

# Annealing Studies of Bi and Kr Inclusions in Al

**Bjørn Toft, Nina**

*Publication date:*
1995

*Document Version*
Publisher's PDF, also known as Version of record

RISØ

Risø-R-783(EN)

# Annealing Studies of Bi and Kr Inclusions in Al

Nina Bjørn Thoft

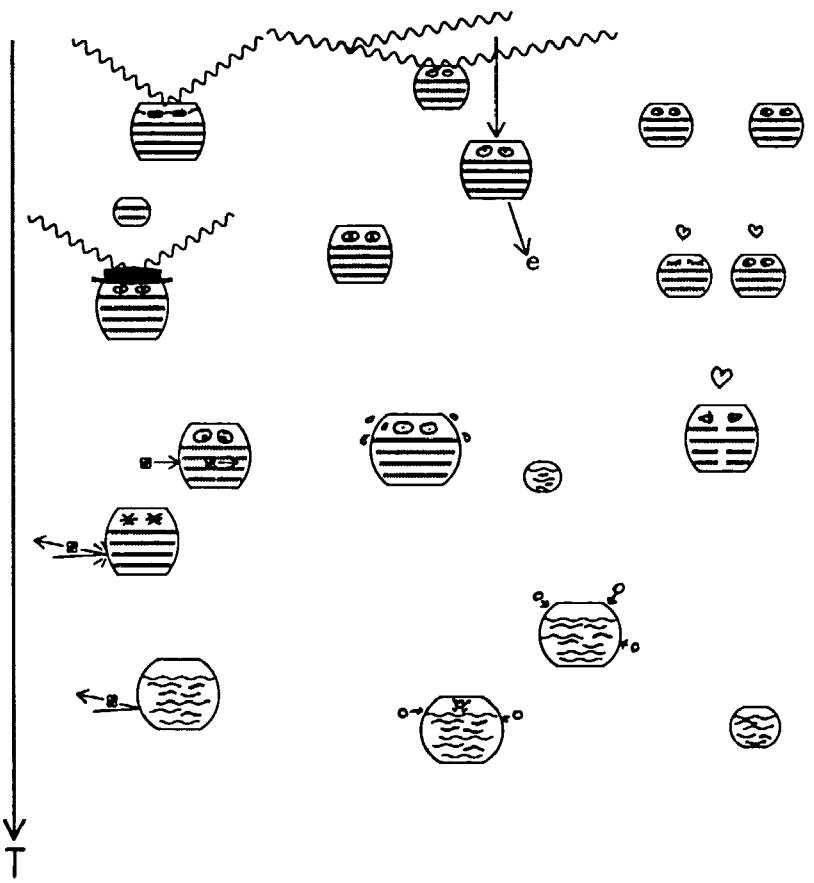


Risø National Laboratory, Roskilde, Denmark
April 1995

Risø–R–783(EN)

# Annealing Studies of Bi and Kr Inclusions in Al

**Nina Bjørn Thoft**

*Risø National Laboratory, Roskilde, Denmark*
*April 1995*

**Abstract** This report contains the results of experimental investigations of melting, solidification and growth of Bi and Kr inclusions made by ion implantation into aluminium. The experimental techniques used for this study were x-ray diffraction, transmission electron microscopy, Rutherford backscattering, ion channeling, and grazing-incidence small-angle x-ray scattering.

The x-ray diffraction signal from crystalline Bi inclusions in Al has been recorded as a function of temperature during heating to temperatures above the bulk melting point and cooling to room temperature. Data from these measurements have been fitted using models (developed by Pawlow and Wronski) for the size-dependent melting temperature of small particles, and size distributions for the inclusions have been determined in this way.

Transmission electron microscopy has confirmed the melting and solidification of the Bi inclusions in the temperature ranges, in which these processes were observed by x-ray diffraction, establishing the facts that the inclusions melt below the bulk melting point and that a large supercooling is seen.

Information about the amount and depth distribution of the Bi confined in the Al matrix has been derived from Rutherford backscattering measurements. Melting and solidification of Bi inclusions have been observed by means of ion channeling.

The results of the investigations of bismuth inclusions in aluminium are compared to previous, similar results for lead inclusions in aluminium.

Finally, preliminary experiments have confirmed that growth of Kr inclusions in Al can be observed using grazing-incidence small-angle scattering.

This report is submitted in partial fulfilment of the requirements for a Ph.D. degree at the University of Copenhagen. The supervisors were Jakob Bohr at the Technical University of Denmark and Erik Johnson at the University of Copenhagen.

ISBN 87-550-2028-3
ISSN 0106-2840

Grafisk Service Risø · 1995

**Dansk resumé** Denne rapport indeholder resultater fra eksperimentelle undersøgelser af smeltning, størkning og vækst af bismut- (vismut) og krypton-inklusioner fremstillet ved ion-implantering i aluminium-krystaller. Flere forskellige eksperimentelle teknikker har været benyttet.

Hovedvægten i denne rapport er lagt på røntgendiffraktionsundersøgelser af bismut-inklusioner i aluminium. Diffraktionstoppen fra de krystallinske inklusioner blev studeret som funktion af temperaturen ved opvarmning til bismuts smeltepunkt og følgende afkøling til stuetemperatur. Resultater fra disse målinger er blevet beskrevet ud fra modeller for små partiklers størrelsesafhængige smeltning, og herved er der udledt størrelsesfordelinger for inklusionerne.

Transmissionselektronmikroskopi har bekræftet, at smeltning og størkning af bismut-inlusionerne finder sted i de temperaturintervaller, hvor det blev set i røntgenmålingerne. *In situ* opvarmning i elektronmikroskopet viser, at nogle inklusioner smelter ved temperaturer, der er væsentligt lavere end bismuts smeltepunkt, og ved den efterfølgende afkøling ses, at smeltede inklusioner først størkner, når temperaturen er langt under bismuts smeltepunkt.

Mængden af bismut og dets dybdefordeling i aluminiumkrystallen er blevet fundet ved hjælp af Rutherford-tilbagespredning. Smeltning og størkning af inklusioner er blevet observeret med ion-channeling. Resultaterne fra studiet af bismut-inklusioner sammenlignes med tidligere, tilsvarende undersøgelser af bly-inlusioner i aluminium.

Til slut beskrives foreløbige resultater, der viser, at vækst af krypton-inklusioner i aluminium kan observeres ved hjælp af småvinkelspredning under strejfende indfald.

# Contents

# 1 Introduction

The main purpose of this piece of work is to learn more about the physics governing the melting, solidification and growth processes of small particles and the importance of the interface formed between two immiscible elements. Bismuth and krypton inclusions in aluminium have been studied employing several different experimental techniques, and the results have been compared for a check of consistency.

Bismuth and aluminium are immiscible. When they are mixed by ion implantation it is like mixing oil and water. The system reaches equilibrium when the two phases are completely separated; the inclusions appear when the phase separation is initiated at many sites simultaneously.

Different experimental techniques each have their advantages and drawbacks. Transmission electron microscopy gives a direct picture of the inclusions in the matrix and electron diffraction images show the existence of liquid or solid phases. The number of inclusions under investigation is quite low, rendering conclusions on the general behaviour of the inclusions difficult, and the precision of the diffraction images is not sufficient to support precise determinations of lattice spacings. X-ray diffraction (in the Bragg mode) gives quantitative results averaged over a large number of inclusions. Several effects may however cause similar behaviour of the diffracted intensity; if a change in the width of the reflection is overlooked, the melting or realignment of inclusions could be confused when no other evidence was brought forth. Rutherford backscattering and ion channeling are sensitive to the depth at which scattering occurs. The total amount of Bi in the sample and a depth profile of the implanted Bi can be extracted from these measurements. The observation of a channeling effect in the inclusions restricts the orientation of the inclusions with respect to the aluminium matrix. Ion channeling gives direct-space evidence of the melting phase transition, as the channeling effect in the inclusions must disappear when the inclusions are liquid.

Previously, a large effort has been put in the study of lead inclusions in aluminium, which therefore has been a natural basis for comparison for the results of this study. Bi is the element right after Pb in the periodic table. It is one of the few examples of elements which contract when melting. The crystalline structure is rhombohedral with two atoms per unit cell. It is a very open structure (far from close-packed) and looks like a distorted simple cubic structure.

The thesis is organized as follows: An introduction to the subject of melting and solidification of inclusions is given in Chapter 2. The models of size-dependent melting developed by Pawlow[46] and Wronski[70] are presented.

Bismuth inclusions in aluminium are the subject of the Chapters 3–5. The first section of Chapter 3 deals with the basic elements of diffraction and is followed by a section on the experimental setup for x-ray diffraction. The results of the x-ray diffraction experiments are presented in the third section of Chapter 3, which finishes with a discussion of the two models of size-dependent melting in relation to the x-ray data. Chapter 4 deals with transmission electron microscopy. After an introduction to the method, tentative assumptions on the orientational relationship between the lattices of the inclusions and the host are discussed. In the next section heating sequences in the electron microscope confirming the melting of the inclusions are shown. The Rutherford backscattering and ion channeling experiments are described in Chapter 5, which finally gives a comparison between the x-ray and channeling data.

The subject of Chapter 6 is the grazing-incidence small-angle x-ray study of Kr inclusions in aluminium. The method is presented, a simple data reduction is performed and some of the results are compared to an x-ray diffraction measurement by Gråbæk[21].

Some of the results on Bi inclusions in Al have previously been presented as posters, and a paper on parts of this work is to be published in Journal of Physics D: Applied Physics[64]. The grazing incidence small-angle x-ray scattering experiments were done in collaboration with Prof. A. Naudon and Prof. C. Templier of the University of Poitiers, and the data have been presented as a poster and a contribution to the proceedings from the IX$^{th}$ International Conference on Small-Angle Scattering by Slimani, Thoft and Naudon[57].

The references are arranged alphabetically after the authors' surnames.

# 2 Melting and solidification of inclusions

**In Section 2.1 the size range of inclusions is defined, and examples are given of inclusions formed by noble gases and metallic elements. Section 2.2 deals with the processes of melting and solidification from the point of view of finite-size systems. Some of the previous experiments on melting and solidification of thin films or inclusions are presented, short descriptions are given of the models of melting by Lindemann[38], Pawlow[46], and Wronski[70], and finally, the homogeneous and heterogeneous nucleation processes are defined.**

## 2.1 Introduction to inclusions

**The field of very small particles**

In the field of very small particles there is no general agreement on the terminology describing the size classification. Depending on the element involved the words inclusions, precipitates, and (for rare gases) bubbles are used for confined particles in the same range of sizes. Harrison and Edwards[26] suggested the use of the word "cluster" for (free) particles containing between 1 and 10 atoms, "aggregate" when the number of atoms is in the range 10–100 atoms, and "small metallic particle" (or "ultrafine particle"[36]) for the range 100–10000 atoms. In this thesis the word "inclusion" denotes a particle in the diameter range 50–500 Å, enclosed within the mass of a bulk material, the host. Such a particle would contain about 1000–1000000 atoms. A bismuth inclusion with a typical diameter of 200 Å contains around 100000 atoms. For comparison, the number of atoms in a bulk material is at least in the region of Avogadro's number ($6 \cdot 10^{23}$ atoms). One reason that inclusions are interesting is that their sizes lie between those of the bulk material and the clusters. This means that compared to a bulk material there is a large fraction of atoms, which lie in the surface and therefore feel a different potential. An investigation of the physics of inclusions can help shed light upon what governs the physical properties of a particle when growing from one atom to a bulk material.

When particles of elements which form cluster structures (*e.g.* Na and Xe) reach the size range of the inclusions, the clusters structures[6] are no longer observed and the particles have taken the crystalline structures known from bulk materials. However, several examples (see below) show that the surface/interface still plays an important role in determining which of the bulk structures is favorable. Further, the surface/interface has a strong influence on physical properties of the material, such as melting temperature, in this size range. Tersoff *et al.*[63] have reported a low energy electron microscopy study of the growth of small (around 1 $\mu$m) silver crystallites on a silicon (111) surface. They demonstrated that the equilibrium shape at a temperature below the roughening temperature was not unique, but an oscillatory function of the number of atoms changing from sharply facetted to rounded and back.

**Noble gas inclusions**

Solid noble gas inclusions were first reported in 1984, when vom Felde *et al.*[17] and Templier *et al.*[62] independently found that argon and xenon inclusions in aluminium had face-centered cubic (fcc) structures and were epitaxially aligned with the aluminium host lattice. Transmission electron microscopy studies[61] of xenon inclusions in different metallic hosts showed that when the matrix was fcc (Al, Ag, Au, Ni, and Cu), the inclusion structure was fcc in epitaxial alignment. When the matrix was Zn, which has hexagonal close-packed (hcp) structure, the xenon inclusions were also hcp in epitaxy with the matrix. The lattice parameters

of the solid xenon inclusions indicated that the pressure in the inclusions was around 1-5 GPa at room temperature.

X-ray diffraction studies[24] of krypton and xenon inclusions in an aluminium matrix have confirmed the fcc structures and high pressures reported previously[61]. When heated, the smaller inclusions gradually lose their epitaxial alignment with the matrix as the facets of the confining aluminium void undergo a roughening transition[2]. The larger inclusions keep their alignment until they melt. The melting transition is broadened by the pressure.

**Metallic inclusions in aluminium**

A wide variety of inclusions with aluminium as host material has been studied, e.g. Al-Tl, Al-Pb, Al-In, Al-Na, and Al-Cd. The inclusions form as a result of phase separation of two immiscible elements. The structure of aluminium is face-centered cubic.

The behaviour of thallium inclusions in aluminium is an interesting example of the influence of the matrix. The equilibrium structure of bulk thallium at atmospheric pressure is hexagonal close-packed (hcp) at temperatures below 503 K, and body-centered cubic (bcc) between 503 K and the bulk melting point[40]. At high pressures (above 3.8 GPa) a transition to the face-centered cubic structure occurs[65]. Recent transmission electron microscopy studies[59, 58, 34] have shown that thallium inclusions in aluminium have either an fcc, hcp or bcc structure depending on their size. The smaller inclusions take up the host fcc structure in epitaxial alignment, while the larger ones are bcc and follow the Kurdjumov-Sachs rule for the alignment (orientational relationship) between fcc and bcc structures[59]. Inclusions with hcp structure have also been observed[58]. From a subsequent high-pressure study[45] of pure thallium using a diamond-anvil cell it has been estimated that the lattice parameter of the fcc inclusions corresponds to a pressure of approximately 0.23 GPa.

Lead inclusions in aluminium have been studied with a wide range of experimental methods, including transmission electron microscopy[75, 32, 54], differential scanning calorimetry[75], x-ray diffraction[21, 23], and channeling[8, 7]. Lead inclusions in aluminium have the bulk fcc structure with a lattice parameter corresponding to a pressure of at most 0.18 GPa[23], and the inclusions are almost perfectly aligned with the Al matrix with a possible misorientation less than 0.1°[8].

Observations of indium inclusions in aluminium show similarities with the Al-Pb system; the inclusions have an fcc structure in epitaxial alignment with the aluminium lattice[32]. However, the bulk equilibrium structure of indium is tetragonal, and the structure of the inclusions is thus a result of the influence of the aluminium matrix, or alternatively, of the small size of the inclusions. Larger inclusions show signs of internal and interface strains resulting from the attempt to take up the bulk indium structure[29, 32]. *In situ* electron microscopy heating experiments on indium inclusions in aluminium showed size-dependent superheating (38 K) and supercooling (around 25 K)[51]. High resolution microscopy has revealed that melting initiates at the {100} facets[53].

The information on the bismuth in aluminium system is more scarce. Roth *et al.*[50] using differential thermal analysis and electron microscopy reported supercoolings of 24 K for lead particles in aluminium and 93.5 K for bismuth particles in aluminium. In neither case was superheating observed. The average sizes of the particles were 5-10 $\mu$m, *i.e.* they were more than two orders of magnitude larger than the inclusions studied in the present work.

| Element | Inclusion structure | References |
|---|---|---|
| Kr | fcc | [17, 62] |
| Xe | fcc | [17, 62] |
| Na (bcc) | fcc or bcc | [30, 31] |
| Cd (hcp) | hcp | [75, 52] |
| In (tetr.) | fcc | [51, 74, 29, 53, 32] |
| Tl (hcp) | fcc, hcp or bcc | [34, 58, 59] |
| Pb (fcc) | fcc | [23, 21, 75, 32, 54, 72, 8, 7] |

***Table 1. Structures of inclusions of different elements in aluminium (fcc) and references to the literature. The structures in parentheses in the first column are the bulk structures of the elements.***

## 2.2 Introduction to melting and solidification

In spite of the widespread use of melting and solidification in technology, our understanding of the solid-liquid phase transition is incomplete, and there is hence a significant experimental and theoretical interest in the subject.

Melting of small particles has been discussed by several authors. In general, theories predict that the change in melting temperature of a free particle is inversely proportional to the particle radius[47]. The reason is that the surface-to-volume ratio increases with decreasing radii of the particles. A review of the current understanding of melting and solidification has been given by Kofman *et al.*[36].

Turnbull and Cech[67] observed supercoolings of Bi particles in the size range 10-50 $\mu$m up to 90 K below the bulk melting temperature by means of optical microscopy. To achieve homogeneous nucleation (see page 13) they limited the number of particles containing catalysts by breaking up the metal into a large number of isolated parts.

Takagi[60] studied structural changes of thin films (10-1000 Å) of lead, tin, and bismuth at various temperatures by electron diffraction. He observed a lowering of the melting temperature, relative to the bulk values. For lead and bismuth films of mean thickness 50 Å, he observed a supercooling of 96 K and 53 K, respectively.

Frenken *et al.*[18] reported the first direct observation of a reversible melting transition of the surface of a crystal in 1985 using Rutherford backscattering. They found that the melting of the (110) surface of lead starts 40 K below the bulk melting point, and that the thickness of the molten layer increases steeply when the temperature approaches the bulk melting point in agreement with the model proposed by Lipowsky[39].

In x-ray diffraction studies by Gråbæk *et al.*[22, 23] of lead inclusions in aluminium, size-dependent superheating (up to 67 K) and supercooling (at least 18 K) were observed. It was concluded that the most important single factor contributing to the superheating is the absence of a free surface on which melting can nucleate. The observed supercooling is believed to be caused by the inability of the inclusions to solidify by homogeneous nucleation at higher temperatures because of their small size. Transmission electron microscopy[54] have shown that the situation is reversed for very small inclusions (2-5 nm) - the smaller the inclusion the higher the solidification temperature. A very recent high resolution electron microscopy study[72] showed differences between the inclusions formed at the grain boundaries and the ones inside the grains. The inclusions at the grain boundaries started to dissolve around 25 K below the bulk melting point, while the inclusions inside the grains only started to melt 25 K above the bulk melting point. Undercoolings as large as 25 K were observed. Some of the inclusions at the grain boundaries were twinned. Moore *et al.*[43] have studied surface energies

and solidification kinetics of lead inclusions in quenched alloys of aluminium and lead. The lead {100} facets disappeared when the inclusions melted (at the bulk melting point) while the {111} facets (stabilized by the aluminium facets) disappeared gradually, and the inclusions finally became spherical around 225 K above the bulk melting point. These results are confirmed by x-ray diffraction studies[22]. Recently Cantor[12] has reported an adsorption model of heterogeneous nucleation of solidification, the predicted supercoolings of which are in reasonable agreement with previously reported experimental results on binary and ternary "alloys" between immiscible elements.

Bismuth contracts on melting (like ice and germanium), and its thermal expansion coefficient is smaller than that of aluminium. Lead expands on melting (like most elements), and its thermal expansion coefficient is comparable to that of aluminium[10]. This makes it interesting to compare the melting and solidification behaviours of bismuth inclusions in aluminium to those of the Al-Pb system, as was also pointed out by Roth *et al.*[50].

Yoon *et al.*[73] have reported the nucleation of a metastable Bi phase at large supercoolings of a fine (1–20 $\mu$m) droplet sample. The metastable phase, Bi(*II*), known at high pressures (see Fig. 1), is base centered monoclinic with four atoms per unit cell and cell parameters $a = 6.674$ Å, $b = 6.117$ Å, $c = 3.304$ Å, and $\beta = 110.33°$ at 2.6 GPa and 30°C. The Bi(IV) is bcc with two atoms per unit cell and $a = 3.800$ Å at room temperature and 9 GPa. Bi(I) is the rhombohedral structure stable at ambient condition[71]; the structures are unknown for the other phases in the pressure-temperature phase diagram in Fig. 1.

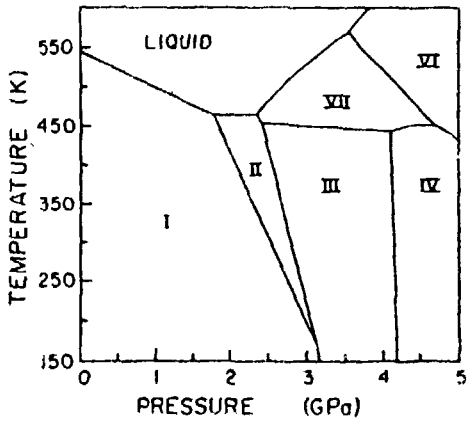


*Figure 1. The pressure-temperature phase diagram for bismuth[73].*

### Models of melting

Lindemann[38] proposed that a solid melts, when the amplitude of the vibrations of the atoms around the lattice positions reaches a certain fraction of the interatomic distance, at which temperature the effective volumes of neighbouring atoms collide. A reasonable agreement with experimental data was found when this fraction was set to approximately 10%. On the basis of the Lindemann criterion Shi[55] has recently proposed a simple model for the size-dependent melting temperature, which is in good agreement with experimental observations.

Buffat and Borel[11] found satisfactory agreement between their melting data for small, supported gold particles and a phenomenological model. The model assumes a solid or liquid particle in equilibrium with its vapour phase. The melting temperature $T_m$ of a solid spherical particle of radius $r$ is deduced by equating the chemical potentials of the solid and liquid phases. Restricting their result to first order gives the result previously found by Pawlow[46] (model A):

$$\frac{T_m}{T_B} = 1 - \frac{2}{Lr\rho_s^{1/3}}\left(\frac{\gamma_s}{\rho_s^{2/3}} - \frac{\gamma_l}{\rho_l^{2/3}}\right), \tag{1}$$

where $T_B$ is the bulk melting point, $\rho$ the density, $\gamma$ the (isotropic) surface free energy, $L$ the latent heat of melting, and the subscripts $s$ and $l$ denote the solid and the liquid phase, respectively. Buffat and Borel found that this model gives a melting temperature which is slightly too high for the smallest sizes. Wronski[70] (and later Coombes[14]) assumes a thin molten layer of thickness $\delta$ surrounding the solid particle and give the following relationship (model B):

$$\frac{T_m}{T_B} = 1 - \frac{2}{\rho_s L}\left[\frac{\gamma_{sl}}{r-\delta} + \frac{\gamma_l}{r}\left(1 - \frac{\rho_s}{\rho_l}\right)\right], \tag{2}$$

where $\gamma_{sl}$ is the solid-liquid interfacial energy, and $r$ is the total radius of the partly liquid particle. Buffat and Borel[11] found satisfactory agreement between their data and this model, when the value of the parameter $\delta$ was 6.2 Å. However, their measurements did not permit a conclusive choice to be made between the two models.

**Homogeneous and heterogeneous solidification**

The solidification transformation begins with the formation of a very small solid particle, a solidification nucleus. If the nucleus is formed at a boundary, *e.g.* at an impurity in the liquid or at the confining or supporting material, the process is called heterogeneous nucleation. If no such catalytic site is present, the nucleus has to form homogeneously from the liquid in a so-called homogeneous nucleation process. A detailed discussion of these processes can be found in the textbook by Porter and Easterling[48]. A brief introduction will be given here.

The size of the nucleus has to exceed a certain critical size $r_c$, which depends on the temperature and the material, as smaller embryos are unstable at the corresponding temperature. For small undercoolings $\Delta T$ the critical radius is

$$r_c = \frac{2\gamma_{sl}T_B}{L}\frac{1}{\Delta T}. \tag{3}$$

The critical radius for nucleation is identical for homogeneous and heterogeneous nucleation; but for heterogeneous nucleation the activation energy barrier is lower, and smaller undercoolings are obtained. The probability for the formation of a nucleus larger than $r_c$ increases with the number of atoms in the liquid. The largest inclusions are therefore expected to solidify at the highest temperatures (smallest undercoolings). Indeed, if the inclusions are smaller than the critical radius at a given undercooling they are not able to solidify at all, if the interface energies do not favour solidification.

## 2.3 Bismuth in aluminium samples

All samples have been produced by ion implantation of $Bi^+$ into aluminium. Sample preparations and implantations were carried out at the Ørsted Laboratory of the University of Copenhagen. According to the equilibrium phase diagram for the aluminium-bismuth system in Fig. 2, bismuth and aluminium are mutually immiscible. Following implantation, phase separation leads to formation of

Bi inclusions in the Al crystal. The sample orientation and implantation energy, temperature and fluence were adjusted to meet the requirements of the different experimental methods. The beam current density was kept below $4\,nA/mm^2$. To avoid changes in the samples (caused by exposure to air/humidity), which would have been especially severe for the thin electron microscopy samples, the samples were kept under vacuum until they were studied. When transferring samples from the target chamber of the separator to the x-ray furnace or the transmission electron microscope the time spent in air by the samples was made as short as possible.

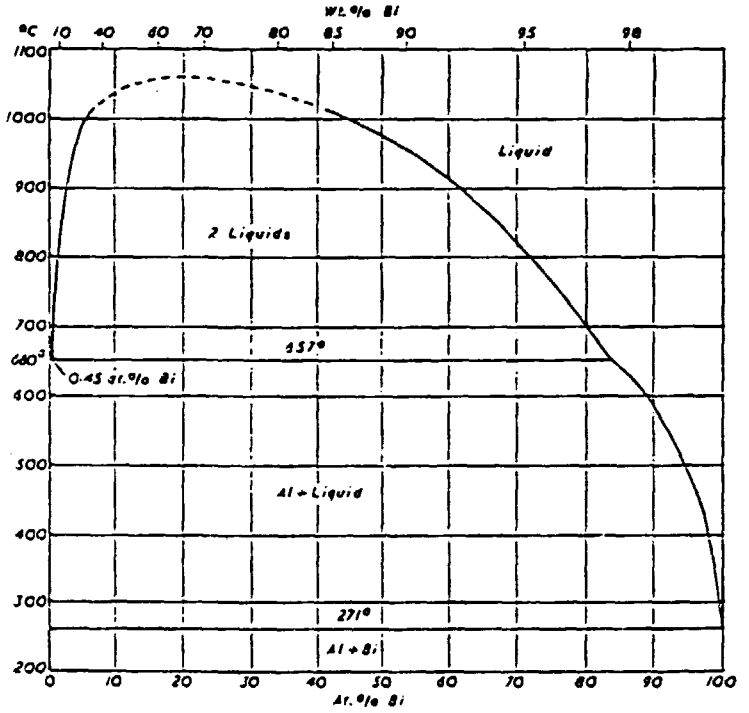


*Figure 2. Equilibrium phase diagram for the Al-Bi system [10].*

The bismuth ion energy was 150 keV for the x-ray and channeling samples and 100 keV for the transmission electron microscopy samples. For transmission electron microscopy, the samples had to be very thin — less than a few hundred nanometers thick. As the implantation depth depends on the ion energy, a lower implantation energy was chosen for the transmission electron microscopy samples.

50 $\mu$m thick samples for transmission electron microscopy were punched out from cold-rolled and recrystallised aluminium foils of 99.999% purity (Goodfellow Ltd., UK). The diameter of the samples was 3 mm to enable them to fit into the holders of the electron microscope. The side of the samples used for implantation was prepared by electropolishing. After implantation to fluences of around $1 \cdot 10^{16}\,at/cm^2$ the samples were back-thinned to perforation. A sufficiently thin (less than a few hundred nanometers thick) area was usually achieved close to the edge of the hole. As the samples were polycrystalline, inclusions could be studied in aluminium grains with different crystallographic orientations. Four such samples (TEM-1–TEM-4) were made for transmission electron microscopy.

For x-ray diffraction and channeling experiments disks of aluminium single crystals 9 mm in diameter and 1–2 mm thick were cut by spark-machining from a larger

crystal of 99.999% purity (Monocrystals Company, Cleveland). The surfaces of the crystals were prepared for implantation by mechanical and electrolytical polishing.

The x-ray samples (called X-1 and X-2) were cut with a (111) surface normal and implanted at room temperature to fluences of around $2 \cdot 10^{16}$ at/cm$^2$. The implantations were carried out in a 4 mm wide strip across the sample by scanning a 2 mm high slit twice across the sample. To avoid accidental channeling during implantation, the samples were rotated 10° away from the high-symmetry orientations (low-index axes).

The channeling effect in aluminium is largest along the [110] direction[20]. The sample (Ch-1) for channeling experiments was therefore cut with a (110) surface normal. Sufficient sensitivity on the channeling in the inclusions is present only for relatively large inclusions[8]. The crystal was therefore implanted at a temperature ($T = 548$ K) above the Bi bulk melting point ($T_B = 544.5$ K[10]). The fluence was $7.5 \cdot 10^{15}$ at/cm$^2$. To avoid excessive channeling, the crystal was implanted 10° off normal incidence and rotated around the surface normal during implantation. The Rutherford backscattering and ion channeling investigations were performed without breaking the vacuum using a 500 keV $He^{2+}$ beam from the accelerator for analysis.

An overview of implantation conditions of the samples studied and the experiments performed on these samples is given in Tab. 2.

| Samples | Implantation energy keV | Implantation temperature K | Fluence at/cm$^2$ | Temperature ranges of experiments/annealings K |
|---|---|---|---|---|
| X-1 (163 A nr. 1) | 150 | 295 | $2 \cdot 10^{16}$ | 298-624-298-547-298-548-298 |
| X-2 (194 B nr. 1) | 150 | 295 | $2 \cdot 10^{16}$ | 298-569-298-15-294 |
| Ch-1 (168 A) | 150 | 548 | $7.5 \cdot 10^{15}$ | 296-553-308 |
| TEM-1 (EJ-2 B6) | 100 | 295 | $1 \cdot 10^{16}$ | 298 |
| TEM-2 (Ar B4) | 100 | 295 | $1 \cdot 10^{16}$ | 298-633-298-607-386 |
| TEM-3 (EJ94 B2) | 100 | 523 | $1 \cdot 10^{16}$ | 298 |
| TEM-4 (EJ94 D2) | 100 | 523 | $1 \cdot 10^{16}$ | 298-518-298 |

*Table 2. Samples of bismuth inclusions in aluminium, implantation energies, temperatures, and fluences. The last column gives the temperature ranges of the experiments, which have been performed on the samples.*

# 3 X-ray diffraction

In the first two sections of this chapter the basic theory of diffraction and the experimental setup are presented. Thereafter the data analysis and the results are discussed, and finally size distributions are derived by modelling the decrease of the intensity during melting.

## 3.1 Diffraction theory

**X-rays**

X-rays are electromagnetic radiation of very short wavelenght, typically in the range 0.1-10 Å. These wavelengths are on the order of the distances between atoms in a solid, making x-rays a useful tool for structural studies of matter. Diffraction patterns from crystals were observed in 1912 by W. Friedrich and P. Knipping following M. von Laue's predictions[19], and shortly after, W. L. Bragg determined the crystal structures of NaCl and KCl and developed an alternative picture of x-ray diffraction[9].

A short presentation of the basic theory of x-ray diffraction by crystalline matter based on the textbooks of Warren[68] and Guinier[25] will be presented here.

In the classical picture of x-ray scattering, the electric field of the incident x-rays causes the electrons to oscillate around their equilibrium position at the frequency of the field. The accelerations of the oscillating electrons cause them to emit radiation in all directions at the same frequency as the incident radiation. In this process, which is called Thomson scattering, the x-rays are scattered elastically, i.e. without loss of energy. This contrasts with Compton scattering, where some of the energy of the incident x-ray is lost to the crystal. Another possible event is photoelectric absorption of x-rays by the atoms. The atom is excited and electron emitted. When it decays, the superfluous energy is removed as the system emits one or more photons of energies characteristic of the element (fluorescence) or one or more electrons (the Auger effect).

The classical treatment can only predict elastic scattering; polarization is given correctly by classical calculations and the classical scattering intensity is close to the measured one when the non-elastic contributions (*e.g.* Compton and photoelectric effect) have been subtracted.

A wave mechanical treatment yields the result that the scattering amplitude of a single electron, observed from a point far away compared to the dimensions of an atom, can be calculated as an integral of the charge density corresponding to this electron times the classical scattering amplitude from one electron. The scattering from the entire atom can be obtained by summing the contributions from the electrons of the atom. The atomic scattering factor, $f$, expresses the elastic scattering amplitude per atom of a specific element in units of the classical scattering amplitude from a single electron. It plays an important role in x-ray diffraction theory in analogy with the scattering length in neutron diffraction. The atomic scattering factor increases with the number of electrons, that is with the atomic number. Values of atomic scattering factors have been tabulated and appear in the literature[27].

Thomson scattering is the main interaction between the x-rays and the electrons. The cross section for scattering caused by the interaction between the x-rays and the magnetic moment of the electrons in the crystal is typically 5-6 orders of magnitude smaller than the cross section for Thomson scattering.

### The Bragg law

W. L. Bragg accounted for the characteristic pattern of x-rays reflected from crystalline materials by the well-known law bearing his name. It is based on the specular reflection of the incident x-rays in each crystal plane, and the constructive interference of the x-rays reflected from different parallel planes. To obtain

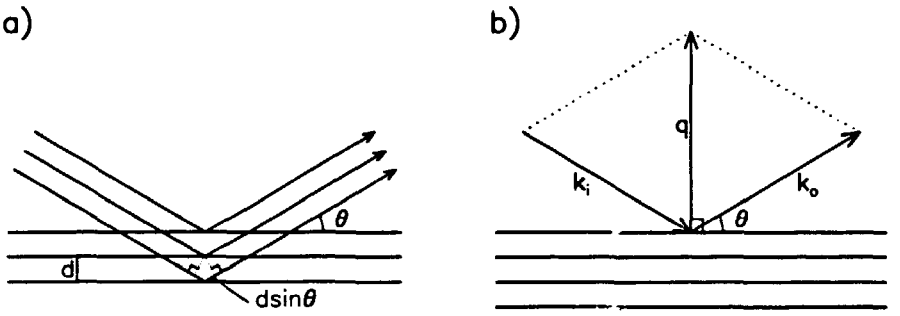


*Figure 3. a) Bragg reflection from a set of parallel atomic planes. The path difference between x-rays scattered by adjacent planes is* $2 \cdot d\sin\theta$. *b) The scattering vector* $\mathbf{q}$.

constructive interference the difference in the path length travelled by x-rays reflected from successive planes must be an integral number $n$ of wavelengths $\lambda$, as can be seen from Fig. 3a. The path difference is expressed in terms of the distance $d$ between the planes, leading to the Bragg relation

$$n\lambda = 2d\sin\theta, \tag{4}$$

where $\theta$ is the angle between the crystal planes and the incident x-rays.

Let $\mathbf{k}_i$ and $\mathbf{k}_o$ denote the wavevectors of incident and scattered x-rays, respectively. As the scattering is elastic, these two vectors have equal lengths, $k = 2\pi/\lambda$. The Bragg law can be rewritten as $2k\sin\theta = n2\pi/d$ or $q = 2k\sin\theta$, where $q = 2\pi/d$ is the length of the vector $\mathbf{q} = \mathbf{k}_o - \mathbf{k}_i$ (see Fig. 3b). The vector $\mathbf{q}$ is called the scattering vector and is a measure of the momentum transferred in the scattering process. It contains information about the crystal structure because its length gives the spacing between crystal planes in a given orientation and it is perpendicular to the scattering planes.

Another much used equivalent treatment of x-ray diffraction has been given by von Laue, whose starting point is the crystal viewed as atoms placed on the sites of a lattice, instead of the sectioning of the crystal into planes used by Bragg. In his formulation, constructive interference occurs provided that the scattering vector $\mathbf{q}$ is a vector of the reciprocal lattice, which is defined in the next section.

### The reciprocal lattice

The reciprocal lattice is defined from the direct space lattice of the crystal. Let $\mathbf{a}_1, \mathbf{a}_2$, and $\mathbf{a}_3$ be the lattice vectors in direct space. The reciprocal lattice vectors $\mathbf{b}_1, \mathbf{b}_2$. and $\mathbf{b}_3$ are given by:

$$\begin{aligned}
\mathbf{b}_1 &= 2\pi\frac{\mathbf{a}_2 \times \mathbf{a}_3}{\mathbf{a}_1 \cdot \mathbf{a}_2 \times \mathbf{a}_3}, \\
\mathbf{b}_2 &= 2\pi\frac{\mathbf{a}_3 \times \mathbf{a}_1}{\mathbf{a}_2 \cdot \mathbf{a}_3 \times \mathbf{a}_1}, \quad \text{and} \\
\mathbf{b}_3 &= 2\pi\frac{\mathbf{a}_1 \times \mathbf{a}_2}{\mathbf{a}_3 \cdot \mathbf{a}_1 \times \mathbf{a}_2},
\end{aligned} \tag{5}$$

which fulfils

$$\mathbf{a}_i \cdot \mathbf{b}_j = 2\pi\delta_{ij} \tag{6}$$

justifying the name reciprocal lattice. The $(h,k,l)$ plane in the direct lattice is the one which cuts the lattice axes in $(\mathbf{a}_1/h, \mathbf{a}_2/k, \mathbf{a}_3/l)$. The integers $h$, $k$, and $l$ are called the Miller indices. Directions in the direct lattice are written $[h,k,l]$ $\{h,k,l\}$ denotes equivalent planes, and $<h,k,l>$ equivalent directions. For cubic lattices the relation $[h,k,l] \perp (h,k,l)$ holds.

Saying that the scattering vector $\mathbf{q}$ is a vector of the reciprocal lattice, means that it can be written $\mathbf{q} = h\mathbf{b}_1 + k\mathbf{b}_2 + l\mathbf{b}_3$, where $h$, $k$, and $l$ are integers, which can be shown to be the Miller indices of the reflecting planes[68].

### Calculated intensity and the structure factor

When the crystal structure is known it is possible to calculate the total scattering amplitude from the complete crystal, $A(\mathbf{q})$, by adding the contributions from individual atoms taking their relative displacement into account. In a simple approximation, the scattering amplitude is therefore

$$A(\mathbf{q}) = \sum_{i=1}^{n} f_i \exp(-i\mathbf{q} \cdot \mathbf{x}_i), \tag{7}$$

where $n$ is the number of atoms in the crystal, $f_i$ and $\mathbf{x}_i$ the atomic scattering factor and real-space position of the $i^{th}$ atom, respectively, and i the imaginary unit. The calculated intensity is given by $I(\mathbf{q}) = |A(\mathbf{q})|^2$.

In a crystal the real-space position of the $i^{th}$ atom can be written as a sum of the vector $\mathbf{r}_i$ from the origin of the unit cell, to which the atom belongs, to the position of the $i^{th}$ atom and a lattice vector $\mathbf{R}_j$ from the origin of the coordinate system to the origin of the $j^{th}$ unit cell. This gives the following expression for the scattering amplitude:

$$A(\mathbf{q}) = \sum_{i=1}^{m} f_i \exp(-i\mathbf{q} \cdot \mathbf{r}_i) \sum_j \exp(-i\mathbf{q} \cdot \mathbf{R}_j), \tag{8}$$

where $m$ is the number of atoms in the unit cell. The second sum is an infinite sum over all lattice vectors $\mathbf{R}_j$ ($\mathbf{R}_j = m_1\mathbf{a}_1 + m_2\mathbf{a}_2 + m_3\mathbf{a}_3$, $m_1$, $m_2$, $m_3$ integers). This sum is unity when $\mathbf{q}$ is a vector of the reciprocal lattice ($\mathbf{q} = h\mathbf{b}_1 + k\mathbf{b}_2 + l\mathbf{b}_3$, $h$, $k$, $l$ integers) and otherwise zero. The first sum contains all information about the positions of the atoms in the unit cell and is called the structure factor ($F$). From the structure factor the theoretical relative intensities of different reflections can be calculated. As an example, the structure factor of bismuth will be calculated below. At ambient conditions bismuth has a rhombohedral structure with $a = 4.7459$ Å, $\alpha = 57.2369°$ and two atoms per unit cell in the positions $(u,u,u)$ and $(1-u, 1-u, 1-u)$, where $u = 0.237$[71]. The structure factor then becomes:

$$\begin{aligned} F_{hkl}(\mathbf{q}) &= \sum_{i=1}^{m} f_i \exp(-i\mathbf{q} \cdot \mathbf{r}_i) \\ &= f_{Bi}\,(\exp(-i(h\mathbf{b}_1 + k\mathbf{b}_2 + l\mathbf{b}_3) \cdot (u\mathbf{a}_1 + u\mathbf{a}_2 + u\mathbf{a}_3)) \\ &+ \exp(-i(h\mathbf{b}_1 + k\mathbf{b}_2 + l\mathbf{b}_3) \cdot ((1-u)\mathbf{a}_1 + (1-u)\mathbf{a}_2 + (1-u)\mathbf{a}_3))) \\ &= f_{Bi}\,(\exp(-iu(h+k+l)) + \exp(-i(1-u)(h+k+l))) \end{aligned} \tag{9}$$

An estimate of the strongest reflections can be made by calculating

$$I_{hkl}(\mathbf{q}) \propto |F_{hkl}(\mathbf{q})|^2 = 2f_{Bi}^2\,(1 + \cos((h+k+l)(1-2u))). \tag{10}$$

Inserting values, this shows that the (011), (01$\bar{1}$), (112) relections are expected to be the strongest ones (see Tab. 3).

| Reflection | $d$ Å | $q$ Å$^{-1}$ | $\lvert F_{hkl}(q)\rvert^2$ a.u. |
|---|---|---|---|
| (111) | 3.9540 | 1.589 | 1355 |
| (001) | 3.7368 | 1.681 | 151 |
| (011) | 3.2802 | 1.915 | 21074 |
| (112) | 2.3688 | 2.653 | 16797 |
| (01$\bar{1}$) | 2.2732 | 2.746 | 18342 |
| (122) | 2.0320 | 3.092 | 2708 |
| (222) | 1.9770 | 3.178 | 13141 |
| (012) | 1.9707 | 3.188 | 992 |
| (11$\bar{1}$) | 1.9421 | 3.235 | 111 |
| (002) | 1.8684 | 3.363 | 15861 |
| (022) | 1.6401 | 3.831 | 13327 |

*Table 3. Relative intensities of bismuth reflections. The values of $q$ and the lattice distances $d$ have been calculated using $a = 4.7459$ Å, $\alpha = 57.2369°$ [71].*

**Diffraction from a very small crystal**

A small crystal size leads to broadening of the diffraction peaks. This can be demonstrated most easily in a simple, one-dimensional example. Consider a one-dimensional crystal with $N$ atoms positioned with a spacing $a$, like pearls on a string. The length $L = aN$ of the crystal is finite.

$$\begin{aligned} I(q) &= |A(q)|^2 \\ &= \left|\sum_{i=1}^{N} f \exp(-iq(i-1)a)\right|^2 \\ &= \left|\sum_{i=1}^{N} f \left(e^{(-iqa)}\right)^{i-1}\right|^2 \\ &= \left|f\frac{1-e^{-iqaN}}{1-e^{-iqa}}\right|^2 \\ &= f^2\frac{\sin^2(qaN/2)}{\sin^2(qa/2)} \end{aligned} \tag{11}$$

The shape of this function is shown in Fig. 4. The function is periodic in $qa/2$, and

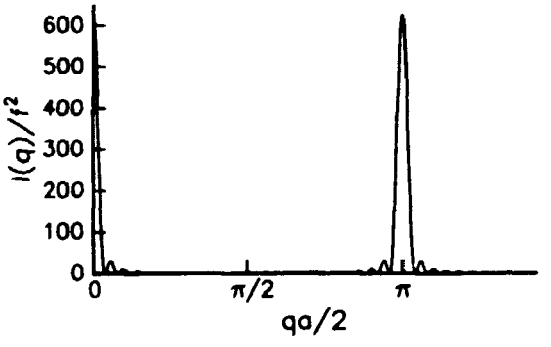


*Figure 4. Shape of the function* $\frac{\sin^2(qaN/2)}{\sin^2(qa/2)}$

the full width at half maximum is calculated most easily for the peak at $q = 0$, as

for small values of $qa$

$$\frac{\sin^2(qaN/2)}{\sin^2(qa/2)} \approx \frac{\sin^2(qaN/2)}{(qa/2)^2}.$$

The full width at half maximum (FWHM) $\Delta q$ of the peak at $q = 0$ is determined by $I(\Delta q/2) = I_{max}(q)/2$ or

$$\frac{\sin^2(\Delta qaN/4)}{(\Delta qa/4)^2} = \frac{N^2}{2}.$$

Solving the transcendent equation numerically leads to $\Delta qaN/4 = 1.39156$ (as seen in Fig. 5) or

$$L = aN = 5.5662/\Delta q. \tag{12}$$

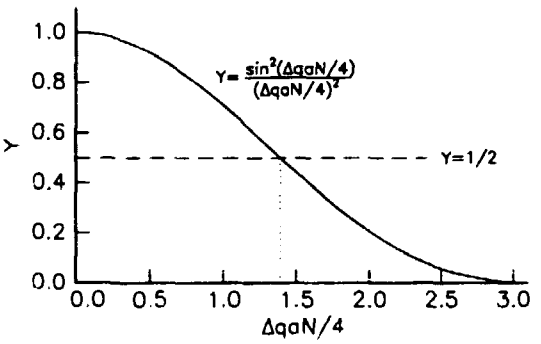


*Figure 5. Solving the transcendent equation* $\frac{\sin^2(\Delta qaN/4)}{(\Delta qaN/4)^2} = \frac{1}{2}$.

A more careful three-dimensional analysis (using a box with side length $L$) leads to the same result for the relation between the size of the system and the resulting peak broadening.

The FWHM due to the small size of the system is not directly measurable, because the instrumental resolution has to be considered (see Section 3.2).

**Thermal vibrations — the Debye-Waller factor**

At all temperatures the atoms of a solid crystal vibrate around their lattice positions. The amplitude of the thermal vibrations increases with temperature until the solid melts and the lattice description breaks down. Because of the thermal agitation, the atoms do not occupy the exact equilibrium positions in the lattice planes and the intensity reflected from the planes of a real crystal is not as strong as the reflections of an ideal crystal lattice. In addition, the background level increases. The diffraction peaks are not broadened by the thermal vibrations.

More formally, the lattice positions (and therefore the displacements from these) of the atoms enter the expression for the structure factor (Eq. 9). If the displacements of the atoms are isotropic around the equilibrium positions, the reduction of the structure factor can be described by a factor $\exp(-M)$, where $M$ is proportional to the mean square displacement of the atoms, which to first order is proportional to the absolute temperature[25],

$$M = \frac{8\pi^2 \sin^2\theta \langle \Delta x^2 \rangle}{\lambda^2} = \frac{q^2 \langle \Delta x^2 \rangle}{2}. \tag{13}$$

$\sqrt{\langle \Delta x^2 \rangle}$ is the root mean square of the component of the displacement normal to the reflecting planes. At room temperature $\sqrt{\langle \Delta x^2 \rangle}$ generally is around 2 tenths of an angstrom for simple crystal structures

As the intensity is proportional to the structure factor to the second power (Eq. 10), the intensity is reduced by a factor $\exp(-2M)$, which is called the Debye-Waller (or Debye) factor.

If the Debye temperature $\Theta_D$ is known, an approximate value of $M$ for a simple crystal is given by[25]

$$M = \frac{\sin^2\theta}{\lambda^2} \frac{6h^2}{km\Theta_D} \frac{T}{\Theta_D} \left[ \phi\left(\frac{\Theta_D}{T}\right) + \frac{1}{4}\frac{\Theta_D}{T} \right], \tag{14}$$

where $k_B$ and $h$ are the Boltzmann and Planck's constant, respectively, and $m$ is the atomic mass. The function $\phi$ (which was introduced by Debye) is tabulated in Ref. [27]. This relation is not strictly applicable to the rhombohedral structure of Bi, but is used here to estimate $M$. Values of the Debye characteristic temperatures of Bi are given in the International Tables for X-Ray Crystallography[27] to be $62\,\mathrm{K} < \Theta_D < 120\,\mathrm{K}$. The Debye temperatures of the elements are generally not very well determined and vary even more for the non-cubic elements than those of the cubic elements. Inserting the atomic mass of Bi gives

$$\frac{2M(\Theta_D)}{T} = \frac{\sin^2\theta}{\lambda^2} \frac{110.0\,K}{\Theta_D^2} \left[ \phi\left(\frac{\Theta_D}{T}\right) + \frac{1}{4}\frac{\Theta_D}{T} \right], \tag{15}$$

which is drawn for the Bi (110) reflection as a function of absolute temperature $T$ in Fig. 6 for both of the limiting values of $\Theta_D$. For temperatures above $\Theta_D$,

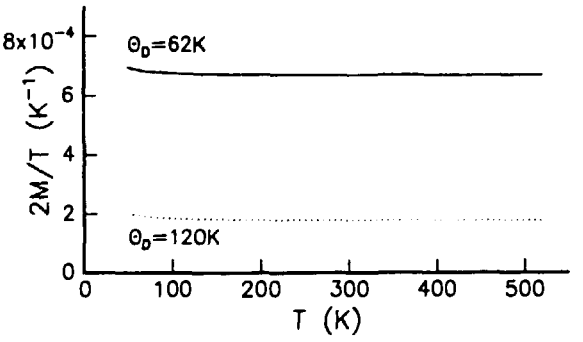


*Figure 6. $2M/T$ as a function of absolute temperature $T$. Full line: $\Theta_D = 62\,K$ Dotted line: $\Theta_D = 120\,K$.*

the function in the square brackets in Eqs. 14–15 is approximately equal to 1 and $2M/T$ is therefore constant, as seen in Fig. 6. The Debye temperature of Bi is so small compared to room temperature that $2M/T$ will be considered a constant below (Section 3.3).

## 3.2 Experimental setup

The x-ray diffraction experiments have been performed on the triple-axis spectrometer at the 12 kW Rigaku rotating anode in the Department of Solid State Physics at Risø National Laboratory.

The experimental setup for the x-ray diffraction experiments is sketched in Fig. 7. A is the rotating anode. A copper anode was chosen in all experiments. $S_i$

are slits, T flight tubes, and M the monochromator. A bent graphite crystal was chosen. This crystal focuses the beam sagittally on the sample, which is marked S. The detector D is a bicron solid state detector.

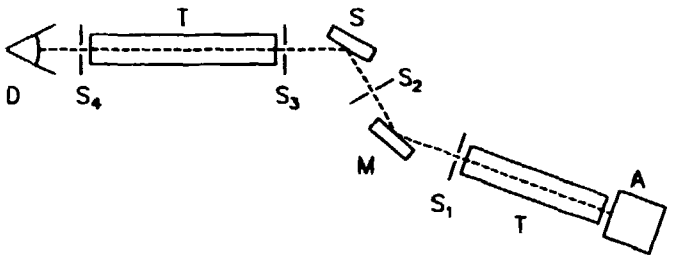


*Figure 7. Sketch of the spectrometer.* A *rotating anode,* $S_i$ *slits,* T *flight tubes,* M *monochromator,* S *sample,* D *detector.*

### Rotating anode x-ray source

A sketch of the wavelength spectrum from the rotating anode equipped with a copper anode is shown in Fig. 8. The continuous part of the radiation has a cut-off at low wavelengths corresponding to the maximum voltage $V_{max}$ between cathode and anode, $\lambda_{min} = hc/eV_{max}$. A series of characteristic lines are superimposed on the continuous spectrum. The wavelengths of the copper $K_{\alpha 1}$ and $K_{\alpha 2}$ lines are 1.54051 and 1.54433 Å, respectively, and the weighted average for $K_\alpha$ is 1.54178 Å[68]. The wavelength of $K_\beta$ is 1.39217 Å. The $K_\alpha$ and $K_\beta$ lines can easily be resolved, and the $K_\alpha$ radiation has been used for these experiments.

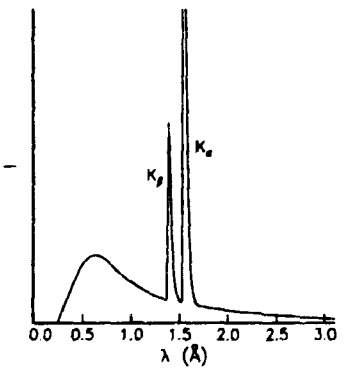


*Figure 8. Sketch of the rotating anode spectrum.*

### The x-ray furnace

A sketch of the x-ray furnace, which was made at Risø by W. Kofoed, is shown in Fig. 9. The sample (1) was mounted with silver paste on the copper base (2) of the furnace. A heater wire (3) was wound around the base and connected to a power supply. The temperature was measured by an iron-constantan thermocouple (4), placed inside the copper base as close to the sample as possible. On top of the body of the furnace (5), an x-ray transparent cap (6) made of plastic or graphite covered

by aluminium was placed, and the furnace was evacuated with a diffusion pump. The plastic caps, which were made from coloured spheres used for Christmas tree decorations, had to be cooled by a fan to prevent melting in the heat radiated from the inside of the furnace. A copper cover (7) was placed around the filament, and the copper base was fastened in an isolating support (8). The furnace fitted the mount on a small Huber goniometer.

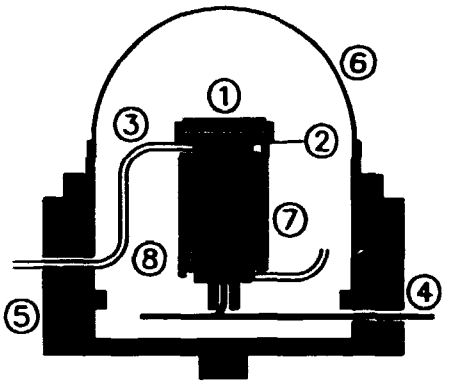


*Figure 9. Sketch of the x-ray furnace. (1) sample, (2) copper base, (3) heater wire, (4) thermocouple, (5) copper body of furnace, (6) x-ray transparent cap, (7) copper cover, (8) isolating support.*

The furnace was controlled from a pc, either by means of an ECA-40 temperature controller or by one of the new Risø temperature controllers. Both of these are feedback-systems. The measured temperature is compared with the programmed temperature and a controller voltage calculated from tuning parameters, which were previously determined and encoded in the system, and sent to a power supply. The output of the power supply is a current proportional to the controller voltage, which is led through the resistor coil. The advantages of the Risø temperature controller are that the temperature can be changed by the program, which runs the spectrometer, making overnight measurements at several different temperatures possible, and that the furnace can be replaced by a displex (a cryogenic cooling unit) without changing the temperature controller.

### Alignment of the spectrometer

The spectrometer is equipped with around twenty translations or rotations which are motorized to facilitate the alignment. The movements of the spectrometer can be controlled either by a manual box (joy-stick principle), which is especially useful when aligning the spectrometer, or by a pc using the program package TASCOM (Triple Axis Spectrometer COMmands) developed at Risø.

The slit $S_1$ defines the direct beam from the anode and its position is optimized before the monochromator is mounted. The width of $S_1$ and its distance from the anode determines the collimation of the beam before the monochromator.

The monochromator table has a rotation and a tilt. The rotation allows the selection of the copper $K_\alpha$ wavelength, and the tilt serves to adjust the height of the beam path.

Other monochromator crystals besides graphite are available; choosing, for instance, a germanium monochromator instead could give higher resolution but lower intensity. The Bi signal was rather faint (a factor $10^6$ lower than the Al

(111) Bragg peak, see Fig. 10), so gaining resolution on the cost of intensity was generally not considered desirable. The sample table has a large translation to

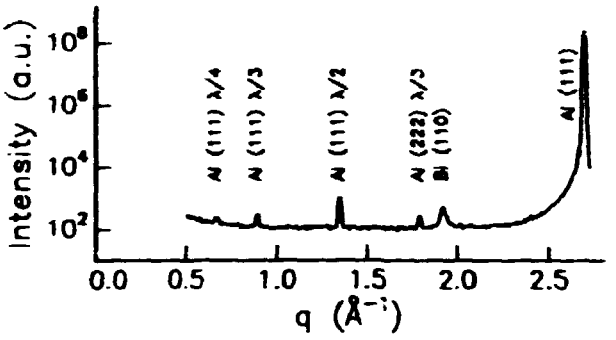


*Figure 10. An x-ray diffraction spectra showing the q-range from 0.5 Å$^{-1}$ to the Al (111) Bragg peak.*

place the center of the sample in the beam, a double goniometer and a rotation to get the desired sample orientation, and two smaller mutually perpendicular horizontal translations to align the sample on the axis of rotation of the table.

The sample S was mounted vertically on a small goniometer on a turntable with horizontal axis, which is sitting on the sample stage. This makes it possible to put a specific crystallographic direction of the sample in the scattering plane and rotate the sample around this axis.

The detector arm ($2\theta$-arm) rotates around the sample table, and the zero point of the rotation is determined using the direct beam from the monochromator.

To avoid losing intensity the detector D is mounted directly on the $2\theta$-arm (double-axis configuration of the spectrometer), the slit $S_4$ was vertically as high as the detector opening and horizontally around 2 mm. The energy resolution of the bicron detector is poor; several higher harmonics of the Cu $K_\alpha$ energy are detected. This can be avoided by using a Ge solid state detector with high energy resolution ($\Delta E/E \approx 3\%$). The Ge detector was used to test the origin of suspected higher-order aluminium peaks, but otherwise it was considered more useful to keep the higher-order aluminium peaks for calibration purposes and measure with the bicron detector, which is easier to handle.

When the beam path and detector zero-angle have been determined, the sample is translated into the beam and the zero-angle of its rotation determined first by aligning the surface of the sample (which was generally well cut — less than a few degrees from the the crystallographic [1,1,1] direction) parallel to the beam and finally by aligning on the aluminium (1,1,1) reflection. The alignment was checked on the aluminium (2,2,2) reflection. When the crystal was aligned in the beam, the furnace was evacuated to reduce the background caused by scattering in air close to the sample and to limit the heat radiation.

### The instrumental resolution

Several effects are included in the instrumental resolution; I will give a short overview of these and refer to Ref. [21] and references therein for a more detailed description of resolution effects and calculation of the resolution following the method proposed by Als-Nielsen *et al.*[1].

As mentioned above (p. 22), the copper $K_\alpha$ radiation consists of two lines separated by $3.8 \cdot 10^{-3}$ Å. The natural linewidth of the lines is $5.8 \cdot 10^{-4}$ Å [49]. There is

therefore a spread in the wavelength of the radiation. As mentioned above, there will be an angular spread of the radiation, which reaches the monochromator, determined by the ratio of the width of the slit $S_1$ in front of the monochromator to the distance between the anode and slit. A further angular spread is introduced by the mosaicity of the graphite monochromator, which is 0.55°(= $9.6 \cdot 10^{-3}$rad). The slit $S_2$ following the monochromator was not allowed to reduce the beam by more than 10%, as its purpose was only to reduce the background and not influence the resolution. The collimation between the monochromator and sample is therefore determined by the width (around 1 mm as seen on a fluorescent screen) of the beam leaving the monochromator and the distance between the monochromator and sample. The collimation after the sample is given by the ratio of the width of the slit $S_3$ to the distance between the slits $S_3$ and $S_4$.

### Correction for instrumental broadening of the FWHM

Grabæk[21] concluded for an equivalent setup that the full width at half maximum (FWHM) of the aluminium (111) Bragg peak in a longitudinal scan was a good measure of the resolution in that direction. The resolution of the spectrometer, which is used as a correction to the observed FWHM $w_o$ of the bismuth reflections, is therefore determined experimentally by measuring the width of the aluminium (111) Bragg peak (see Tab. 4).

| Sample | Temperature cycle | FWHM of Al (111) $Å^{-1}$ |
|---|---|---|
| X-1 | 1 | 0.0195(3) |
| X-1 | 2 & 3 | 0.0125(3) |
| X-2 | 1 | 0.0178(3) |

*Table 4. Full widths at half maximum (FWHM) of the aluminium (111) Bragg peak at room temperature.*

The instrumental width $w_r$ and particle-size broadening $w$ add up linearly if the curves which represent these effects are shaped like Lorentzian functions and quadratically if they are shaped like Gaussian functions. Both Lorentzian and Gaussian fits to the peaks have been made, and the latter (as in Fig. 13) generally gives the best fit to the data. As the convolution af two Gaussian functions yield a third Gaussian function, the deconvolution of the resolution effects has been performed under the assumption of Gaussian shapes and is carried out by calculating

$$w = \sqrt{w_o^2 - w_r^2}. \tag{16}$$

### Data collection

The bismuth {110} reflection (and when present the {111} reflection) has been studied as a function of temperature. The temperature was changed slowly to prevent over-shooting, and when the desired temperature had been reached, data accumulation started only after the temperature was stable. The total time, from changing the set-point temperatu . until data accumulation was begun, was at least 30 minutes.

At each temperature longitudinal scans in the relevant $q$-range were recorded with two points per 0.01 Å. The transverse width was checked at most temperatures by performing a rocking scan. The time spent scanning the spectrometer at each temperature was at least 30 minutes. One temperature cycle of a sample required approximately one week of beamtime at the rotating anode with the ECA-40 temperature controller, and a little less with the Risø controller.

## 3.3 Data analysis and results

**Identification of the peaks**

As pointed out in Section 3.2, several higher order aluminum peaks are seen in the scans (*e.g.* Fig. 10 on page 24). The reason is that the Bragg diffraction condition of the monochromator (and of the sample) is fulfilled for the photons with wavenumbers $k_n$, which are integer multiples $n$ of the wavenumber $k$ chosen by the monochromator alignment, or equivalently, $\lambda_n = \lambda/n$. The photons of wavenumber $k_n$, which are reflected in the sample planes with lattice distance $d = 2\pi/q$, will be detected at an angle $\theta_n$ given by $2\sin\theta_n = q/k_n$. When TASCOM converts the $(\theta,2\theta)$-scan to a $q$-scale, only the value $k$ is used, and the higher order peaks will appear at

$$q_n = 2k\sin\theta_n = \frac{k}{k_n}q = \frac{q}{n}$$

Along the Al <111> directions, the higher-order peaks listed in Tab. 5 have been observed. The calculated $q$-values of the Bi reflections have been listed in Tab. 3.

| Calculated $q_n$ Å$^{-1}$ | Reflection | $n$ |
|---|---|---|
| 0.537 | Al {111} | 5 |
| 0.672 | Al {111} | 4 |
| 0.896 | Al {111} | 3 |
| 1.075 | Al {222} | 5 |
| 1.344 | Al {111} | 2 |
| 1.612 | Al {333} | 5 |
| 1.792 | Al {222} | 3 |
| 2.016 | Al {333} | 4 |
| 2.150 | Al {444} | 5 |
| 4.031 | Al {333} | 2 |

*Table 5. Calculated position of the observed higher order aluminium reflections.*

Only the (111), (110), (222), and (220) reflections of bismuth have been observed in the x-ray diffraction measurements.

**Data reduction**

Figure 11 shows longitudinal scans along the aluminium (111) direction. The Bi (110) reflection (at $q \sim 1.922$ Å) and the Al (222) higher-order ($\lambda/3$) reflection (at $q \sim 1\ 793$ Å) are shown before, under, and after the second temperature cycle on sample X-1. The absence of the Bi peak at 541 K (Fig. 11b) is assigned to the inclusions being liquid.

The data have been processed in two ways: by summing the counts in the peaks and by fitting Gaussian functions to the peaks. To obtain a measure of the intensity of the peaks in the longitudinal scans, the counts in each peak are summed after subtracting the background, which is determined by fitting a line through the points next to the peaks (see Fig. 12). The background increases vaguely with increasing $q$. This is caused by the tail of the Al (111) Bragg peak at $q \sim 2.768$ Å$^{-1}$ (see Fig. 10 on page 24). The intensity derived by summing counts in a longitudinal scan is not the integrated intensity, which should be calculated from scans in three dimensions. However, the present measurements were performed with slits, which were well opened. Therefore, changes of the three-dimensional shapes of

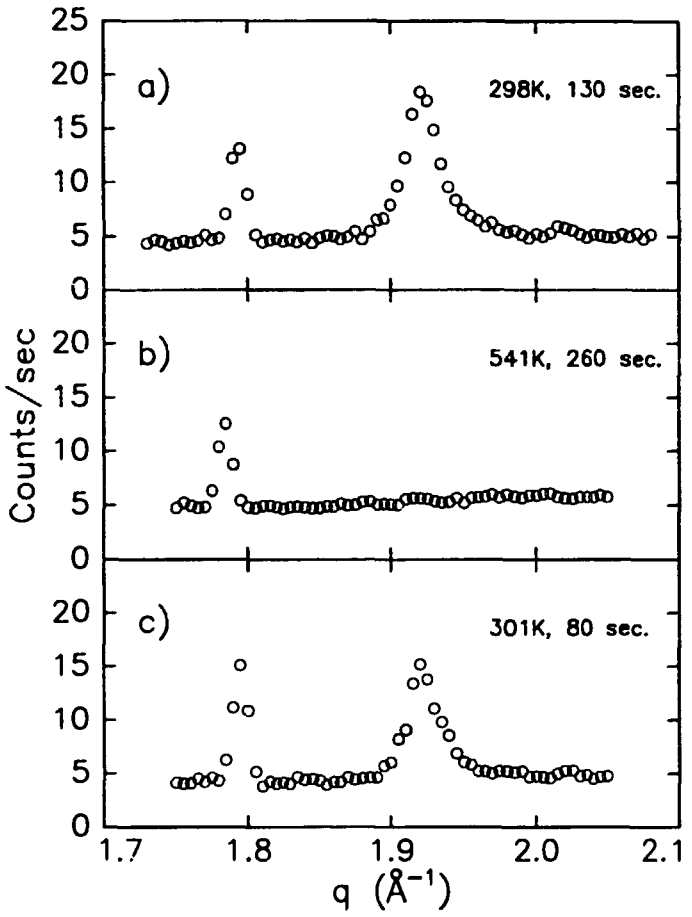


*Figure 11. Longitudinal scans of sample X-1 along the aluminium (111) direction showing the Bi (110) reflection and the Al (222) higher-order (λ/3) reflection. a) At room temperature before the temperature cycle. b) At 541 K where the Bi had melted. c) At room temperature after the temperature cycle. The counting time per point is indicated in the figures.*

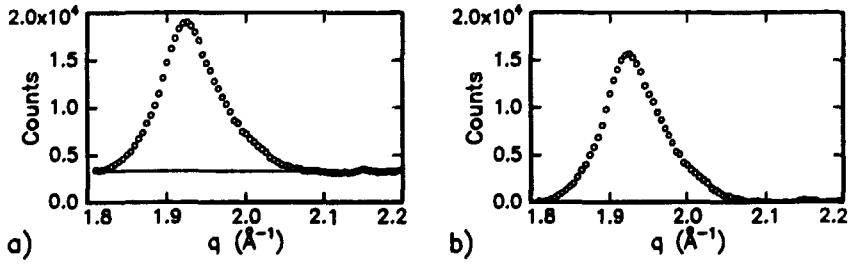


*Figure 12. Background subtraction from longitudinal scan of sample X-2 at 298 K. a) Line fitted to the data points next to the peak. b) Scan after background subtraction.*

the peaks are not expected to cause significant differences between the qualitative behaviours of the measured intensity and integrated intensity.

The second method consists of fitting Gaussian functions to the peaks and a line to the background simultaneously. The peak shape is only approximately Gaussian as can be seen in Fig. 13.

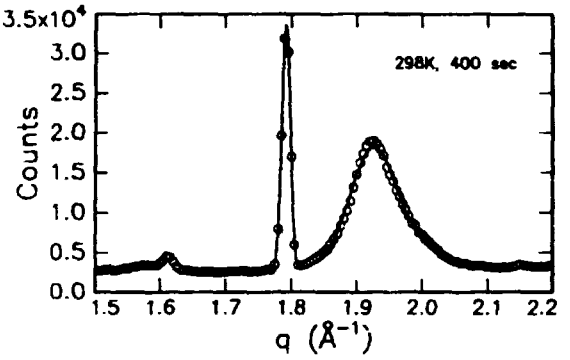


*Figure 13. Same scan as in Fig. 12 with Gaussian fits to the peaks. The range of q-scale has been changed.*

However, when the counting statistics are sufficiently good the fits give fairly precise values of the peak positions ($\pm 4 \cdot 10^{-4}$ Å$^{-1}$) and the full width at half maximum ($\pm 9 \cdot 10^{-4}$ Å$^{-1}$).

**The results**

Figure 14 shows an overview of the data from the second temperature cycle on sample X-1. The details of these data will be discussed in the following sections. Attention is drawn to the fact that the intensity, mean radius, and lattice spacing of the inclusions show an almost linear temperature dependence up to a temperature (around 475 K for the heating data), approximately at which the curves of the Bi data all bend, whereas the Al lattice spacing in Fig. 14d increases linearly in the whole temperature range. This effect is interpreted as a result of the onset of melting of the inclusions at this temperature. That melting occurs so far below the bulk melting point is confirmed by transmission electron microscopy (see section 4.4). The melting transition is wide, as the signal disappears only right at the bulk melting point. Solidification starts at around 440 K, *i.e.* the solid-liquid transition shows a large hysteresis (around 100 K wide). Similar to the melting transition, the solidification of the inclusions proceeds gradually over a temperature range, which is around 70 K wide. As will be discussed in section 5.4, the measured widths of the transitions are smaller in the channeling measurements, but the fact that no superheating, but a large supercooling are observed is confirmed.

The width of the hysteresis of the solid-liquid phase transition is of the same order of magnitude as found for lead inclusions in aluminium by Gråbæk *et al.*[23], but translated to lower temperatures compared to the bulk melting point. A simple, qualitative argument for this translation could be that while lead expands (contracts) when melting (solidifying), bismuth contracts (expands). The confinement of the inclusions could hinder the melting of lead and ease the melting of bismuth and the other way round for solidification. Quantitative predictions, however, would demand a more careful analysis, which have not been the object in the present work.

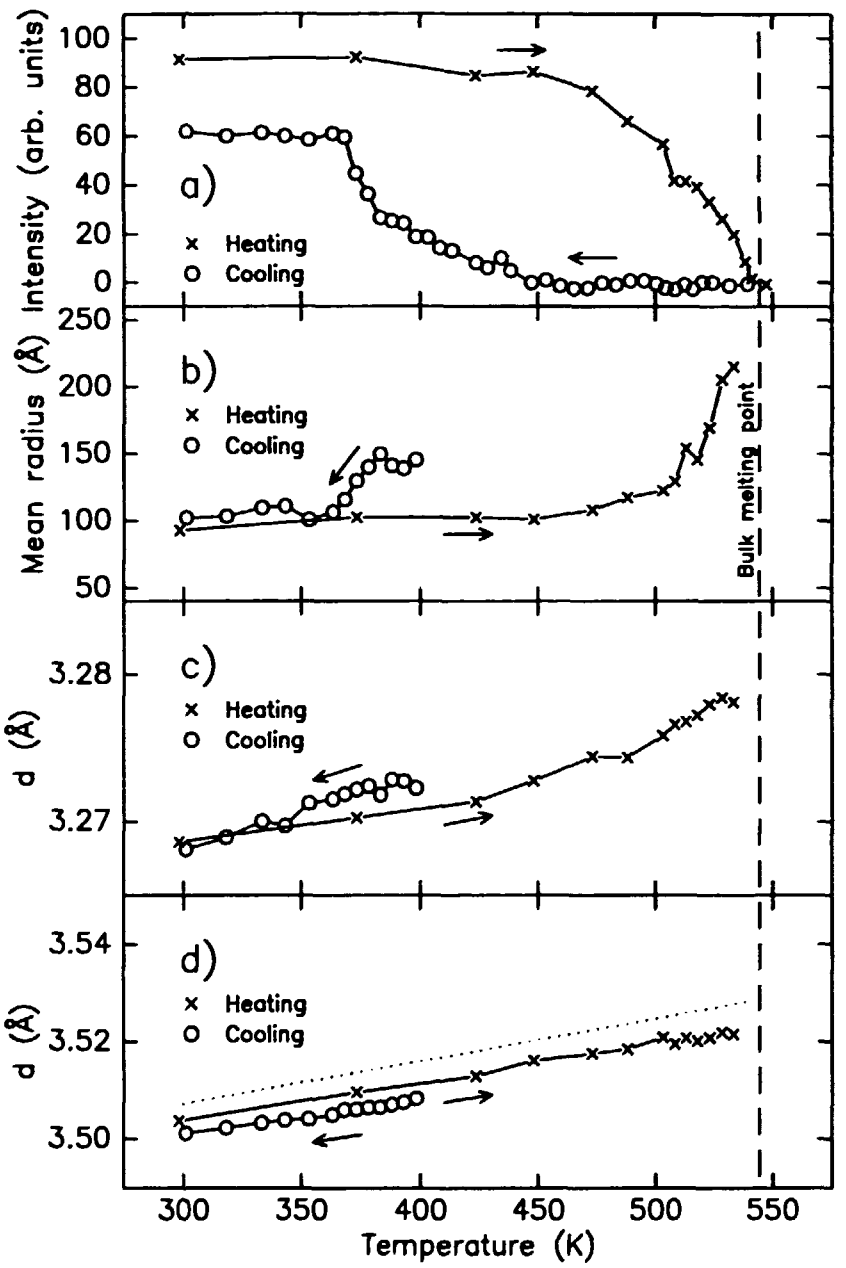


*Figure 14. X-ray data for the Bi (110) reflection from the second temperature cycle on the sample X-1. The dashed line indicates the bulk melting point of Bi (544.5 K[10]), the full lines are guides to the eye. a) Intensity. b) Inclusion mean radius ($\bar{r}$). c) Lattice spacing $d = 2\pi/q$. d) Lattice spacing of Al (222) $\lambda/3$ reflection. The dotted line is the theoretical curve ([69, 71]).*

**Intensity**

Figure 15 shows a logarithmic plot of the intensity of the bismuth (110) reflection during the second heating and cooling sequence on sample X-1.

As mentioned in section 3.1, the decrease of the intensity $I$ with increasing temperature can be described by a Debye-Waller factor: $I = I_0 \exp(-2M)$. A linear fit to the logarithmic intensity of the heating data in the temperature range from 298 to 450 K gives the Debye-Waller factor $\exp(-2M)$ with $2M = 0.00050T$. Fitting the cooling data yields the value $2M = 0.00045T$. The uncertainties on these values are large (around 50 %), reflecting the low statistics of the data and the fact that the values depend strongly on the slope of the lines. Similarly for sample X-2, values of $2M$ from the heating data between $0.00021T$ (when fitting in the temperature range 298–423 K) and $0.00046T$ (fitting 298–473 K) and the value $2M = 0.00040T$ from the cooling data have been found. As sample X-2 had not previously been heated, changes in the intensity caused by other reasons (*e.g.* growth of inclusions, change in the orientations of the inclusions, and segregation to the surface) than change in the thermal vibrations are likely to occur, and furthermore it is harder to distinguish, at which temperature melting sets in, when looking at the intensity data alone. For both samples the values of $2M$ all lie within the limits calculated from tabulated Debye temperatures (see Fig. 6).

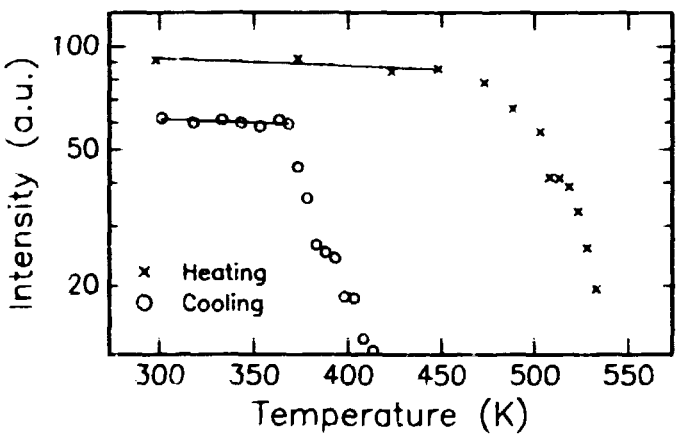


*Figure 15. Logarithmic plot of the intensity of the bismuth (110) reflection during the second heating and cooling sequence on sample X-1.*

As seen in Fig. 15 the levels of the intensity before and after the second heating sequence are not the same. However, after the third heating sequence, the level before the second one was recovered. This indicates that difference in room temperature intensity levels is caused by resolidification of inclusions in different orientations. Aluminium has four equivalent {111} planes, and the inclusions parallel to only one of these are observed.

An estimate of the root mean square $\sqrt{\langle \Delta x^2 \rangle}$ of the component of the displacement normal to the reflecting planes has been calculated in Fig. 16 from the heating data in Fig. 15 using

$$\sqrt{\langle \Delta x^2 \rangle} = \frac{\sqrt{\ln(I_0/I)}}{q},$$

which is derived from Eq. 15 in Section 3.1.

As mentioned above, melting sets in at approximately 475 K. At this temperature the root mean square displacement is around 12 % in qualitative agreement

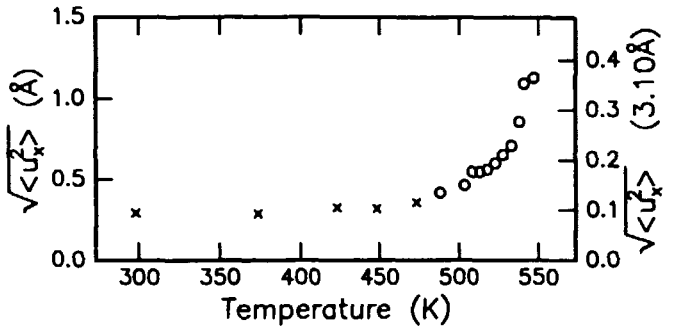


*Figure 16. Root mean square displacements calculated from the heating data in Fig. 15. The right axis is in units of the nearest-neighbour distance 3.10Å[71].*

with the Lindemann criterion, which says that a crystal melts when the root mean square displacement is larger than a certain fraction of the interatomic distance (see section 2.2). The root mean square displacements are high (around 10%) at lower temperatures too, which may be explained by the uncertainty on fitting a line to only four points. In this case the Lindemann criterion therefore does not give any independent information on the melting temperature. The points marked with circles should not be ascribed any physical meaning, because the decrease in intensity reflects the melting of inclusions and not a (for all inclusions) general increase in the vibration amplitude as expressed by the Debye-Waller factor.

For the sample X-2 which had not previously been annealed, the first heating sequence was accompanied by a large loss of intensity (around 90% was lost). Rutherford backscattering measurements before and after the heating sequence showed that the main reason for this was the loss of Bi from the sample.

The decrease of the intensity during melting is analysed in the section "Size-dependent melting" starting on page 34.

### Size of the inclusions

Table 6 sums up the size data of the x-ray samples at room temperature. The Bi (111) reflection was observed only prior to the heating of the samples. Its full width at half maximum is smaller than the one of Bi (110). A possible interpretation is that the inclusions lying in this orientation are larger than the ones lying with their {110} planes parallel to the Al {111} planes. However, after the annealing the mean size of the inclusions is larger, yet no inclusions are seen in the former orientation, as would be expected if this was the preferred orientation of the larger inclusions. Alternatively, the smaller FWHM can be caused by the presence of the close-lying Al {333} $5^{th}$ order reflection, which is narrower and gives a significant contribution to the intensity in this $q$-range. Though two peaks were found here when fitting, the fits may not have separated the peaks correctly.

The mean size (measured on the Bi (110) peak) of the inclusions in sample X-1 at room temperature has increased from the initial value by 23% (or more) after the first temperature cycle and by 10% (or less) during the second cycle, but it has not changed during the third cycle. This behaviour signifies that the the sample has reached a state, in which no further growth of inclusions is feasible. It is expected that the largest growth occurs when the sample has not been annealed previously. The mean size of the inclusions in sample X-2 has increased by 45% after the first temperature cycle. As the mean size of the inclusions in sample X-2 was smaller than that of sample X-1, a larger relative increase was expected.

| Sample | Cycle | Peak | FWHM ($Å^{-1}$) | | Size (Å) | |
|---|---|---|---|---|---|---|
| | | | before | after | before | after |
| X-1 | 1 | Bi (111) | 0.0358(8) | - | 186(6) | - |
| X-1 | 1 | Bi (110) | 0.042(2) | 0.034(2) | 151(9) | 200(20) |
| X-1 | 2 | Bi (110) | 0.0324(10) | 0.0298(11)* | 186(7) | 205(9)* |
| X-1 | 3 | Bi (110) | 0.0298(11)* | 0.0299(10) | 205(9)* | 205(8) |
| X-2 | 1 | Bi (111) | 0.067(4) | - | 87(6) | - |
| X-2 | 1 | Bi (110) | 0.0861(10) | 0.061(4) | 66.1(8) | 95.5(6) |

*Table 6. Measured full widths at half maximum (FWHM) of the Bi peaks (before and after the temperature cycles) and mean sizes (Eq. 12) deconvoluted for the measured resolution given in Tab. 4. The two pairs of values marked * are the same data point.*

Figure 14b shows the evolution of the mean radius (defined as half the mean size given by Eq. 12) during second temperature cycle derived from the FWHM of the Bi (110) reflection. The mean size is seen to increase in the temperature range where the intensity of the peak decreases. Two interpretations of the increasing mean size are evident: the inclusions are growing or the smaller inclusions are melting first. (For lead inclusions in aluminium it was found[33] that the larger inclusions melted first and solidified last.) However, as seen in Tab. 6 and directly from Fig. 14b by comparing the levels of the heating and cooling data, the mean size at room temperature has not increased comparably, disproving the former interpretation. Likewise, the cooling data in Fig. 14b indicates that the larger inclusions solidify first. The observations that the smaller inclusions melt first and the larger ones solidify first agree qualitatively with the models of melting and solidification, which were mentioned in Section 2.2. Figure 17 shows the resolution corrected mean size calculated from the full width at half maximum of the Bi (110) reflection during heating and cooling of sample X-2. The mean size of the inclusions in sample X-2 is approximately a factor two smaller that the one of sample X-1, but the qualitative behaviour is the same.

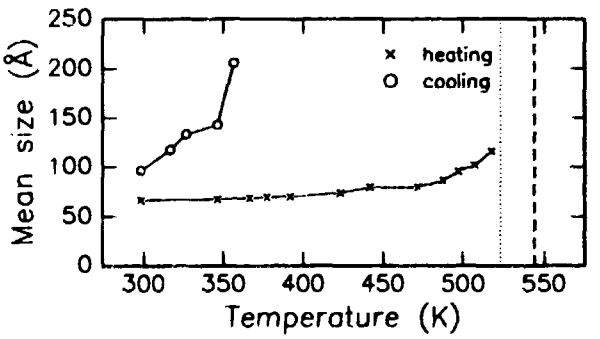


*Figure 17. Deconvoluted mean size ($2\bar{r}$) calculated from the FWHM of the Bi (110) reflection from the sample X-2. The dashed line indicates the bulk melting point of Bi and the dotted line shows the approximate temperature at which the Bi signal vanishes.*

### Lattice parameter of the inclusions

The lattice spacing between the Bi (110) planes is shown as a function of temperature in Fig. 14c for the second temperature cycle of sample X-1 and in Fig. 18 for

sample X-2. In Fig. 14d the lattice spacing of the Al (222) $\lambda/3$ peak is shown, to confirm the stability of the angles of the spectrometer. The dotted lines in the two figures are the theoretical curves calculated from the tabulated values of the lattice constant and thermal expansion coefficient of aluminium[71, 69]. The full line in Fig. 18 is a linear fit to the data. The coefficient of linear expansion from this fit is $18(2)\cdot10^{-6}\,K^{-1}$, which lies between the tabulated values for Bi ($13\cdot10^{-6}\,K^{-1}$) and Al ($29\cdot10^{-6}\,K^{-1}$)[27]. If the Bi inclusions are under pressure from the confining Al lattice, they are not free to expand as bulk Bi and their coefficient of expansion may be different from the bulk value. For the sample X-1 values between $7.9(11)\cdot10^{-6}\,K^{-1}$ and $16.3(12)\cdot10^{-5}\,K^{-1}$ have been found, indicating the influence of the confinement.

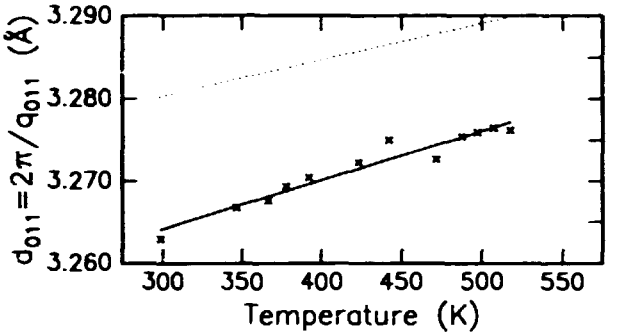


*Figure 18. Lattice spacing $d = 2\pi/q$ of the Bi (110) reflection during the heating of sample X-2. The full line is a linear fit to the data and the dotted line is the theoretical curve.*

The lattice parameter of the inclusions obtained from measurements is smaller than the bulk value at all temperatures. This may be taken as a sign that the inclusions are under high pressure. High pressures (1–2 GPa) have been reported for noble gas inclusions in aluminium[61]. For lead inclusions with a mean size ($2\bar{r}$) of 140 Å an upper limit on the pressure is estimated to be 0.18 GPa[22, 23]. At room temperature before the second temperature cycle on sample X-1 the measured value for the lattice parameter of bismuth is $a_m = 4.729$ Å and the tabulated value $a_0 = 4.7459$ Å[71]. From the bulk modulus $K = 31.1$ GPa[35], an estimate can be made of the corresponding pressure of the bismuth inclusions as $\Delta p = K(a_0^3 - a_m^3)/a_0^3 = 0.33$ GPa. This is the same order of magnitude as the pressures found in thallium inclusions in aluminium (see Section 2.1)[45]. Another possible explanation for the smaller lattice parameter is a distortion of the lattice. Since the bulk rhombohedral structure may not fit the aluminium fcc structure very well, this may be the case. Conclusive evidence for or against this hypothesis can be provided by measuring reflections from other families of lattice planes. A larger distance between lattice planes in another direction would support the hypothesis of a distortion, while a smaller distance would favour high pressure on the inclusions. Unfortunately the observations of the Bi {111} reflection from the two samples did not allow for a sufficiently precise determination of the lattice spacing.

### The effect on the melting transition of a pressure

If no other factors are involved in the process of melting, a pressure would decrease the melting temperature of bismuth. The change in melting temperature can be

estimated using the Clausius-Clapeyron equation[48]

$$\frac{dp}{dT} = \frac{L}{T_B \Delta V},$$

which predicts an decrease (increase) of the melting temperature when $\Delta V$ is negative (positive). $L = 10.89\,\mathrm{kJ/mol}$[10] is the latent heat of melting The change in molar volume, $\Delta V = -0.722\,\mathrm{cm^3/mol}$, is calculated from the relative volume change during melting, $\Delta v = -0.0335$[10]. In the temperature range of melting the values of $\Delta p$ lie between 0.33 and 0.41 GPa. Combining $dp/dT = -0.028\,\mathrm{GPa/K}$ with an average value of $\Delta p = 0.37\,\mathrm{GPa}$ gives $\Delta T = -13\,\mathrm{K}$. This $\Delta T$ is an upper limit on the shift in temperature of the melting phase transition, as $\Delta p$ is an upper limit on the pressure Since an x-ray diffraction signal is seen in all measurements at temperatures up to immediately below the bulk melting point, it appears that melting of the inclusions below the bulk melting point of bismuth cannot be explained solely in terms of an overpressure. It should be stressed that on the basis of a single x-ray reflection there is no conclusive evidence of an overpressure.

**Size-dependent melting**

The decrease of the intensity takes place over a wide temperature range (around 100 K) and at the same time the mean size of the inclusions grows, indicating that what is observed is size-dependent melting.

To compare the x-ray data and the two models of melting (Eq 1–2, see Section 2.2) it is necessary to parameterise the size distribution of the Bi inclusions Let $s(r)$ denote the distribution of Bi atoms as a function of the radius $r$ of the inclusion to which they belong. To describe this distribution a "hat"-shaped function (sum of two sigmoidal functions):

$$h(r, r_1, r_2, \beta) = \frac{\exp(\beta(r - r_1))}{1 + \exp(\beta(r - r_1))} + \frac{\exp(-\beta(r - r_2))}{1 + \exp(-\beta(r - r_2))} - 1 \qquad (17)$$

is used. A distribution function which is the weighted sum of two "hat" functions ($h(r, r_{i1}, r_{i2}, \beta_i)$) with different positions $r_{ij}$ of the sides of the "hat" is also used. The parameter $\beta_i$ determines the sharpness of the corners of the $i^{th}$ "hat", $n$ is the number of "hat" functions, and $w$ is the weight ($s(r) = w\,h(r, r_{11}, r_{12}, \beta_1) + (1 - w)\,h(r, r_{21}, r_{22}, \beta_2)$). The distribution functions are normalized to give a total number of atoms of one

The model intensities have been multiplied by a Debye-Waller factor. The model intensity is then calculated as

$$I(T) = I_0 \exp(-2M) \cdot (1 - \int_0^{r(T)} s(r)\mathrm{d}r). \qquad (18)$$

The radius $r(T)$ of particles melting at the temperature $T$ is given by the models. For model A (developed by Pawlow[46]) the result is

$$r(T) = \left(1 - \frac{T}{T_B}\right) \frac{L\rho_s^{1/3}}{2} \left(\frac{\gamma_s}{\rho_s^{2/3}} - \frac{\gamma_l}{\rho_l^{2/3}}\right)^{-1}, \qquad (19)$$

where $T_B = 544.5\,\mathrm{K}$[10] is the bulk melting point, and $L = 10.89\,\mathrm{kJ/mol}$[10] the latent heat of melting. The density of the solid phase $\rho_s = 9.70\,\mathrm{g/cm^2}$ is calculated using the linear coefficient of thermal expansion of bismuth, $\alpha_{Bi} = 13.4 \cdot 10^{-6}\,\mathrm{K^{-1}}$[10], the density of the liquid phase is $\rho_l = 10.07\,\mathrm{g/cm^2}$[69], and the (isotropic) surface free energy of the solid and liquid phases are $\gamma_s = 550\,\mathrm{mJ/m^2}$[41] and $\gamma_l = 378\,\mathrm{mJ/m^2}$[10], respectively. The radius given by model B (formulated by Wronski[70]), which assumes a thin molten layer of thickness $\delta$ around a solid core, is

$$r(T) = \frac{1}{2}\left(\delta + \frac{2K_1}{T\gamma_s L} + \sqrt{\delta^2 + (\frac{2K_1}{T\gamma_s L})^2 + 2\delta\frac{2K_2}{T\gamma_s L}}\right), \qquad (20)$$

where $\gamma_{sl} = 54.4\,\mathrm{mJ/m^2}$[66] is the solid-liquid interfacial energy, $K_1 = \gamma_{sl} + \gamma_l(1 - \rho_s/\rho_l)$, $K_2 = \gamma_{sl} - \gamma_l(1 - \rho_s/\rho_l)$, and $r$ is the total radius of the partly liquid particle.

Figure 19a shows the results of iterative fits to the data from the second temperature cycle on sample X-1. When the distribution function consists of only one "hat", the resulting curves do not fit the data very well, regardless of the model used for the size dependence of the melting temperature (see Fig. 19a). The slope of the melting curve at high temperatures cannot be reproduced with a single "hat". The parameters obtained from the fits are given in Table 7, and the size distributions corresponding to these values are drawn in Fig. 19b. As the distributions are quite broad (low values of $\beta_i$), the fits are not very sensitive to the positions $r_{ij}$, but the mean value and approximate shape of the distribution are well determined. When two "hats" are included in the fit, the resulting size distribution has a peak at low sizes and a tail of larger inclusions, corresponding to the bump in the intensity data between 508 K and the Bi bulk melting point. To check that the resulting size distributions do not depend critically on one point, the fit is repeated excluding the point at 508 K (marked with an arrow), which seems to disagree the most with curves obtained from fitting with only one "hat". It turns out that if this point is excluded from the fit, the results are not significantly changed. The use of Gaussian distribution functions (instead of the sum of two sigmoidal functions) yielded similar results.

| Model | A | B | A | B |
|---|---|---|---|---|
| $n$ | 1 | 1 | 2 | 2 |
| $r_{11}$ (Å) | 0 | 0 | 46 | 61 |
| $r_{12}$ (Å) | 66 | 105 | 110 | 45 |
| $\beta_1$ | 0.0093 | 0.043 | 0.093 | 0.26 |
| $r_{21}$ (Å) | - | - | 0 | 0 |
| $r_{22}$ (Å) | - | - | 220 | 119 |
| $\beta_2$ | - | - | 0.0047 | 0.0134 |
| $w$ | - | - | 0.557 | 0.559 |
| $\bar{r}$ (Å) | 129 | 62 | 108 | 44 |
| $\delta$ (Å) | - | 5.7 | - | 4.1 |
| $I_0$ (a.u.) | 101 | 100 | 95 | 97 |
| $2M/T$ ($\mathrm{K^{-1}}$) | 0.00043 | 0.00065 | 0.00027 | 0.00037 |

*Table 7. Fit parameters and mean radii ($\bar{r}$) derived from the parameters.*

Model A and model B give different size distributions. The size distributions which were found using model B (Eq. 2) generally have a high concentration of Bi atoms in inclusions smaller than a 100 Å, leading to mean sizes considerably smaller (see Table 7) than the experimentally determined value $\bar{r} \approx 100$ Å (see Fig. 14b). Although model A and model B give practically indistinguishable fits to the data, the corresponding mean sizes suggest that model A is the most appropriate for our data.

The values found for $2M$ vary strongly from one fit to another. As remarked above (page 30) the uncertainties are large, so only the order of magnitude is expected to be correct.

Figure 20 shows the results of iterative fits to the data from the second temperature cycle on sample X-2 and the resulting size distributions. The data are fitted well with only one "hat" included in the distribution function. The parameters from the fits are found in Tab. 8.

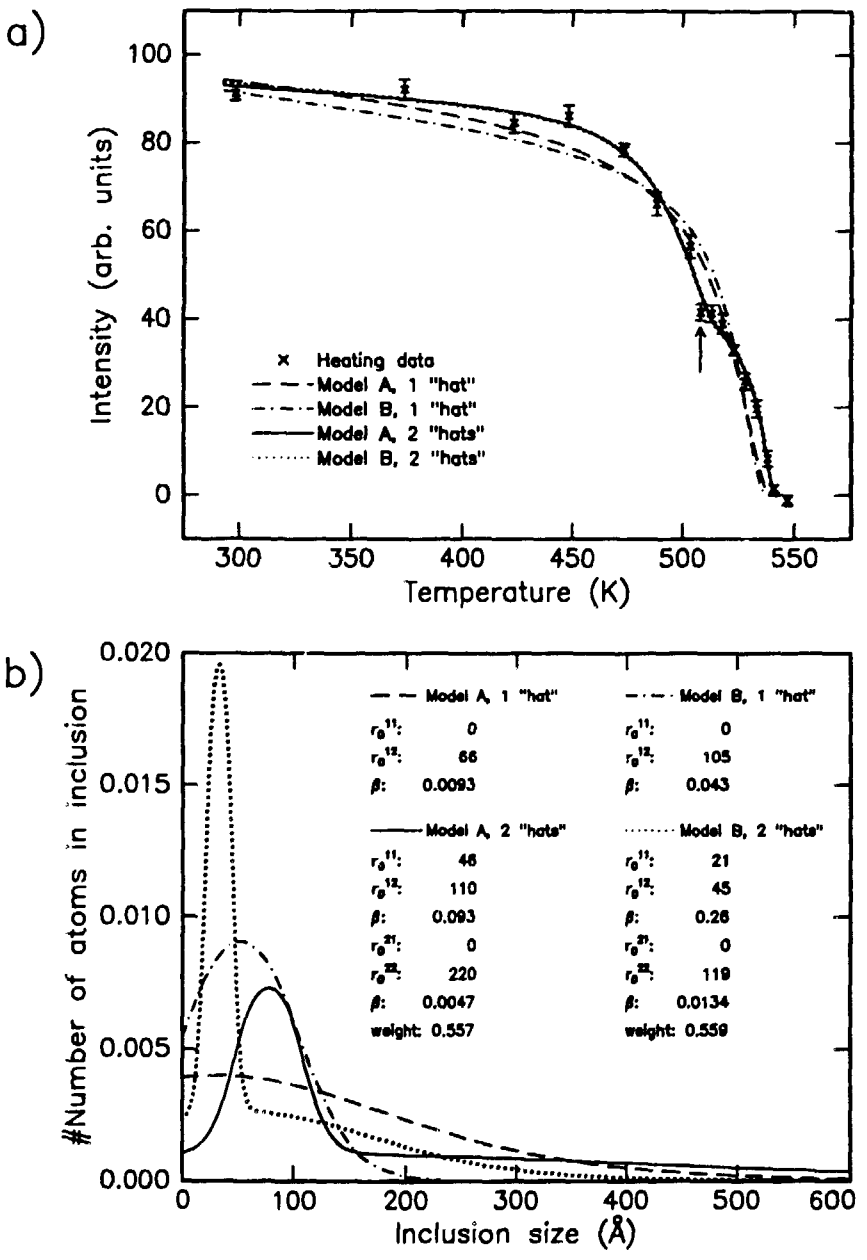


*Figure 19. Comparison of x-ray data from the second temperature cycle on sample X-1 and the models. a) Fits to the x-ray data. b) Corresponding distributions of Bi atoms on inclusions, characterized by their size r. The full and the dashed lines correspond to model A (Eq. 1); the dotted and the dash-dot lines correspond to model B (Eq. 2) (see Tab. 7 for the parameters and mean sizes).*

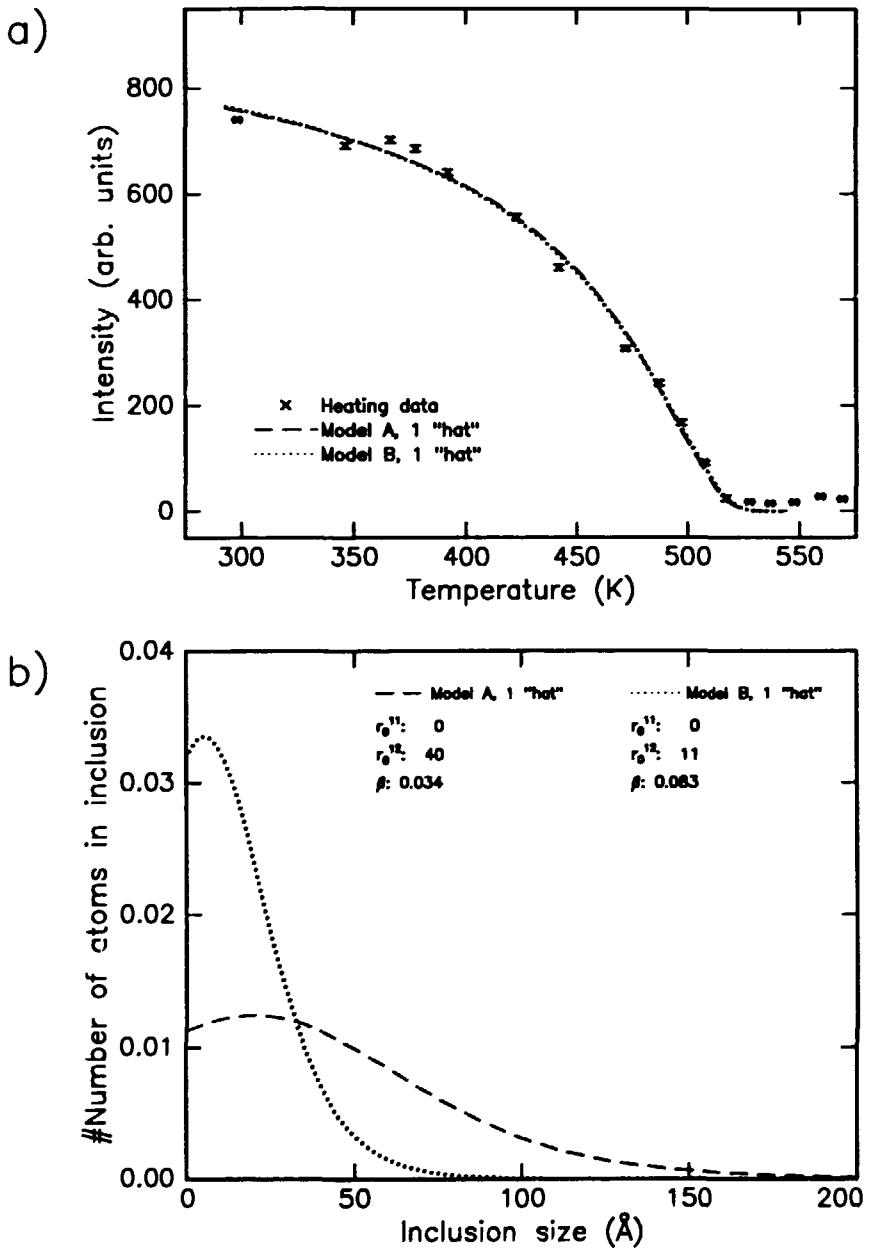


*Figure 20. Comparison of x-ray data from the temperature cycle on sample X-2 and the models. a) Fits to the x-ray data. b) Corresponding distributions of Bi atoms on inclusions, characterized by their size r. The dashed lines correspond to model A (Eq. 1); the dotted lines correspond to model B (Eq. 2) (see Tab. 8 for the parameters and mean sizes).*

| Model | A | B |
|---|---|---|
| $r_1$ (Å) | 0 | 0 |
| $r_2$ (Å) | 40 | 11 |
| $\beta$ | 0.034 | 0.083 |
| $\bar{r}$ (Å) | 41 | 15 |
| $\delta$ (Å) | - | 1.1 |
| $I_0$ (a.u.) | 938 | 988 |
| $2M/T$ ($K^{-1}$) | 0.00020 | 0.00020 |

*Table 8. Fit parameters and mean radii ($\bar{r}$) derived from the parameters. The data are fitted including only one "hat" in the distribution function.*

As found for the data from sample X-1, model B gives an unrealistically small value for the mean size, whereas the value obtained using model A is close to the value ($\bar{r} \approx 40$ Å) derived from the full width at half maximum. It is therefore concluded that Model B, which assumes a thin molten layer around a solid core, does not give a good description of the inclusions.

As the models describe free particles, agreement between the models and the data for confined Bi crystallites should not be expected *a priori*. In addition the models do not take into account the effects of pressures in the inclusions or the existence facets. Several authors have observed that for lead inclusions in aluminium melting starts as a roughening transition of the {100} facets, where the melting nucleates[54, 42]. The same phenomenon has been observed for indium inclusions in aluminium[53].

# 4 Transmission electron microscopy

After an introduction to the transmission electron microscope, the image formation in the microscope and the origin of moiré patterns are discussed shortly. In Section 4.3 the orientations of the inclusions with respect to the aluminium matrix are discussed on the basis of electron diffraction patterns. Section 4.4 deals with the results of *in situ* temperature cycles in the transmission electron microscope.

## 4.1 The microscope

The transmission electron microscopy was performed in the Philips CM 20 microscope at the Orsted Laboratory of the University of Copenhagen (see Fig. 21 ) The microscope operates at acceleration energies up to 200 keV. A description of the microscope can be found in [51]. The relativistic wavelength of 200 keV electrons is 2.51 pm, however, due to lens aberrations, the resolution of the microscope is limited to a few angstrom. Two different sample holders were used in the micro-

*Figure 21. The Philips CM 20 microscope at the Orsted Laboratory of the University of Copenhagen*

scope. Holder 1 has two mutually perpendicular horizontal axes, around which the sample can be rotated ±30° and ±60°, respectively. In holder 2, it is possible to

heat the sample in the microscope, while it is studied. In this holder the sample can be tilted ±60° around only one axis.

The transmission electron microscopy samples are polycrystalline, and usually several different crystallographic orientations of the aluminium grains can be found in the sample around the hole made by electro-polishing. The orientation of the grains with respect to the beam is adjusted by using the tilt(s). The selector diaphragm is used to select the area of interest for diffraction patterns. The electromagnetic lenses in the microscope allow magnifications between 25 and 750 000 times. With a (typical) magnification of 115 000, 1 cm on the negatives corresponds to $\sim 90\,nm$.

## 4.2 Image formation in the transmission electron microscope

On the whole, two kinds of pictures were recorded: selected area diffraction images and direct-space images. The images can either be seen on a fluorescence screen in the bottom of the microscope or on a video screen through a video camera, or recorded on a photographic negative by a camera in the microscope.

One source of contrast between the Al grains and the Bi inclusions in direct-space images is the effect that Bi scatters electrons more effectively than Al. In addition, crystal structures with different lattice spacings diffract the electrons in different angles, according to the Bragg relation (Eq. 4). This is the main source of contrast in the direct-space images. When a diaphragm (the objective diaphragm) is inserted in the back-focal plane (diffraction plane) to block electrons scattered away from the direct electron beam, the resulting image will show Bi inclusions as darker spots compared with the surrounding aluminium (see Fig. 22a). This is called a bright-field (BF) image. If a diffracted electron beam is used for image formation, instead, the objects causing this diffraction will appear bright in dark surroundings, a so-called dark-field (DF) image (see Fig. 22b).

When the objective diaphragm is taken out and the intermediate lens images the diffraction plane of the objective lens, the image of a planar intersection of reciprocal space of the area of the sample selected by the selector diaphragm is projected to the screen. This is called selected area diffraction (SAD) (an example is seen in Fig. 22c). The brightest spots stem from the aluminium fcc lattice, while fainter spots originate from the bismuth crystallites. Apart from the primary Bi spots multiple diffraction yields faint spots, *e.g.* around the central spot. An estimate of the lattice spacing of the diffracting planes can be made from the SAD image. As the image is subjected to aberration caused by the lenses and by deviations in the energy of the electrons, the lattice spacings are calculated by comparing the distance between symmetrically lying pairs of Bi spots to the distance between the closest pair of Al spots.

When two sets of equidistant parallel lines with slightly different interline distance (lattice distance) are superimposed, a new line pattern is created (see Fig. 23). This is called a moiré pattern. The distance between the fringes in the moiré pattern is[28]

$$D = \frac{d_1 d_2}{\sqrt{d_1^2 + d_2^2 - 2 d_1 d_2 \cos\phi}}, \tag{21}$$

where $d_1$ and $d_2$ are the interline distances of the superimposed line patterns and $\phi$ the angle between the line patterns. If the two line patterns are parallel ($\phi = 0$),

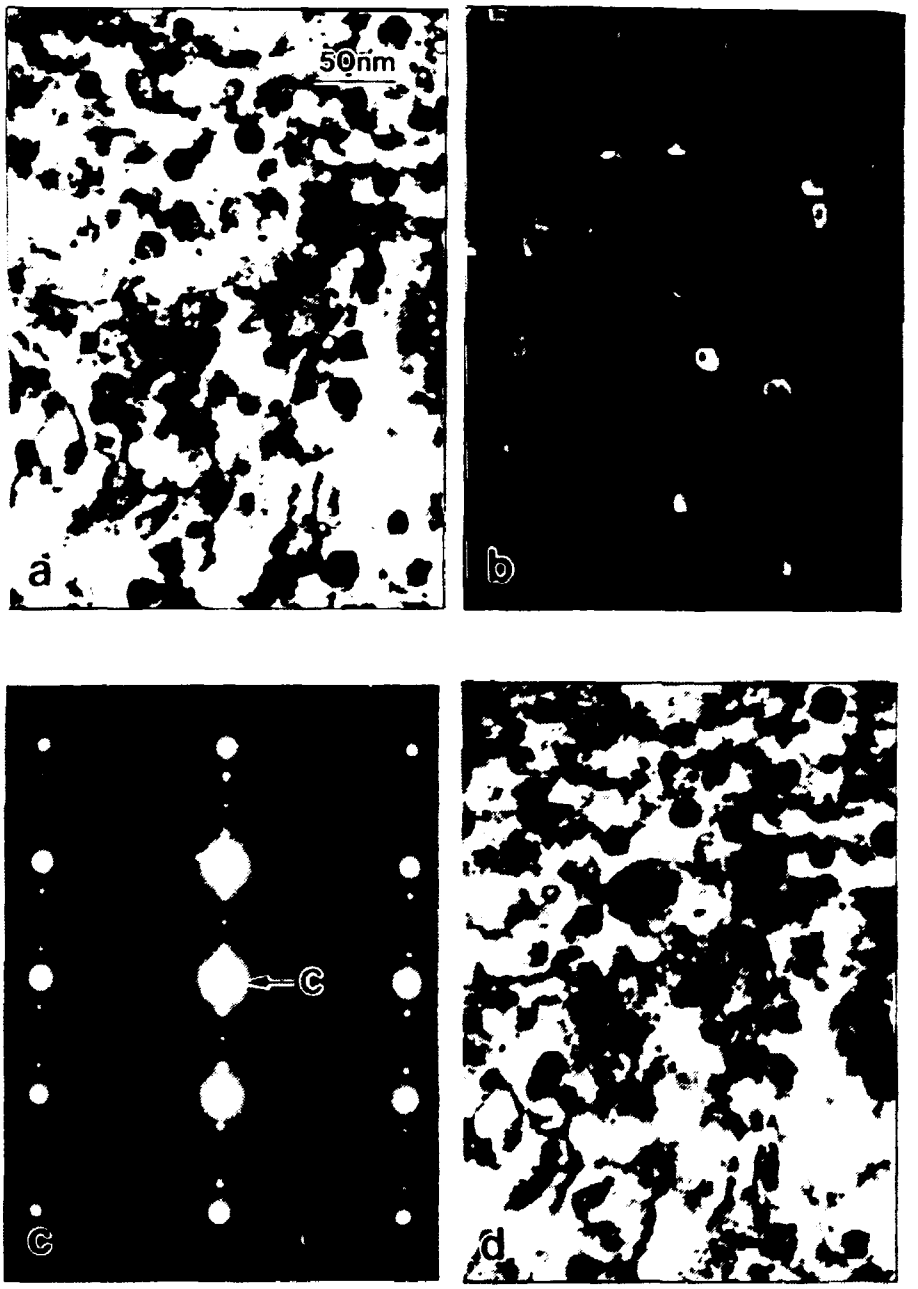


*Figure 22. Transmission electron microscope images of sample TEM-1 in the* $\{112\}_{Al}$ *orientation, 230 000 times magnified. a) Bright-field image using the central spot alone. b) Dark-field image using the* $<110>_{Bi}$ *reflection c) Selected area diffraction image. C is the central spot. d) Bright-field image with central spot and adjacent Bi spots.*

Eq. 21 comes down to

$$D = \frac{d_1 d_2}{|\, d_1 - d_2 \,|} \tag{22}$$

In the bright-field image in Fig. 22d the double diffraction Bi spots (with $q$-value $Q$ equal to the difference between those of the nearest Al ({111}) and Bi ({110}) reflections) around the central spot in Fig. 22c are included in the beam, which creates the image. The interference between the aluminium and bismuth crystal lattices creates moiré patterns, as seen in Fig. 22d and many of the following images. The spacing of these patterns is $D = 2\pi/Q$, which is equivalent to Eq. 22. Inserting, as an example, the values $d^{Al}_{111} = 2.3380\,Å$ and $d^{Bi}_{110} = 3.2802\,Å$ calculated from tabulated lattice parameters[71], gives $D = 8.14\,Å$, in agreement with the length scale in Fig. 22d.

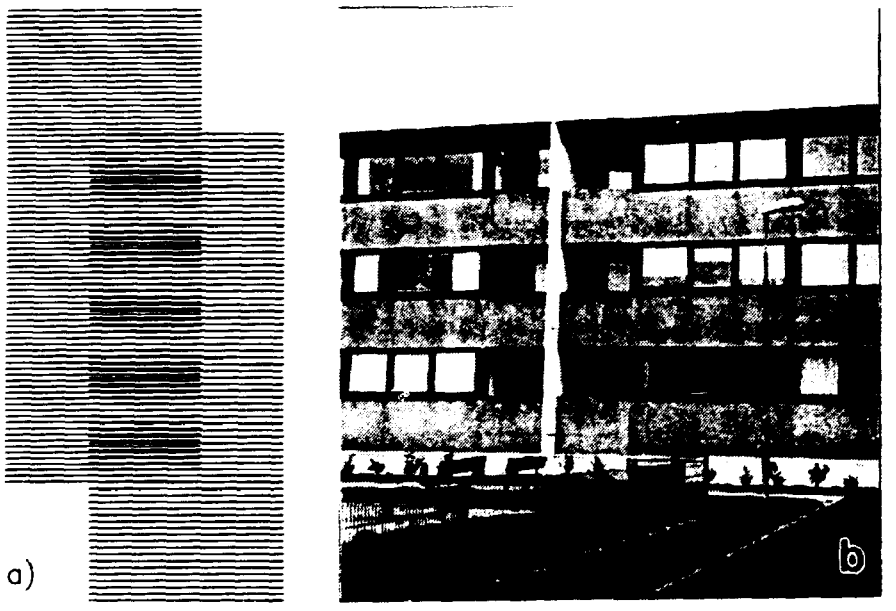


*Figure 23. a) Demonstration of moiré patterns ($\phi = 0$). b) Photo of two fences creating a moiré pattern.*

Figure 24 shows a bright-field image of an area of the sample TEM-1 at room temperature. The largest inclusions are found in the grain boundaries. Next to the boundaries there is a narrow inclusion-free zone, because the Bi has segregated to the boundaries, where the interfacial energy between Bi inclusions and Al host is lowered.

As previously mentioned, the TEM samples degenerated when exposed to air, meaning that it was possible to study a sample within only a short period (around one week). Therefore, either careful room-temperature studies or heating sequences have been performed on the samples, as indicated in Tab. 2 on page 15.

## 4.3 Orientation of the inclusions

Figure 25 shows a selected area diffraction image of the sample TEM-3 in the Al <001> orientation at room temperature. The measured lattice spacings (and $q$) of the Bi reflections in Fig. 25 are listed in Tab. 9. The identification of the reflecting planes given in Tab. 9 are based on the theoretical lattice spacings from


*Figure 24. Bright-field transmission electron microscope image of sample TEM-1 showing Al grains with Bi inclusions (dark spots). Note that the different orientations of the Al grains lead to contrast.*

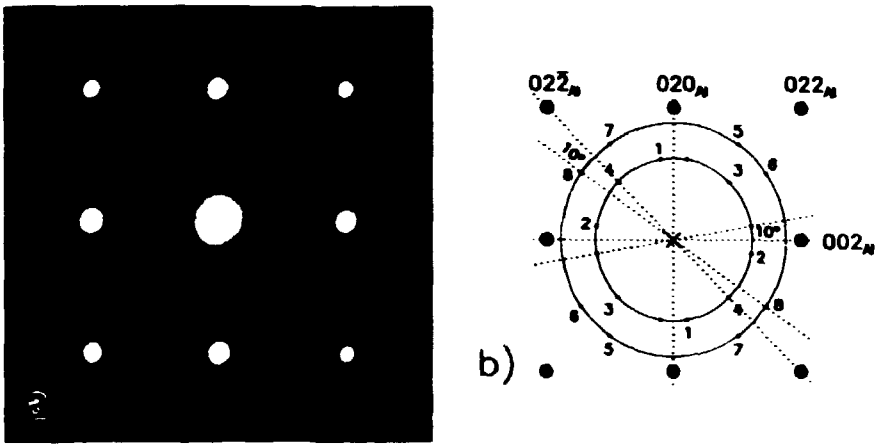


*Figure 25. a) Selected area diffraction image of sample TEM-3 from which an orientational relationship can be deduced. b) Schematic diffraction pattern*

Tab. 3, which have been transcribed to Tab. 10. The measured lattice spacings between {011} planes are shorter than the calculated one, indicating that the lattice is distorted or compressed. The lattice spacings between $\{01\bar{1}\}$ planes match the calculated one within the uncertainties. The precision of electron diffraction ($\pm 0.5\%$) is not sufficient to determine whether the lattice is distorted or compressed.

| Bi spot | Al reflections | $d$ Å | $q$ Å$^{-1}$ | Bi reflection |
|---|---|---|---|---|
| 1 | $(020),(0\bar{2}0)$ | 3.28 | 1.92 | {011} |
| 2 | $(002),(00\bar{2})$ | 3.31 | 1.90 | {011} |
| 3 | $(022),(0\bar{2}\bar{2})$ | 3.28 | 1.92 | {011} |
| 4 | $(02\bar{2}),(0\bar{2}2)$ | 3.26 | 1.93 | {011} |
| 5 | $(022),(0\bar{2}\bar{2})$ | 2.28 | 2.75 | $\{01\bar{1}\}$ |
| 6 | $(022),(0\bar{2}\bar{2})$ | 2.28 | 2.76 | $\{01\bar{1}\}$ |
| 7 | $(02\bar{2}),(0\bar{2}2)$ | 2.27 | 2.77 | $\{01\bar{1}\}$ |
| 8 | $(02\bar{2}),(0\bar{2}2)$ | 2.27 | 2.77 | $\{01\bar{1}\}$ |

*Table 9. Measured lattice spacings (and q) of the Bi reflections in Fig. 25. The first column gives the number of the Bi spots in Fig. 25, the second one tells which Al reflections has been used for calibration, and the last column gives the identification based on the d-values*

| Reflection | $d$ Å | $q$ Å$^{-1}$ | $\lvert F_{hkl}(\mathbf{q})\rvert^2$ a.u. |
|---|---|---|---|
| (011) | 3.2802 | 1.915 | 21074 |
| (112) | 2.3688 | 2.653 | 16797 |
| $(01\bar{1})$ | 2.2732 | 2.764 | 18342 |

*Table 10. Theoretical values of lattice spacings, q, and relative intensities of bismuth reflections.*

The theoretically calculated angle between the {110} and $\{01\bar{1}\}$ (or $\{10\bar{1}\}$) planes is 43.82°, and 136.18° between the {110} and $\{01\bar{1}\}$ (or $\{10\bar{1}\}$) planes. These angles are found (within the uncertainty of the measurement) in Fig. 25,

confirming the identification of the spots. However, it cannot be ruled out that the two families of reflections stem from different inclusions, thereby giving no basis for determining the exact orientational relationship. The Bi {110} reflections lie symmetrically approximately ±10° from the Al {001} reflection, as do the Bi $\{01\bar{1}\}$ reflections from the Al {011} reflection. Assuming that the Bi {110} and $\{01\bar{1}\}$ reflections stem from inclusions of the same relationship, the latter is determined to be approximately:

$$\{1, 12, 12\}_{Bi} \parallel \{200\}_{Al} \tag{23}$$

$$\angle([0\bar{1}1]_{Bi}, [011]_{Al}) \approx 10.0°. \tag{24}$$

Indices as large as (1,12,12) are unrealistic, and it should be noted that the angle between the Bi (011) and (1,12,12) planes is only 3.45°, which suggests that $\{011\}_{Bi} \parallel \{200\}_{Al}$ is a more correct formulation. However, no Bi {110} reflections are seen parallel to the Al {200} reflections in Fig. 25.

The uncertainty of the determination originates partly from the uncertainty in the measured angle in the SAD image, which is affected by aberrations as mentioned above and could be slightly misaligned too, and partly from the lack of symmetry of the rhombohedral lattice. A more detailed discussion of the calculations leading to Eqs. 23 and 24 is found in App. A.

Other, more precise relations between the inclusion and host lattices are:

$$\{110\}_{Bi} \parallel \{02\bar{2}\}_{Al}$$

as seen in Fig. 25 and in Fig. 30b, which shows sample TEM-4 in the <112> orientation, and

$$\{110\}_{Bi} \parallel \{111\}_{Al}$$

as found in Fig. 22c, Fig. 30b and by x-ray diffraction. As $\angle([111]_{Al}, [02\bar{2}]_{Al}) = 90°$ and the angle between the $(110)_{Bi}$ and the $(101)_{Bi}$ (or $(011)_{Bi}$) reflections is 92.36°, this may be the same orientational relationship. If so, calculations similar to the ones in App. A, but on the basis of the reflections seen in Fig. 30b, give the approximate result that $\{1, 12, 12\}_{Bi} \parallel \{112\}_{Al}$, or, arguing as above, $\{011\}_{Bi} \parallel \{112\}_{Al}$. The latter has been observed, *e.g.* in Fig. 29b.

Figure 33b shows a SAD image of sample TEM-4 in the $<100>_{Al}$ orientation, as in Fig. 25. The predominant inclusion orientation is $\{110\}_{Bi} \parallel \{022\}_{Al}$ as in Fig. 25, but in Fig. 33b, $\{110\}_{Bi}$ reflections are seen at an angle, which matches the angle of 92.36° between the $(110)_{Bi}$ and the $(101)_{Bi}$ (or $(011)_{Bi}$) reflections. If these reflections originate from the same inclusions, calculations like the ones performed in App. A leads to the result already given in Eq. 23; however, the relationship described in Eq. 24 is not seen here.

The bottom line must be that Bi lattice matches the Al lattice quite poorly, leading to the existence of different orientational relationships, each of which has several possible choices of orientation, due to the symmetries of the host and inclusion lattices. However, in all TEM and x-ray samples, the $\{110\}_{Bi}$ reflections have been found along each equivalent $<111>_{Al}$ direction. This means that the close-packed {111} facets of the aluminium voids are parallel to the close-packed {110} ones of the bismuth inclusions. A relationship where close-packed planes of one structure is parallel to those of another has been found in other systems, *e.g.* bcc thallium inclusions in aluminium[59], which have their close-packed {110} planes parallel to the close-packed {111} planes of fcc aluminium (following the Kurdjumov-Sachs relationship), as mentioned in section 2.1. The diffraction from aluminium {111} facets is seen clearly as streaks along the aluminium <111> direction in Fig. 31c, where the inclusions are liquid. The inclusions show sharp {110} facets, but are otherwise rounded.

A drawing of the rhombohedral structure of Bi is seen if Fig. 26. The (110) face is in the plane of the paper and the [$\bar{1}$11] direction is vertical. The structure in the drawing is bounded by {110} facets. Seen from this angle, the structure looks like a distorted simple cubic structure.

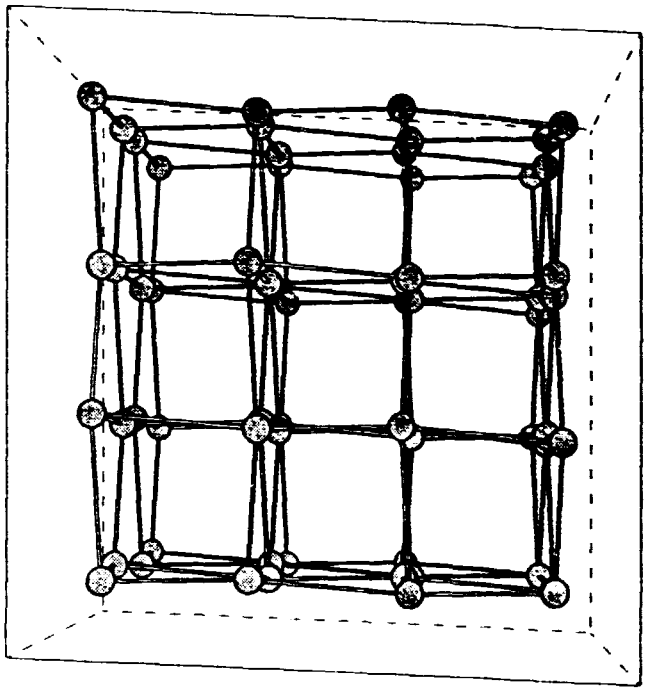

*Figure 26. The rhombohedral structure of Bi. The (110) face is in the plane of the paper and [$\bar{1}$11] direction is vertical.*

## 4.4 Heating and cooling in the electron microscope

Heating sequences have been performed on two transmission electron microscope samples, TEM-2 and TEM-4. The heating sequence was performed studying a grain in the Al <110> orientation in sample TEM-2, and one close to the Al <112> orientation in sample TEM-4. The sample TEM-2 was implanted at room temperature and annealed shortly at 595 K immediately prior to the heating sequence, whereas sample TEM-4 was implanted at an elevated temperature (523 K) and the heating sequence was performed on the as-implanted sample. Figures 27–28 show the sample TEM-2 in the <110> orientation at room temperature before and after annealing and Fig. 29 shows it after the heating sequence at 386 K. Figs. 30 and 33 show the sample TEM-4 at room temperature close to the <112> orientation prior to the heating sequence and in the <100> orientation after this sequence, shown in Fig. 31. The different thermal histories of the two samples are expected to affect the results of the heating sequences. One effect is that the aluminium background of a sample implanted at elevated temperature shows less radiation damage than samples implanted at room temperature (compare Fig. 28 with Fig. 30). The inclusions in the sample TEM-2 implanted at room tempera-

ture grow considerably during annealing, and the alignment of the inclusions to the host lattice is improved (compare Fig. 27 with Fig. 28; notice the different magnifications of the bright-field images).

Comparing Fig. 31a with 31g it is remarkable how little the inclusions have

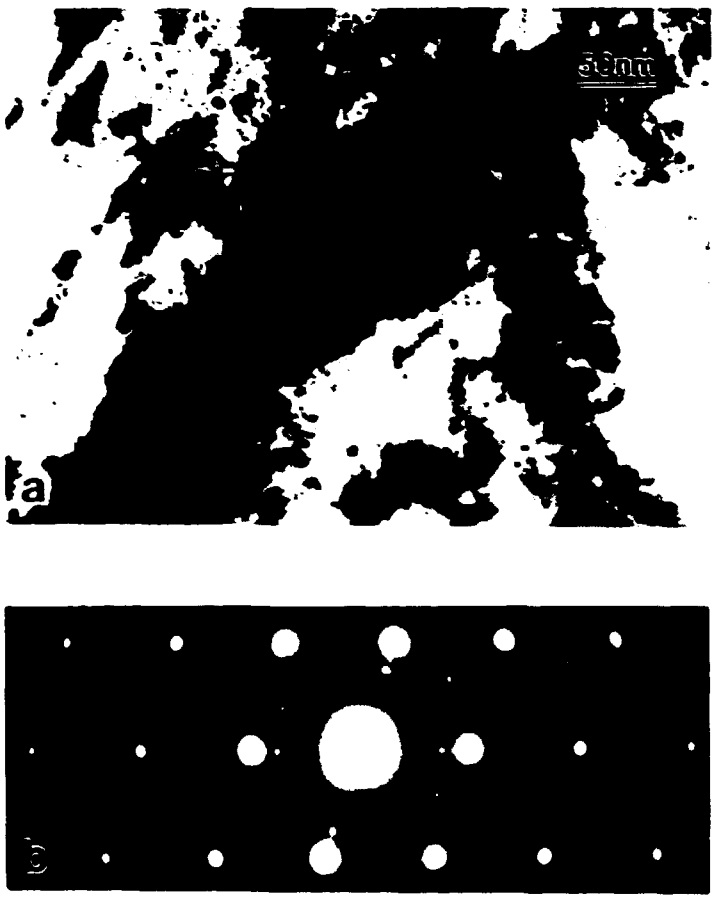


*Figure 27. a) Bright-field image of sample TEM-2 in the <110> orientation at room temperature before annealing. 230 000 times magnified. b) Corresponding selected area diffraction image.*

moved during the heating sequence. This is ascribed to the elevated temperature, at which the sample TEM-4 was implanted, simultaneously annealing the sample and thereby reducing the radiation damage on the aluminium matrix and producing larger inclusions. Both of these effects limit the mobility of the inclusions during the subsequent heating. The temperature during heating did not exceed the implantation temperature. More changes were seen in sample TEM-2, both during the annealing and during heating to a temperature higher than the annealing one (compare Fig. 28 with 29).

In Fig. 31 the same area of the sample TEM-4 is shown during the heating sequence. Between 440 and 476 K several inclusions have lost their moiré patterns, indicating melting. A few examples marked A are shown in Fig. 31a-b. The inclusions marked B seem to have shrunk a little from their non-facetted sides, which have become more curved, making their facetted sides shorter. This may be a sign of a roughening process, which has begun breaking down the {110} Bi facets.

At 516 K all inclusions have lost their moiré patterns and the diffraction image

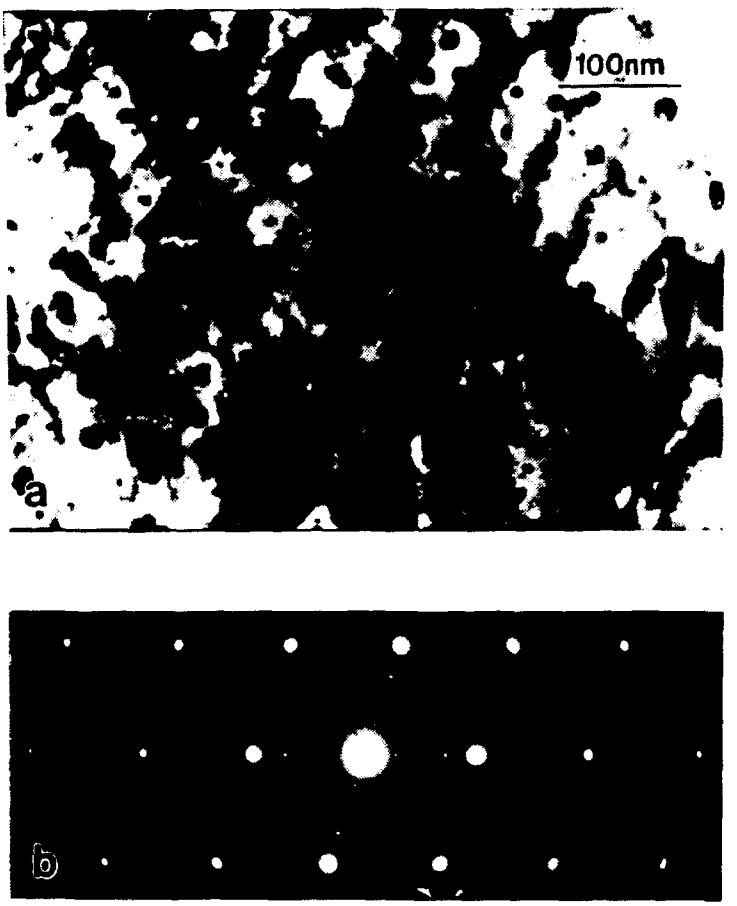


*Figure 28. a) Bright-field image of sample TEM-2 in the <110> orientation at room temperature before the heating sequence (but after annealing), 176 000 times magnified. b) Corresponding selected area diffraction image.*

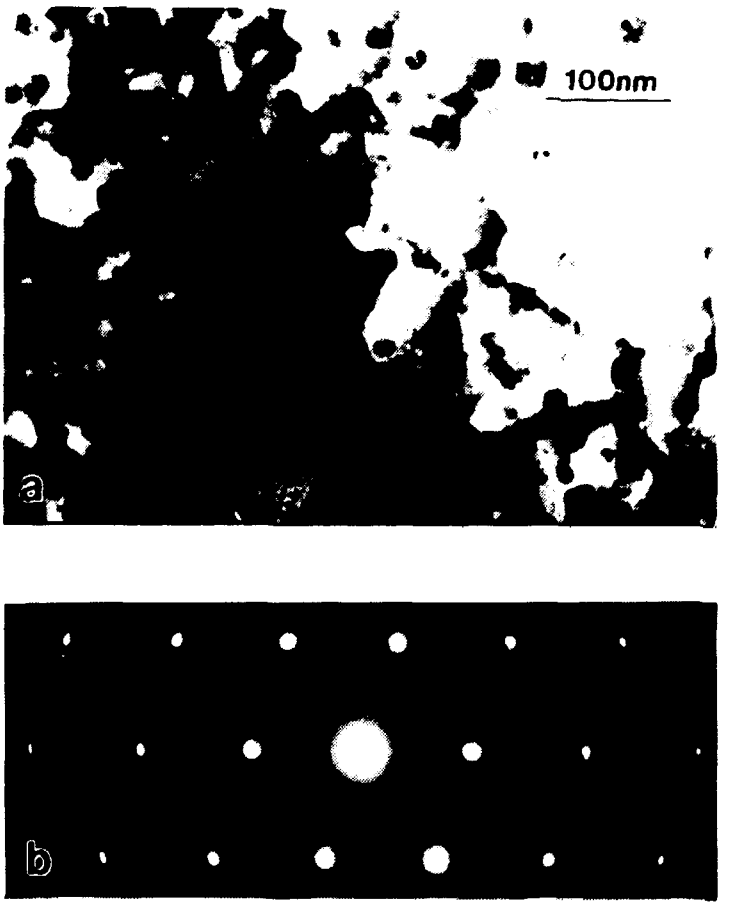


*Figure 29. a) Bright-field image of sample TEM-2 in the <110> orientation at 386 K after the heating sequence (highest temperature was 607 K), 176 000 times magnificd. b) Corresponding selected area diffraction image.*

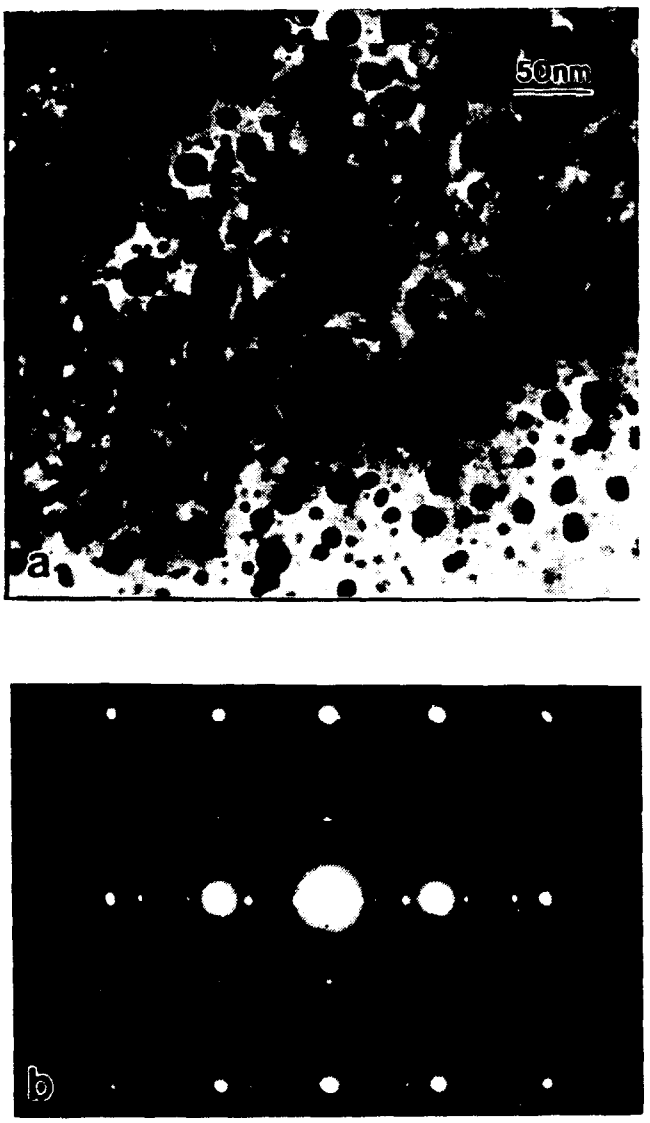


*Figure 30 a) Bright-field image of sample TEM-4 close to the <112> orientation at room temperature before heating. b) Corresponding selected area diffraction image.*

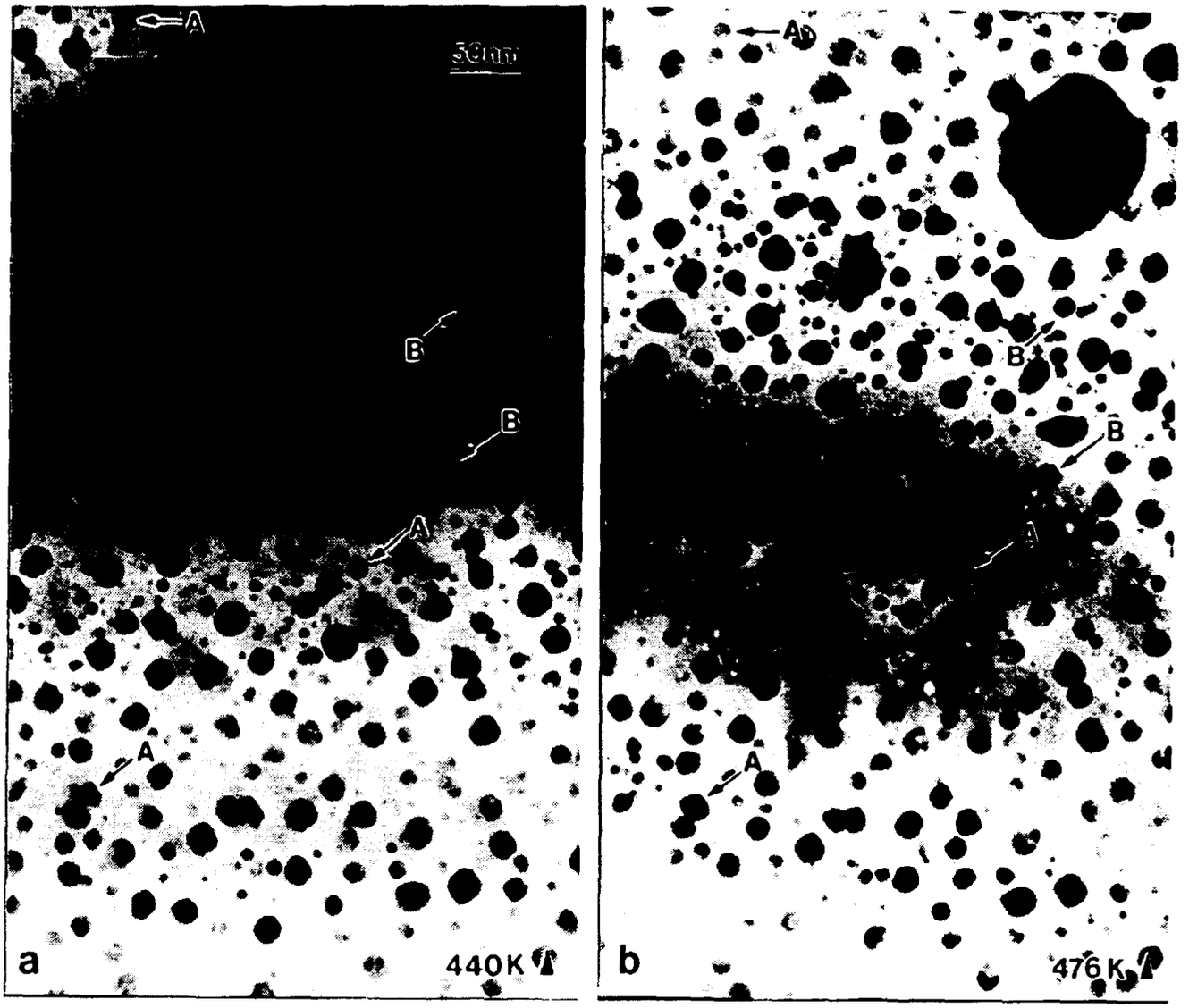
A
50nm
B
B
A
A
a
440K
A
B
B
A
A
b
476K

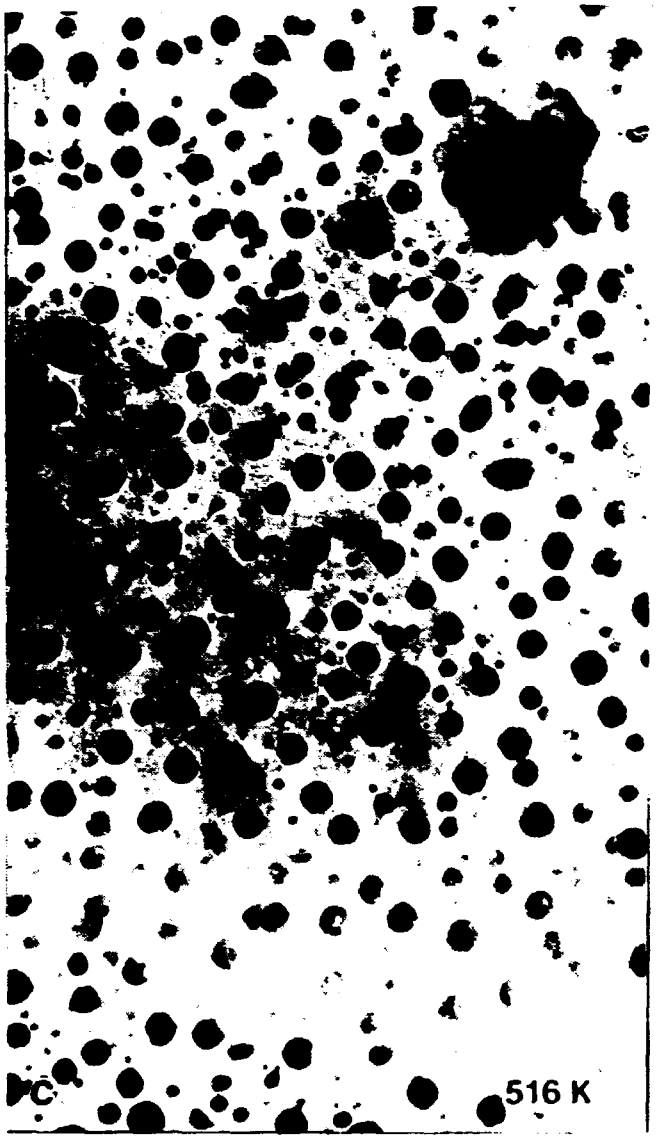
c
516 K


d
400 K

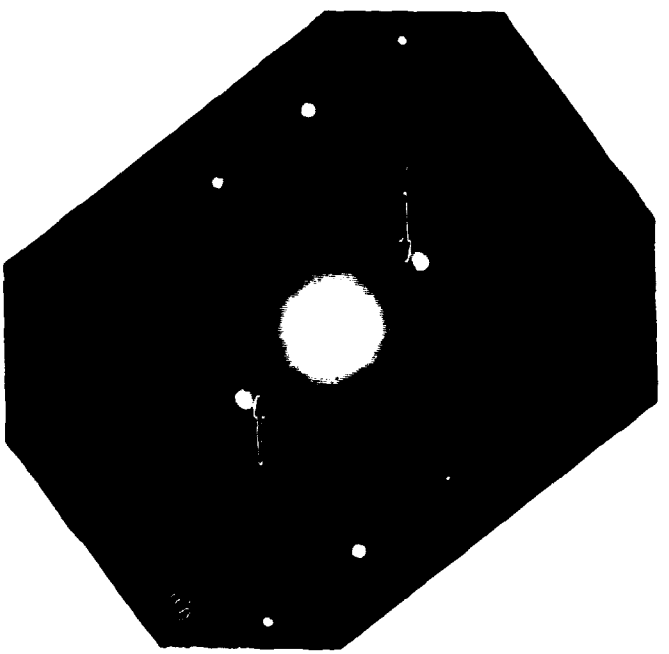

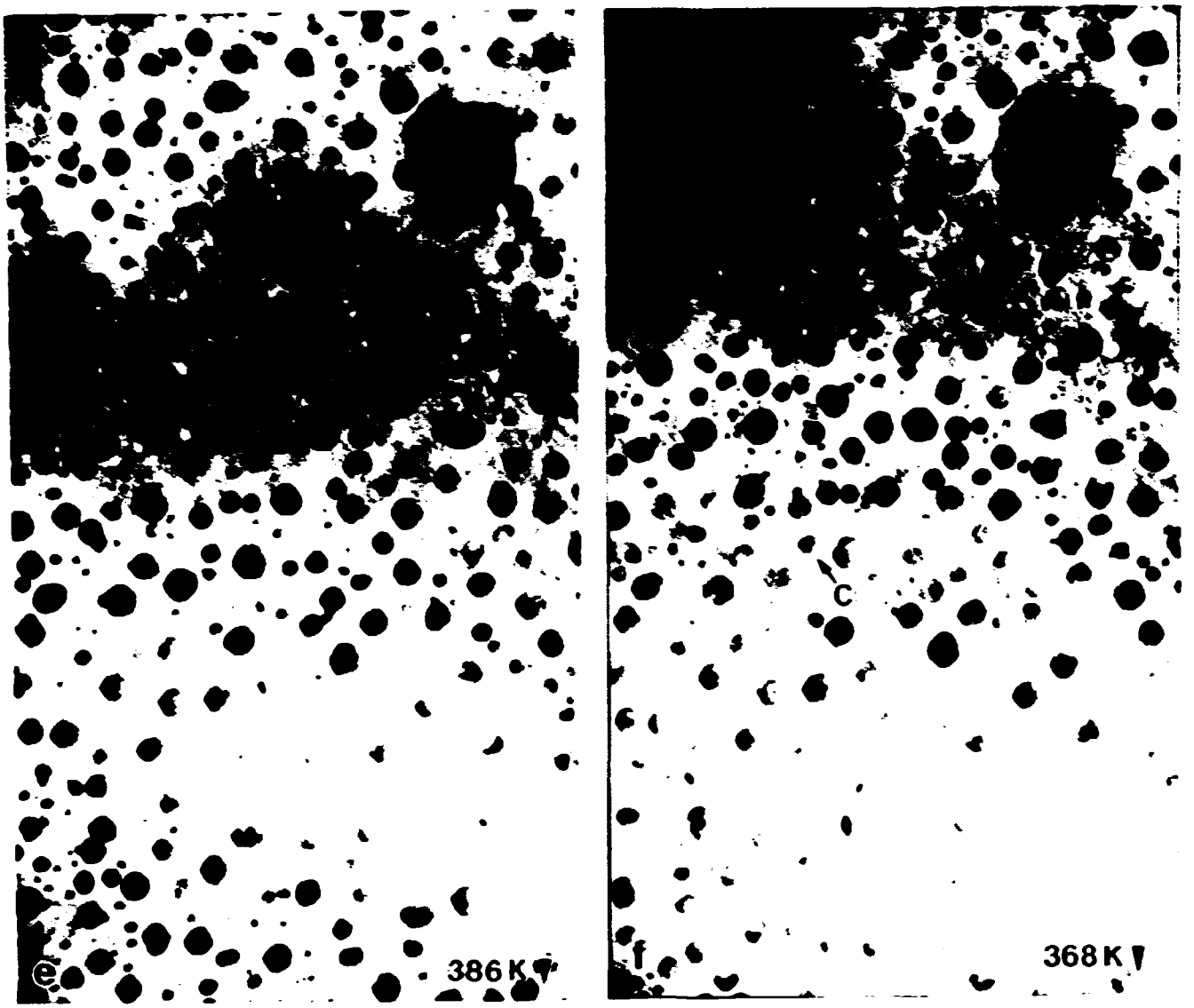
e
386 K
f
C
368 K

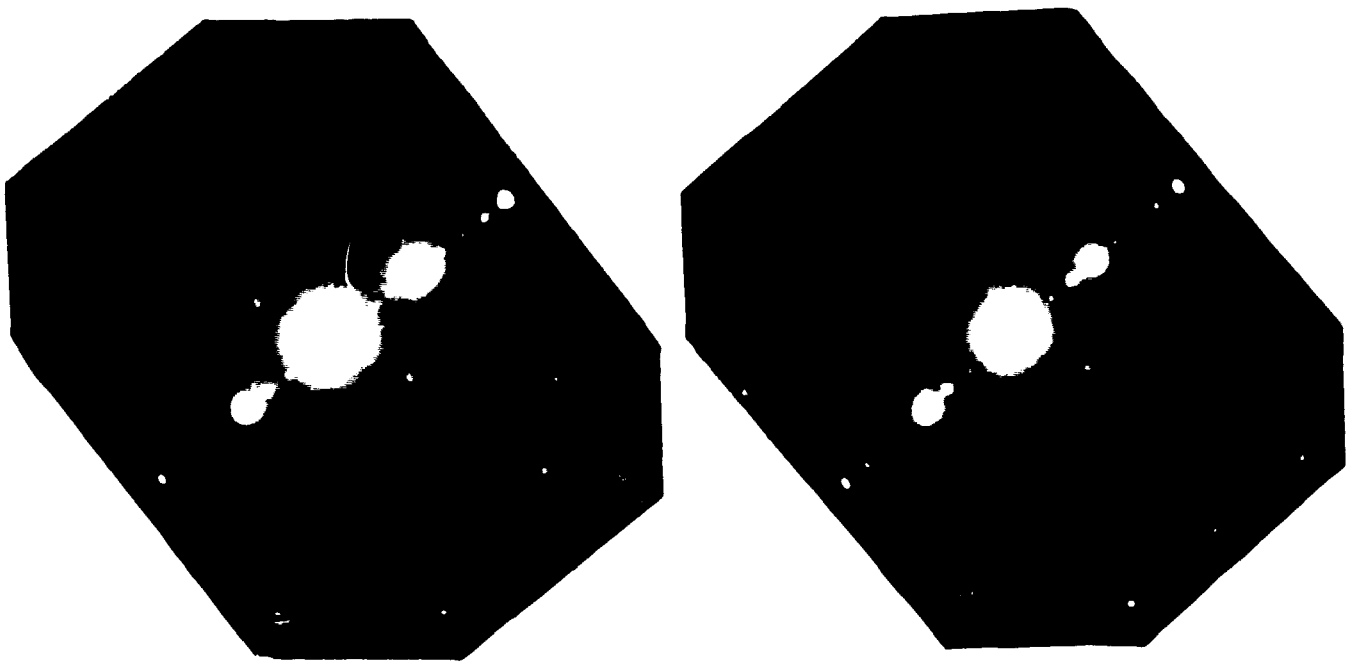

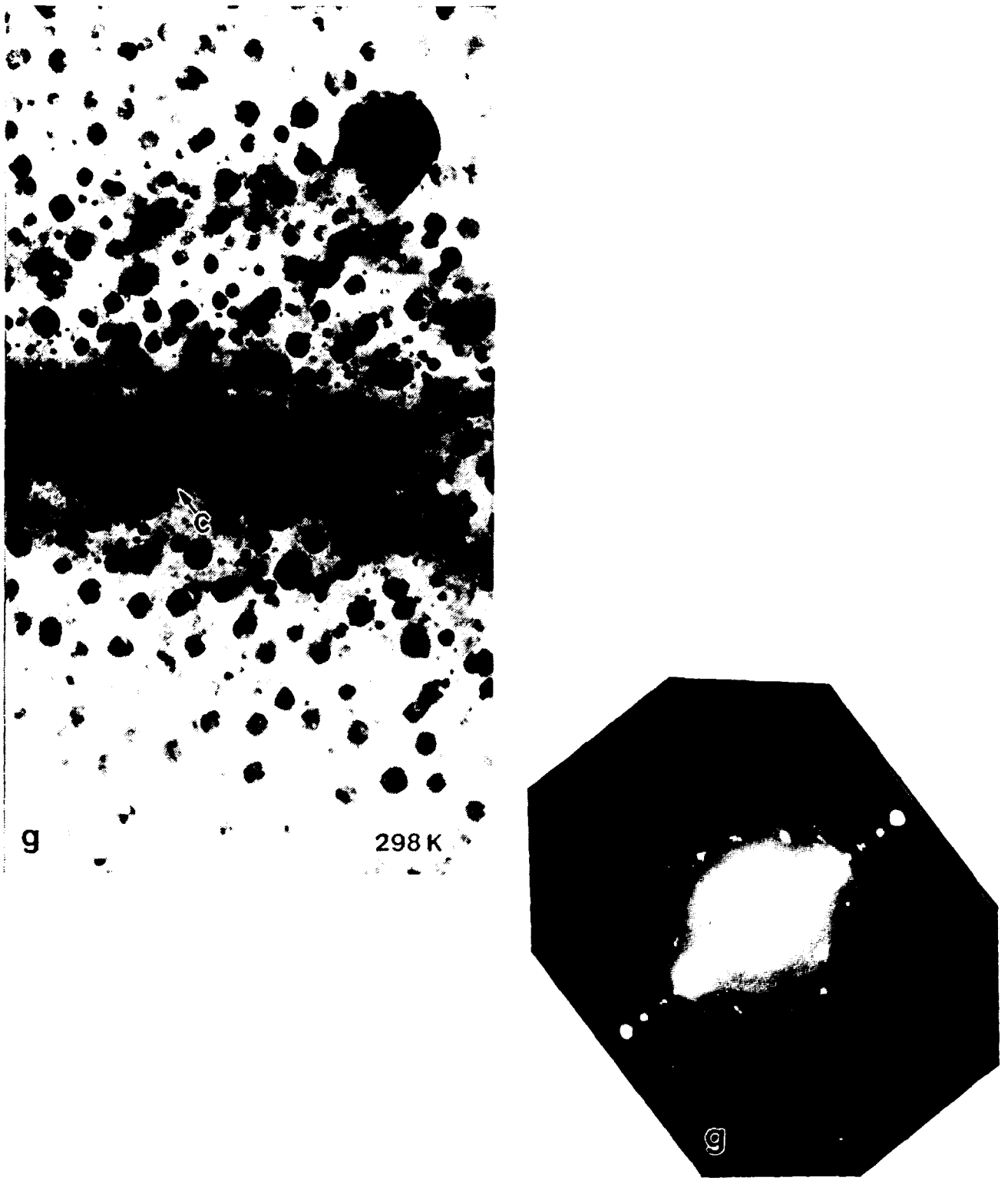


*Figure 31. Bright-field (and corresponding selected area diffraction) images of sample TEM-4 a little further away from the <112> orientation than in Fig. 30. The magnification of the bright-field images is 230 000. a) At 440 K. b) At 476 K. c) At the maximum temperature ≈ 516 K. d) At around 400 K. e) At 386 K. f) At 368 K. g) At room temperature.*

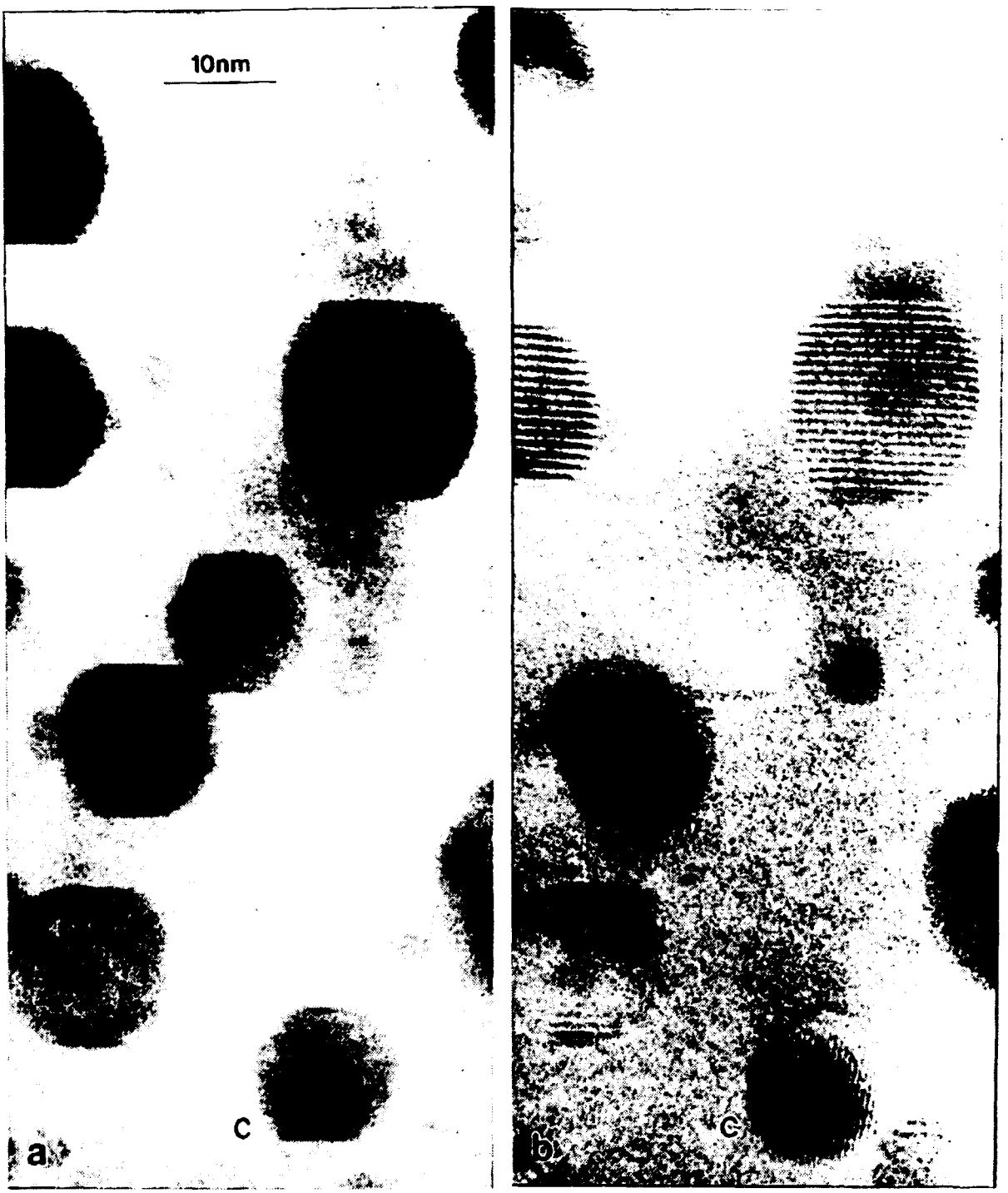


*Figure 32. Larger magnifications (1840 000 times) of the bright-field images in Fig. 31f and g. a) At 368 K (Fig. 31f). b) At room temperature (Fig. 31g).*

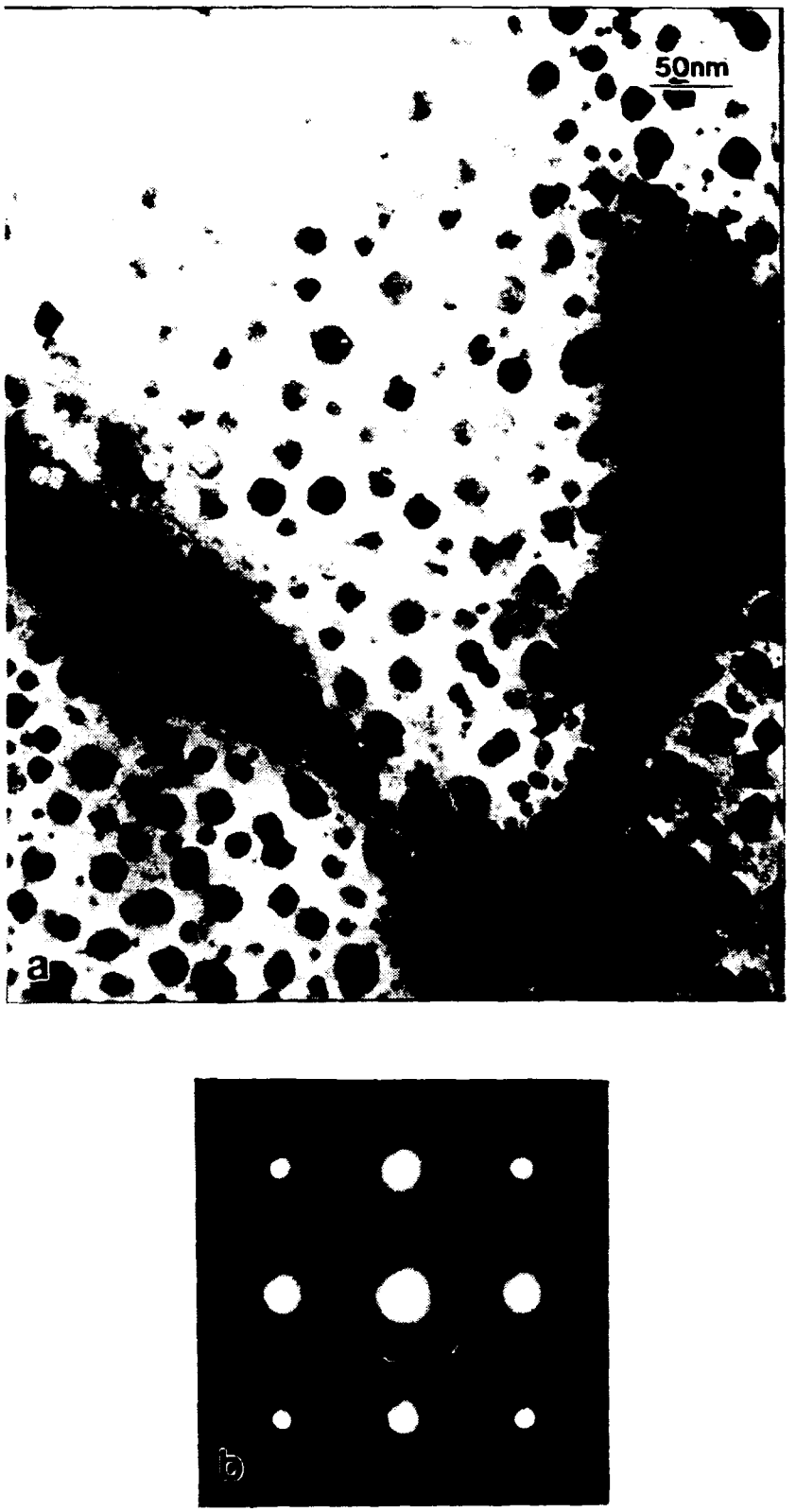


*Figure 33. a) Bright-field image of sample TEM-4 in the <100> orientation at room temperature after heating. b) Corresponding selected area diffraction image.*

in Fig. 31c shows a diffuse ring, which positively confirms that the inclusions are liquid. The streaks (marked with arrows) through the ring and the Al {111} reflections originate from the internal {111} facets of the Al cavities. Similar streaks were observed in the transmission electron microscope study of Xe in Ag by Templier *et al.*[61]. Several of the molten inclusions retain a flat side, where the {110} facets were, because of the confining Al cavity.

When the sample is cooled down 116 K to 400 K (Fig. 31d) the inclusions stay liquid. In Fig. 31e at 386 K, however, moiré patterns have reappeared in several inclusions and the SAD image show both a diffuse ring and Bi {110} spots, signifying that some inclusions have solidified, while others remain liquid. Because of under-shooting the temperature had been as low as 375 K, so the onset of solidification is between 400 and 375 K.

More inclusions solidify when cooling to 366 K with a minimum temperature 355 K (Fig. 31f). It is noted that even more solid inclusions are found at room temperature (Fig. 31g), indicating that the solidification process has not finished at 355 K. The small inclusion (marked C), which showed moiré fringes along the {110} Bi facet has changed the orientation and spacing of its moiré fringes at room temperature (see the magnifications in Fig. 32).

The diffraction image at room temperature (in Fig. 31g) shows (apart from the {110} bismuth reflections along the Al <111> directions) a large number of Bi reflections in different angles to the Al {111} reflections and with different lengths of the q-vector, which demonstrates that the inclusions have taken up several different orientations. As mentioned above, the diffraction pattern viewed in the Al [100] direction (Fig 33b) is different from the one observed for sample TEM-3 in the same orientation (see Fig. 25).

# 5 Rutherford backscattering and ion channeling experiments

The Rutherford backscattering and ion channeling experiments were performed at the isotope separator at the Orsted Laboratory of the University of Copenhagen. Introductions to the concepts of backscattering spectrometry have been given by Chu *et al.*[13] and Andersen[4]. A review of channeling is presented by Gemmell[20]. The following sections are based on the above-mentioned references. Ion channeling in a bismuth single crystal has previously been observed by Ellegaard *et al.*[15].

## 5.1 Rutherford backscattering

*Rutherford backscattering* takes its name from the well-known scattering cross section derived by Rutherford in 1911. The actual scattering cross section differs from the Rutherford cross section, because screening by electrons (at low energies, small scattering angles) and scattering by nuclear forces (at high energies, large scattering angles) give corrections to the cross section.

**The depth scale**

Consider an ion of mass $M_1$ and energy $E$ that collides with an atom of mass $M_2$ ($M_2 \gg M_1$) at a depth $x$ in a mono-isotopic target crystal as depicted in Fig. 34a. The energy of the incident particle after the collision will be $KE$, where $K < 1$ is the kinematic factor

$$K = \left( \frac{M_1 \cos\theta + \left(M_2^2 - M_1^2 \sin^2\theta\right)^{1/2}}{M_1 + M_2} \right)^2 \tag{25}$$

The scattering angle, $\theta$, is given by $\theta = 180° - \theta_1 - \theta_2$, where $\theta_1$ and $\theta_2$ are the angles between the surface normal and the incident and the scattered ion, respectively. The ion also loses energy when passing through the crystal before

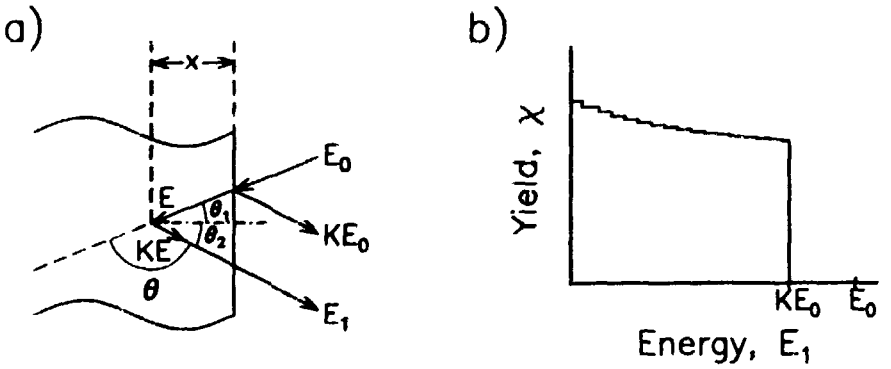


*Figure 34. a) A schematic backscattering spectrum. $E_1$ is the detected energy and $\theta$ is the scattering angle. b) Backscattering yield. $KE_0$ is the edge energy.*

and after the scattering event. If the energy of the ion is $E_0$ before entering the crystal, the maximum detected energy will be $KE_0$. The backscattering spectrum from a bulk sample will therefore be continuous up to the edge energy $KE_0$ (see

Fig. 34b). If the energy loss $dE/dx$ is assumed to be constant along the inward and outward paths, the energy difference $\Delta E$ between ions scattered at the surface and ions scattered at depth $x$ can be linearly related to the depth. In general, the exact relationship

between $\Delta E$ and $x$ is not linear. Several methods exist to obtain more accurate depth scales, employing analytical or numerical calculations[13]. At the Ørsted Laboratory the conversion of energy to depth scale is made by a computer calculation based on tabulated values of the energy loss $dE/dx$. As the energy loss is due to interactions with the electrons of the atoms in the crystal (and at low energies with the nuclei of the atoms), the measured energy loss does in fact not correspond to a depth, but to a certain amount of material (atoms per unit area) passed on the inward and outward paths. However, whenever the atomic density $n$ of the material is known, the number of atoms per unit area $N$ over the traversed distance $\Delta x$ can be related to the distance by $N = n \cdot \Delta x$.

The yield of backscattered ions in a particular energy range depends on the number of scattering events in the corresponding depth range and thus on the number of atoms in that depth, the width of the depth range, the number of incident ions, the scattering cross section, and on the solid angle and efficiency of the detector. When the crystal contains different elements (or isotopes), the backscattering yields from the different elements are added. As can be seen from Eq. 25, the position of the edge depends on the mass $M_2$ of the element. In the present case a 500 keV $^4$He beam impinges on a target containing $^{27}$Al and $^{209}$Bi, and the scattering angle is $\theta = 135°$. The kinematic factors are then $K_{Al} = 0.60$ and $K_{Bi} = 0.94$, giving the edge energies $K_{Al}E_0 = 300\,\text{keV}$ and $K_{Bi}E_0 = 470\,\text{keV}$, which are easily separated. Furthermore, the limited range of the implanted Bi means that the Bi signal does not extend in a large depth, and that the Bi and Al signals practically do not overlap.

## 5.2 Ion channeling

In this chapter the crystal has so far been assumed to be amorphous. Channeling measurements probes the crystal structure. Consider a beam of ions (or atoms) impinging on a crystal. If the direction is close to a major crystal axis, the ions may be steered between the rows of atoms (see Fig. 35a) by a series of small-angle collisions with the atoms of the crystal. As the angle $\psi$ between the incident

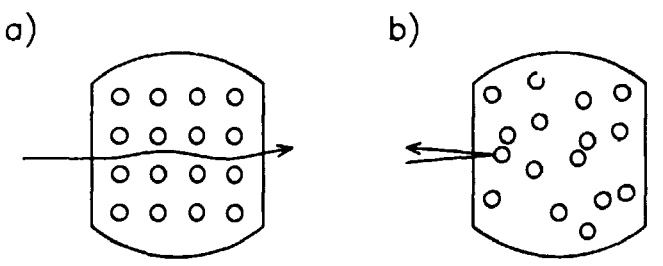


*Figure 35. Schematic illustration of the channeling effect. a) Solid crystal. The frequency of the oscillations of the incident ion is highly exaggerated b) Liquid (or amorphous crystal).*

beam and crystal axis is changed, the backscattering yield, which is normalized to $\chi = 1$ at random incidence, changes dramatically (see Fig. 36). When $\psi = 0$,

the channeled fraction reaches a maximum, and therefore the backscattering yield takes a (local) minimum value $\chi_{min}$. So $1-\chi_{min}$ gives a measure of the channeling ability of the crystal along the given axis. The backscattering yield from a surface

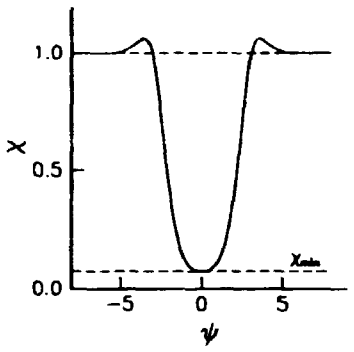


*Figure 36. The angular dependence of the backscattering yield.*

with a given density of atoms does not depend on the structure below the surface. Hence, when the crystal is aligned to a channeling direction, there will be a peak at backscattering energies corresponding to the surface. The surface peak stem from the outermost (1–5) layers of a single crystal [5]. Monte-Carlo simulations for 500 keV $He^+$ ions in lead have given the results that the surface peak dominates the channeling yield in a single crystal for depths up to 15 nm and that good channeling in lead inclusions in aluminium requires inclusions larger than 2 nm[8]. Just below the surface, the backscattered ions have lost a minimum of energy by small-angle scattering processes in the crystal, and therefore we use the level here to measure the channeling effect. Channeling can occur also along a crystal plane (planar channeling) instead of a crystal axis (axial channeling). When the crystal melts, the crystal structure breaks down and the channeling effect disappears (see Figs. 35b and 39b).

If the targets are thin, the channeling effect can be measured in transmission instead of backscattering. As we have not used this technique, I will not discuss it.

## 5.3 Experiment

The backscattering experiment was performed at the accelerator where the sample was implanted (see Fig. 37) without breaking the vacuum; the beam was simply changed from $Bi^+$ ions to 500 keV $He^{2+}$ ions. In the target chamber of the accelerator, the crystal was mounted on a goniometer and annealed *in situ* by means of a wire-wound heater (see Fig. 38). The temperature was measured by a chromel-alumel thermocouple, which was mounted between the sample and the base plate of the holder. The channeling measurement was performed not earlier than five minutes after the temperature selected for a measurement was reached. The temperature was held constant within 0.5 K during measurements, and the temperature difference between the sample and the thermocouple was less than 5 K.

The backscattering yield was recorded in a multichannel analyzer. At each temperature both channeling and random orientation spectra were recorded. Random orientation was achieved by tilting the crystal <110> axis 10° away from the in-

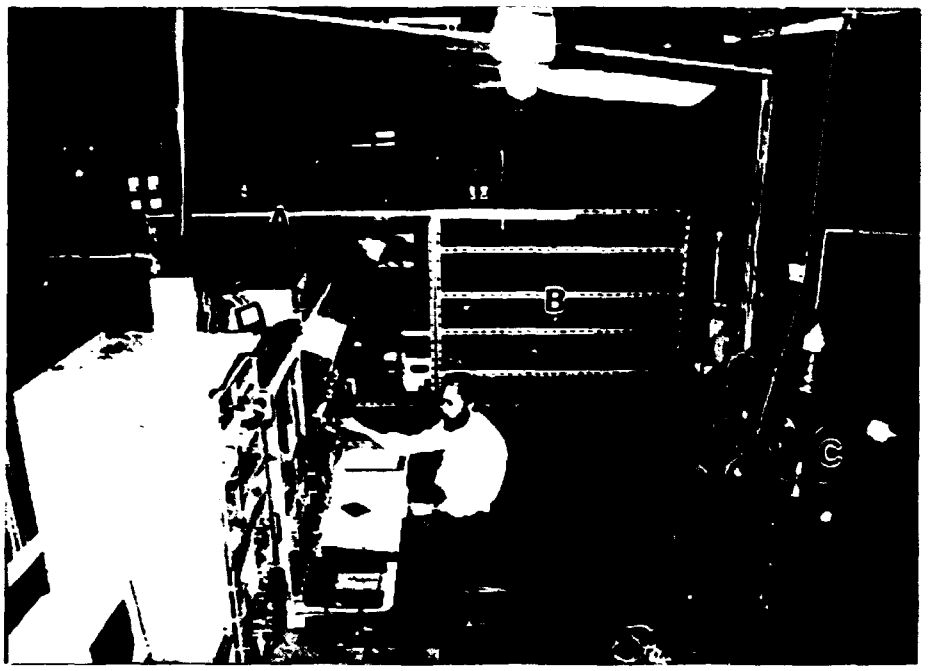


*Figure 37. The Accelerator. A Ion source, B magnet for mass separation, C target chamber.*

cident beam direction, and rotating around the <110> axis while measuring, to average out any axial or planar channeling.

## 5.4 Data analysis and comparison to the x-ray data

Figure 39 shows Rutherford backscattering yields from the sample Ch-1 in random orientation and aligned to the channeling Al <110> direction at room temperature before the heating cycle, at the highest temperature (550 K), and at 310 K during cooling after the heating cycle.

The depth profile of the implanted bismuth, extracted from the random spectrum recorded before the heating cycle (Fig. 39a), is shown in Fig. 40a. The profile does not exhibit significant changes during the temperature cycle. The full curve in Fig. 40b is the calculated TRIM (TRansport of Ions in Matter) profile (version 90)[77] for 150 keV Bi ions in Al for comparison. The dotted curve is the calculated TRIM vacancy profile. The simulated values for the mean projected range $R_p^{th}$ (the mean depth of the implanted particles) and the range straggling $\Delta R_p^{th}$ (the standard deviation of the range distribution) are 51.7 and 11.4 nm, respectively. Experimental investigations indicate that the TRIM calculations reproduce the average depth well in general, but underestimate the range straggling and the width and position of the vacancy production distribution[3]. The measured depth profile shows a pronounced minimum at the depth where the TRIM simulation predicts the maximum concentration. This is interpreted as an effect of the elevated temperature during implantation resulting in radiation-enhanced diffusion and segregation, as similar samples implanted at room temperature do not exhibit such a minimum. Radiation damage during the implantation induces a high densi-

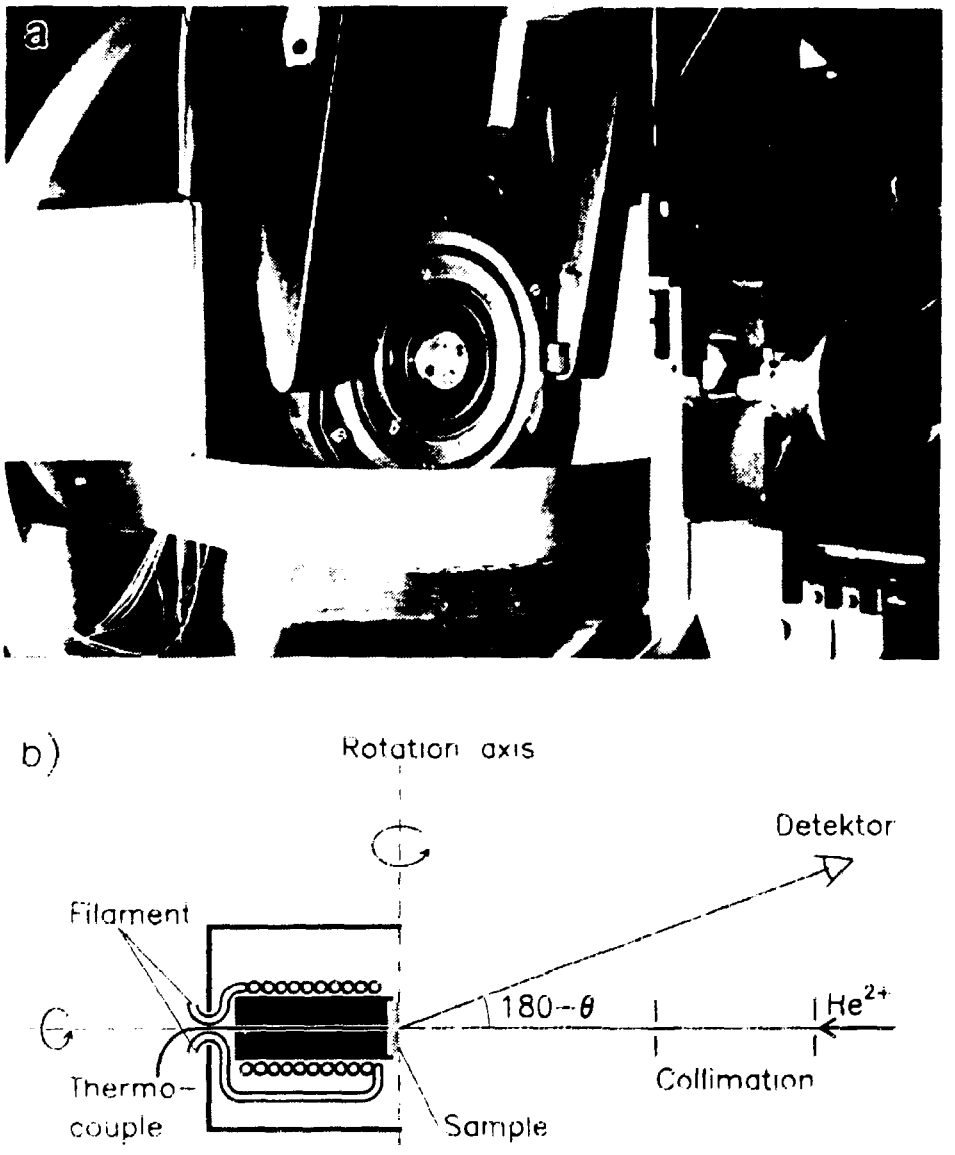


*Figure 18. The experimental setup for channeling experiments. a) Photo of the sample holder in the target chamber. b) Sketch of setup in the target chamber. Only two of the three perpendicular rotation axes are shown.*

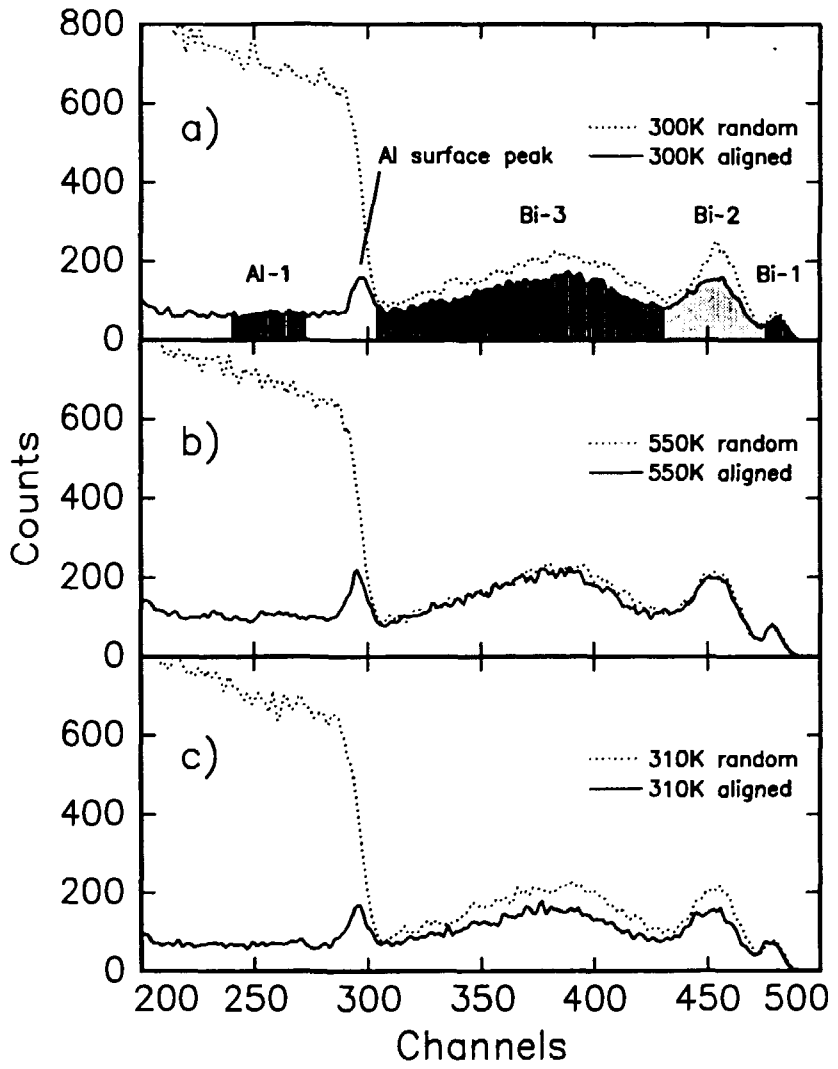


*Figure 39. Rutherford backscattering yield from the sample Ch-1 in random orientation (dotted curves) and aligned to the Al <110> channeling orientation (full curves). a) As implanted at room temperature. The shaded areas are explained in the text. b) At 550 K where no channeling is seen in Bi. c) At 310 K during cooling after the heating sequence.*

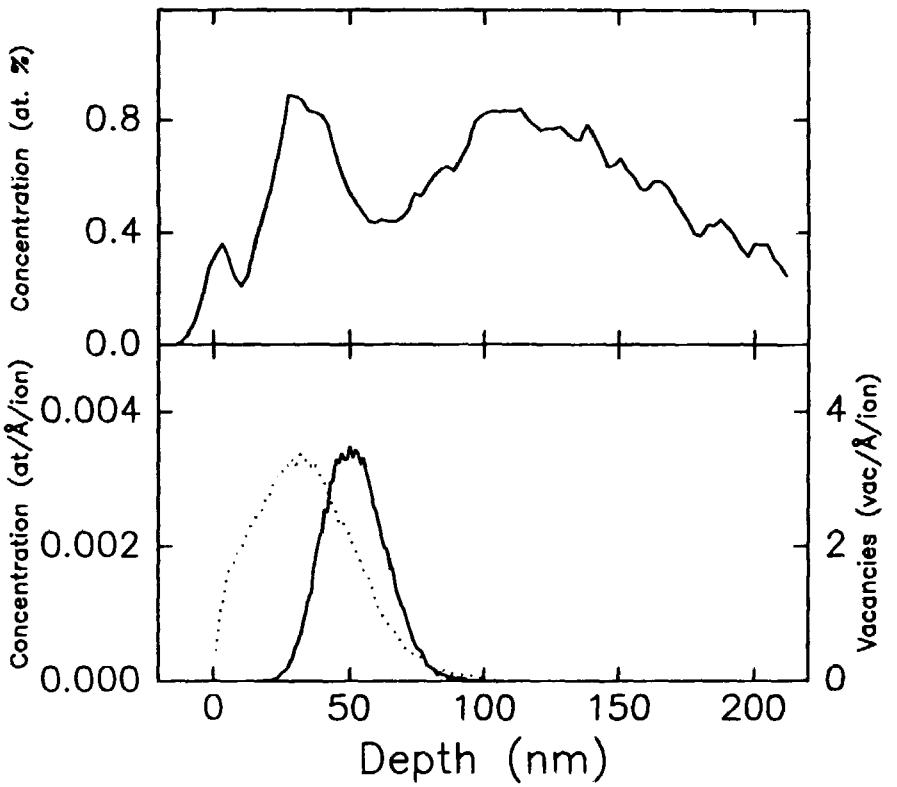


*Figure 40. a) Depth profile calculated from the random spectrum at room temperature in Fig. 39a b) TRIM depth profiles. The full curve drawn against the left scale is the distribution of the implanted Bi ions and the dotted curve plotted against the right scale is the vacancy production.*

ty of vacancies (Fig. 40b). At the elevated temperature the implantation profile will broaden due to diffusion in processes where the oversized bismuth atoms combine with vacancies. Redistribution of implants will hence depend on as well implant as vacancy distribution gradients and their relative position. The latter may not be judged from Fig. 40b due to the uncertainty in the distribution widths.

The as-implanted sample (Fig. 39a) shows significant channeling (the backscattering yield is lower in the aligned spectrum) in the bismuth inclusions when the beam is incident along the <110> direction of the matrix. The absence of channeling at higher temperatures ($T$ = 550 K, Fig. 39b) is ascribed to melting of the inclusions, while the reappearance of channeling upon cooling (Fig. 39c) is ascribed to resolidification in epitaxial alignment. To analyse the channeling effect, the bismuth spectra were divided into three intervals (marked in Fig. 39a) Bi-1, from bismuth atoms at the surface (0-10 nm); Bi-2, from bismuth atoms in the depth range 10 nm to 65 nm below the surface (see Fig. 40a); and Bi-3 from bismuth atoms in the depth range 65 to 200 nm. The yields from these three intervals were compared with that from an aluminium window Al-1 just behind the surface peak. To get a quantitative measure of the channeling, the fraction, $\chi_{min}$, between the areas under the curve from the different windows measured in the <110> orientation and the corresponding areas measured in random orientation is calculated at each temperature. The "relative" channeling is calculated as $(1 - \chi_{min}(Bi))/(1 - \chi_{min}(Al))$. This quantity is normally used to estimate a

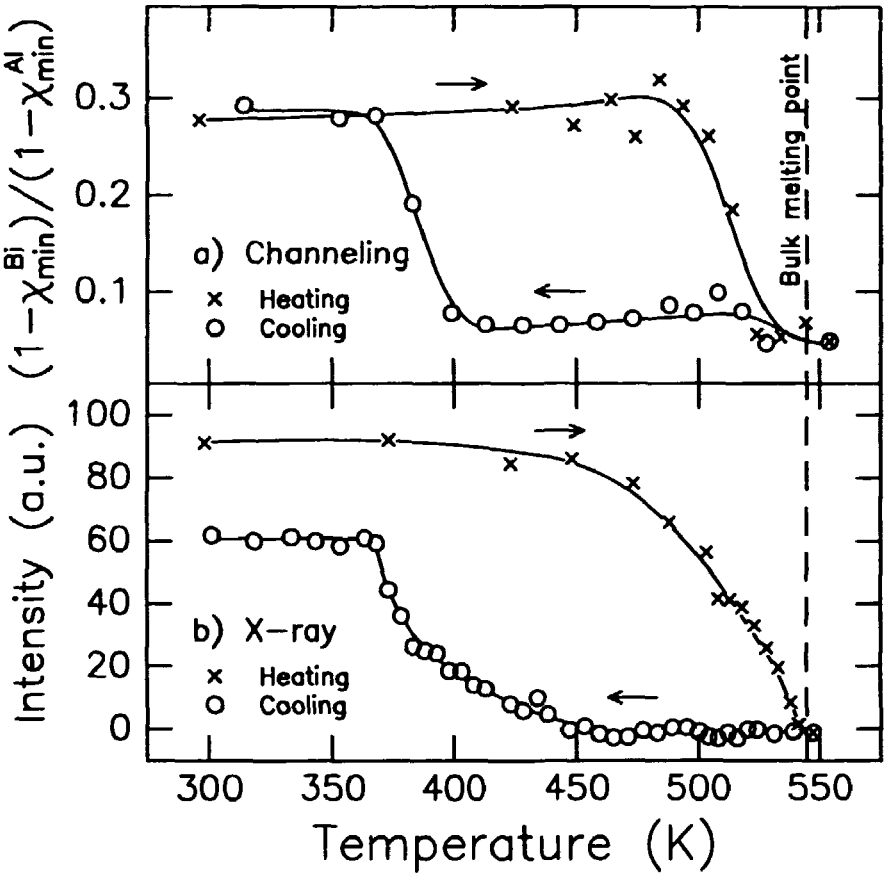


*Figure 41. a) Relative channeling rates during the temperature cycle. b) The x-ray data repeated from 14a. The curves are guides for the eye.*

substitutional fraction on sites along channel rows, but in this case it should be regarded only as a way to normalize the channeling ability of the inclusions to the channeling ability of the matrix.

No channeling is found in the small Bi surface peak (interval Bi-1). The "relative" channeling signals from the higher-lying (Bi-2) and the deeper-lying (Bi-3) inclusions show the same temperature dependence. Figure 41a shows the sum of "relative" channeling from the two intervals Bi-2 and Bi-3 over the whole temperature cycle. The wiggles between 425 K and 500 K in the heating curve were caused by electronic noise and should be disregarded. The x-ray data have been repeated for comparison (Fig. 41b).

The similarities between the channeling data in Fig. 41a and the x-ray data in Fig. 41b are striking, and in particular the data obtained by two different experimental methods agree on the two points: that superheating is not observed, and that a large supercooling is seen. The melting starts well below the bulk melting point, and the liquid inclusions can be supercooled to temperatures far below the bulk melting point, giving a width of the melting/solidification hysteresis of around 100 to 150 K. It should be stressed that the measured quantities related to the liquid/solid phase transformation in the x-ray and the channeling experiment are very different. The channeling signal is dominated by the larger inclusions[8] and the melting and solidification of the small inclusions are therefore not observed, whereas the x-ray measurements detect a wider part of the

size distribution. The depth sensitivity of the two methods is quite different too; the penetration depth for x-rays in Al extends well beyond the distribution of Bi implants, while the channeling measurements probe a layer of a thickness a few hundred nanometers. In addition, the thermal history and the orientation of the two samples are different.

For the x-ray data, the onset of the melting is around 480 K, and the diffraction from the inclusions has disappeared at 541 K, that is 3 K below the bulk melting point. Similarly, solidification takes place over a temperature range of 70 K, from 435 to 365 K. The channeling signal is constant up to 500 K, where it decreases abruptly within a narrow temperature interval of 25 K, disappearing 20 K below the bulk melting point. Solidification as observed by channeling sets in at 400 K and, as for melting, the width of the transition, around 30 K, is considerably smaller than it was in the x-ray data. On the assumption that the melting temperature of a small particle depends mainly on its size, the narrower width of the transition seen in the channeling experiment may be a result of differences in the two size distributions, or, as mentioned above, of the difference in sensitivity between the two methods.

# 6 Grazing-incidence small-angle x-ray scattering

The grazing-incidence small-angle scattering experiments were performed at the 5kW Rigaku rotating anode in the Laboratory of Physical Metallurgy at the University of Poitiers, France.

The chapter is organized as follows: After a short introduction to small-angle x-ray scattering under grazing incidence, the experimental setup and the samples are presented. Thereafter the data analysis is described and the results are discussed.

## 6.1 Introduction to grazing-incidence small-angle scattering

Small-angle x-ray scattering (SAXS) contains information on the shape, sizes, volume fraction and surface of the scattering particles. This information is also available by transmission electron microscopy, but where SAXS gives average values of a large number of particles, the number of particles studied in transmission electron microscopy is much smaller and, in addition, the electron beam may damage or change the sample.

Until recently, small-angle x-ray scattering was done usually in transmission geometry. This is however not very adequate for studying the surface layers of a sample, as the signal from the layers of interest are likely to be hidden by the scattering from the rest of the sample. Levine *et al.*[37] pioneered the use of a grazing incidence geometry of small-angle x-ray scattering (Grazing-Incidence Small-Angle X-ray Scattering or GISAXS) analogous to grazing-incidence x-ray diffraction and reflectometry, which have become valuable tools for studying surfaces (see the review by Feidenhans'l[16]). In contrast to SAXS in transmission geometry and transmission electron microscopy the grazing-incidence geometry imposes no restrictions on the sample thickness.

The refractive index $n$ of a material depends on the wavelength of the electromagnetic radiation, and for x-rays the refractive index is smaller than unity, the difference being of the order of $10^{-5}$. Neglecting absorption, the refractive index is given by[16]

$$n = 1 - 2.701 \cdot 10^{-6} \frac{\sum Z_j}{\sum A_j} \rho \lambda^2, \tag{26}$$

where the atomic charges $Z_j$ and masses $A_j$ are summed over the unit cell, $\rho$ is the mass density in g/cm$^3$, and $\lambda$ wavelength of the electromagnetic radiation. The critical angle ($\alpha_c$) is defined by $\cos\alpha_c = n$. For Cu $K_\alpha$ radiation $\lambda = 1.54178$ Å[68], and for aluminium $Z = 13$, $A = 26.98$, and $\rho = 2.699$ g/cm$^3$[69], giving a critical angle of $\alpha_c = 0.23°$. The angles $\alpha_i$ and $\alpha_n$ between the surface and the incident and refracted x-rays, respectively, are related through $n\cos\alpha_n = \cos\alpha_i$ (Snell's law). For small angles this can be written as $\alpha_n^2 = \alpha_i^2 - \alpha_c^2$. When the angle of incidence is smaller than the critical angle, $\alpha_n$ becomes imaginary, the amplitude of the refracted wave will be exponentially damped as a function of depth and this evanescent wave will travel parallel to the surface.

Levine *et al.*[37] studied the formation of small gold islands in the initial stages of thin film growth on a glass substrate. The angle of incidence ($\alpha_i$) was close (or equal) to the critical scattering angle ($\alpha_c$) of the substrate, and the gold islands produced a small-angle scattering signal around the refracted beam travelling close to the surface. The small-angle scattering from the islands was measured with the scattering vector $\mathbf{q}$ parallel to the surface.

In a comparative SAXS and GISAXS study of Guinier-Preston zones in Al-Ag alloys, Naudon *et al.*[44] demonstrated that GISAXS with $\alpha_i > \alpha_c$ and the scattering vector **q** perpendicular to the surface of the sample gave reliable values of the size parameters and the volume fraction of the scattering Guinier-Preston zones.

The rest of this chapter describes an investigation of the feasibility of grazing-incidence small-angle scattering experiments for the purpose of studying krypton inclusions in aluminium.

### The scattering geometry

The scattering geometry and setup used in the present experiment was the one previously used (and described) by Naudon *et al.*[44]. A short description will be given here.

Figure 42 shows the geometry of the small-angle scattering process. S is the plane of the sample surface, $\alpha_i$ is the angle of incidence, $\mathbf{k}_i$, $\mathbf{k}_r$ and $\mathbf{k}_n$ are the wavevectors of the incident, reflected and refracted x-rays, respectively. **q** is the scattering vector and D the plane of the position-sensitive detector. When $\alpha_i$ is

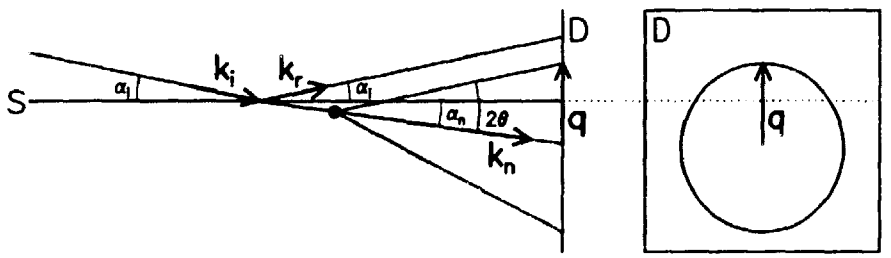


*Figure 42. Schematic drawing of the grazing-incidence small-angle scattering geometry with* **q** *perpendicular to the surface and* $\alpha_i$ *slightly larger than* $\alpha_c$. *Refraction is neglected at the exit from the sample.*

slightly larger than $\alpha_c$ the intensity of the reflected beam is weaker than that of the refracted beam. The refracted beam travelling just below the surface encounters the inclusions, which give rise to a small-angle scattering signal in the directions of a cone of half-angle $2\theta$ around the refracted beam. Only the part of this scattering, which lies in the plane of the detector above the intersection with the plane of the surface can be detected. When the scattering vector is perpendicular to the surface of the sample, the structure of the sample is studied in the depth direction in contrast to the geometry employed by Levine *et al.*[37].

Scattering caused by surface roughness can give rise to a signal in the same range of $2\theta$-angles as the small-angle scattering. It is therefore important to have samples of low surface roughness. If the quality of the surface of the sample is good (low roughness), total reflection will occur when $\alpha_i = \alpha_c$, and for angles ($\alpha_i$) slightly larger than the critical angle, a residual reflection is seen at the scattering angle $\alpha_i + \alpha_n \approx 2\alpha_i$ (as $n \approx 1$).

### Experimental setup

A sketch of the experimental setup is seen in Fig. 43. A is the rotating anode equipped with a copper target. The linear focus size is 3 x 0.3mm. The filters (F) are used to attenuate the beam during alignment. The monochromator M is an asymmetric bent germanium (111) crystal with an angle of 9.1° between

the polished surface and the (111) planes. The monochromator has a large focal distance (1000 mm) in order to produce a beam of small divergence and sufficient intensity, which is defined geometrically by the slits $S_1$ and $S_2$. The detector (D) is a one-dimensional position sensitive proportional counter filled with a mixture of Xe and $CH_4$. The spatial resolution of the detector is 150 $\mu$m. B is the beam-stop and C is the vacuum chamber. The chamber can be rotated around a vertical axis centered on the monochromator, and this is used to maximize the intensity of the direct beam before the sample S is inserted, and later to align the sample in the beam. The sample holder can be rotated around a vertical axis to obtain the desired angle of incidence. The slit $S_2$ determines the area of the sample, which is illuminated by the beam. The distance between the sample and the detector is 160 mm.

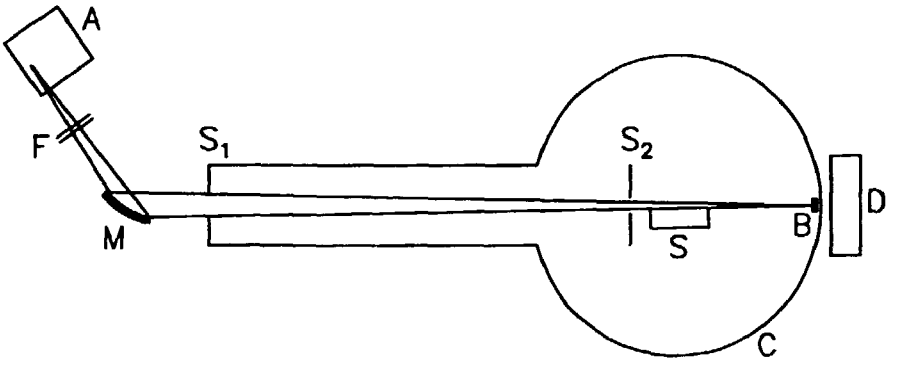


*Figure 43. A sketch of the experimental setup for grazing-incidence small-angle scattering.*

By changing the angle of incidence and the angle of the position sensitive detector (high-angle) diffraction patterns can be observed, as the kapton window of the vacuum chamber covers a large angular range (120°).

**Samples**

All samples have been produced by ion implantation of krypton into aluminium. Sample preparations were carried out at the Ørsted Laboratory of the University of Copenhagen. The 1-2 mm-thick samples were cut by spark-machining from a larger aluminium single crystal of 99.999% purity (Monocrystals Company, Cleveland). The surfaces of the crystals were prepared for implantation by mechanical and electrolytical polishing.

Sample G-1 is a disk 9 mm in diameter, cut with a (111) surface normal. It was implanted at the University of Copenhagen. The krypton ion energy was 100 keV and the fluence was around $2 \cdot 10^{16}$ at/cm$^2$. It had previously been used for x-ray diffraction measurements[21], during which it had been cooled to 14 K, but not heated above room temperature. After the first GISAXS measurements the sample was annealed 30 minutes with a maximum temperature of 650 K.

Sample G-2 is square with a 9 mm-long diagonal, cut with (100) surface normal. After the initial measurements the sample was implanted with 200 keV krypton ions to a fluence of $2 \cdot 10^{16}$ at/cm$^2$. The implantation was carried out at the University of Poitiers. Both samples were implanted at room temperature. An overview of implantation conditions of the two samples is given in Tab. 11.

| Sample | Surface normal | Implantation energy keV | Implantation temperature K | Fluence at/cm$^2$ |
|---|---|---|---|---|
| G-1 (141C) | (111) | 100 | 293 | $2 \cdot 10^{16}$ |
| G-2 | (100) | 200 | 293 | $2 \cdot 10^{16}$ |

*Table 11. Samples of krypton inclusions in aluminium and their surface normals, implantation energies, temperatures, and fluences.*

## 6.2 Results and discussion

Figure 44 shows the diffraction from the sample G-1 before annealing. The large peak at $2\theta \approx 37.8°$ corresponds to the Al (111) reflection and the small peak (marked with an arrow) at $2\theta \approx 27.6°$ corresponds to the (111) reflection from the Kr inclusions. This confirms the existence of Kr inclusions in the sample.

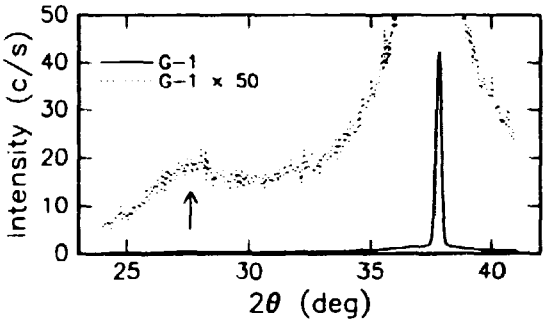


*Figure 44. X-ray diffraction from the sample G-1.*

**Data reduction**

To get the largest part of the scattering curve the angle of incidence ($\alpha_i > \alpha_c$) should be as low as possible. However, the lower the scattering angle is, the stronger the residual reflection from the surface of the sample will be, partially hiding the small-angle scattering signal from the inclusions. At small angles of incidence, the roughness of the surface will also give rise to scattering in the region of angles of interest. Therefore, it can often be useful to compare the signals from the implanted and unimplanted sample, to confirm that the observed scattering is caused by the implanted ions.

Figure 45a shows small-angle x-ray scattering from sample G-2 before and after implantation with $2 \cdot 10^{16}$at/cm$^2$ 200 keV krypton ions. The cut-off at low angles is due to the beam-stop, which was positioned to protect the detector from the direct beam from the monochromator. The peak marked with an arrow is the residual reflection from the surface of the sample at an angle approximately corresponding to $2\alpha_i$. The angle of incidence is slightly different for the unimplanted sample. The observation of the residual reflection proves the high quality (low roughness) of the surface of the sample. Figure 45b shows the same spectra, but the left scale has been reduced. The scattering from the unimplanted sample decreases monotonically with increasing angle above 2°, whereas the implanted sample shows a weak maximum at $2\theta = 2.95°$, caused by the interference between the inclusions.

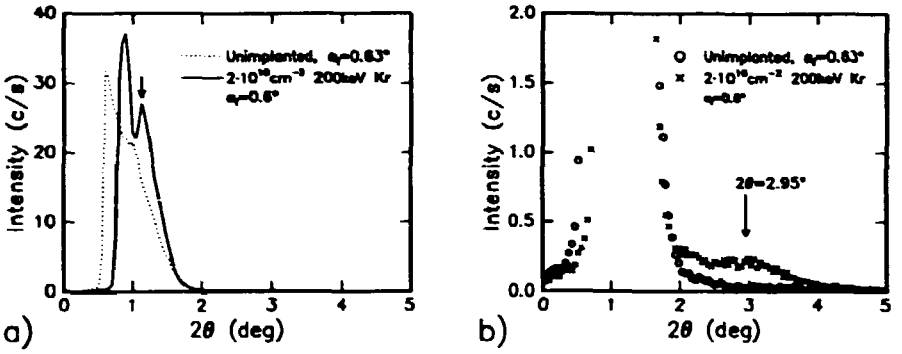


*Figure 45. a) Small-angle scattering spectra of the sample G-2, before (dotted curve) and after (full curve) implantation with $2 \cdot 10^{16}$ at/cm$^2$ 200 keV Kr ions. The peak marked with an arrow is the residual reflection. b) Same as a) with a different scale on the left axis.*

This value corresponds to an average distance between inclusions of $\Lambda = 30$ Å, calculated as

$$\Lambda = \frac{2\pi}{q} = \frac{\lambda}{2\sin\theta} \approx \frac{\lambda}{2\theta}, \tag{27}$$

where $\lambda = 1.54178$ Å is the wavelength of copper $K_\alpha$ radiation and the last approximation is valid as the angle $\theta$ (measured in radians) is small.

The radius of gyration $R_g$ of a homogeneous particle is a geometrical parameter defined as[25]

$$R_g^2 = \frac{\int r^2 dv}{\int dv}, \tag{28}$$

where $r$ is a coordinate vector (with respect to the centre of mass) within the volume of the particle. For a sphere of radius $R$ the radius of gyration is $R_g = \sqrt{3/5}R$. The average intensity per particle $I(2\theta)$ from a set of identical particles having random orientations is given by

$$I(2\theta) = n^2 \exp\left(\frac{-4\pi^2 R_g^2}{3\lambda^2}(2\theta)^2\right), \tag{29}$$

where $n$ is the number of electrons in a particle and $2\theta$ is the scattering angle[25].

In Figure 46a the logarithmic intensity from the sample G-2 after implantation has been plotted against the square of the scattering angle to allow the determination of the radius of gyration from the slope of a linear fit to the data in the region of the scattering from the particles. The value of the radius of gyration from this plot is $R_g = 12$ Å. The small-angle scattering spectrum from the unimplanted sample has been subtracted from the data before the linear fit is made in Fig. 46b, and this gives $R_g = 13$Å.

The results obtained in this way without subtraction of background are given in Tab. 12. The uncertainty on the average distances is ±2 Å; the accuracy of the tabulated radii of gyration may be less, due to the inter-particle interference effects.

## Discussion

The subtraction of a small-angle scattering spectrum of the unimplanted sample demands that great care is taken in aligning the sample, as a small change in the

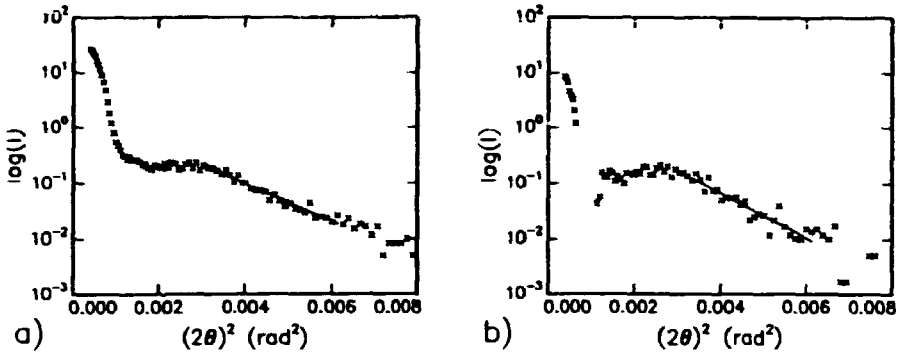


*Figure 46. Small-angle scattering from the sample G-2. The logarithm of the intensity is plotted against the square of the scattering angle. The lines are linear fits to the data. a) Without background subtraction. b) The scattering from the unimplanted sample has been subtracted.*

| Sample | Annealing temperature K | $\alpha_i$ | $\Lambda$ Å | $R_g$ Å |
|---|---|---|---|---|
| G-1 (a) | - | 1.0° | 29 | 8 |
| G-1 (b) | 650 | 0.7° | 39 | 12 |
| G-2 | - | 0.6° | 30 | 12 |

*Table 12. Values of the average distance between inclusions ($\Lambda$) and the radius of gyration ($R_g$). The angle of incidence ($\alpha_i$) is given in the third column. The second line of the sample G-1 gives the values after annealing to 650 K.*

angle of incidence can make a large difference in the scattering spectrum, and in addition, the illuminated area of the sample may be different. With the sample G-2, which has the shape of a disk, the effect of the shadow of the sample may cause large changes, for which it is difficult to correct, in the observed spectrum when the angle of incidence is changed. In the present cases it was found that the background in the angular range of interest was so low, that the data reduction could proceed without subtraction of a background.

In previous x-ray diffraction measurements by Gråbæk[21] on sample G-1, an average size of the Kr inclusions around $2R = 34.5$ Å was determined from the width of the diffraction peak. Approximating the shape of the inclusions by a sphere of radius $R = \sqrt{5/3}R_g$, the average size calculated from the radius of gyration before annealing is $2R = 21$ Å, which is smaller than the earlier measurement. This suggests that the uncertainty on $R_g$ is larger than the 2 Å, which is the estimated uncertainty on $\Lambda$.

From the values of the radius of gyration and the average distance between inclusions the average atomic concentration of the Kr ions in the Al crystal can be estimated as

$$C = \left(\frac{2R_g}{\Lambda}\frac{a^{Al}}{a^{Kr}}\right)^3 \tag{30}$$

The volume fraction have been multiplied by the ratio of the lattice parameters $a^{Al}/a^{Kr}$ to the third power to give the atomic concentrations. The lattice parameter of aluminium is $a^{Al} = 4.05$ Å[71] and the one of the krypton inclusions

($a^{Kr}$ = 5.45 Å) has been taken from the previous measurements by Gråbæk[21] on sample G-1. In the observed average value for $R_g$ the larger inclusions are weighted more heavily than the smaller, and therefore this value is expected ot over-estimate the mean size of the inclusions[56]. A better estimate of the average atomic concentration may be found by using the radius of gyration as a measure of the radius of the inclusions instead of the radius $R$. as

The estimated values of the average atomic concentrations are listed in Tab. 13. The average concentrations have been estimated from the fluences given in Tab. 11, by assuming that all implanted ions are confined within a surface layer of thickness 500 Å for an implantation energy of 100 keV, and 1000 Å for 200 keV. The

| Sample | $C$ from $R$ % | $C$ from $R_g$ % | $C$ from fluence % |
|---|---|---|---|
| G-1 (a) | 15 | 7 | 6.6 |
| G-1 (b) | 21 | 10 | 6.6 |
| G-2 | 45 | 21 | 3.3 |

*Table 13. Average atomic concentrations. The values in the second and third columns are estimated from the GISAXS data, the ones in the last column is calculated from the fluences given in Tab. 11.*

atomic concentrations found from the small-angle scattering data are generally higher than the values calculated from the fluences. This is probably caused by too large values of observed $R_g$, which (as mentioned above) is dominated by the largest inclusions. As the inclusions have formed by precipitation, there is an inclusion-free zone around each of them, and the inter-particle interference is not negligible. Therefore, the values of the radius of gyration derived from the slope of the small-angle scattering curve should be taken with care, and more complicated models should be employed for extracting the average particle radius. Recently, Skov Pedersen *et al.*[56] have demonstrated that a model for interpretation of small-angle scattering data including the effects of both particle correlation and polydispersity gives reasonable results.

## 6.3 Outlook

Grazing-incidence small-angle scattering has yet been applied only to a few experimental investigations, whereas transmission electron microscopy is established as a powerful tool for the investigation of inclusions. One advantage of grazing-incidence small-angle scattering is that the same sample can be studied by both this method and x-ray diffraction. However, as the angle of incidence is low, GISAXS demands a surface of low roughness. Large inclusions pose a problem for GISAXS as the small-angle scattering signal will be too close to the direct beam. However, GISAXS may prove to be a valuable supplement for studying small inclusions, especially at the beginning of their formation. By choosing a heavier element for the inclusions, *e.g.* xenon, the scattering from the inclusions can be increased. A systematic study with improved experimental conditions and more careful data analysis may give quantitative results for the average distances between inclusions and their average mean size.

# 7 Conclusions

Nanometer-size bismuth inclusions in aluminium have been studied by means of x-ray diffraction, ion channeling and transmission electron microscopy. Grazing-incidence small-angle scattering has been used to study krypton inclusions in aluminium. The melting, solidification, orientation with respect to the aluminium matrix and growth of the inclusions have been studied

Transmission electron microscopy has established the facts that when heating the sample some Bi inclusions have melted at 475 K, that is at least 69 K below the bulk melting point, and that when cooling the sample the inclusions are still liquid, when the temperature has been lowered 100 K from the bulk melting point. The x-ray measurements have shown that the width of the melting transition is large (around 100 K). Models (developed by Pawlow and Wronski) of size-dependent melting of small particles fit well the decrease in the x-ray intensity in this temperature range, and size distributions deduced from such fits agree satisfactorily with the mean sizes derived from the width of the x-ray diffraction peak. Further, it has been shown that ion channeling can be observed in Bi inclusions embedded in an Al single crystal and that a heating cycle employing this method gives qualitatively the same results as the x-ray diffraction measurements.

The Bi inclusions have not been seen to take up the structure of the matrix in contrast to many other examples of inclusions in aluminium. Several observations show that the close-packed {110} planes of the rhombohedral Bi inclusions are parallel to the close-packed {111} planes of the fcc aluminium matrix. The detailed structure of the interface between the host and the inclusions is unknown; a high resolution electron microscopy study may be able to solve this intriguing problem.

Grazing-incidence small-angle x-ray scattering has been tested as a new experimental technique for studying small inclusions in aluminium. It has been shown that it is actually possible to observe small-angle scattering under grazing incidence from krypton inclusions in aluminium, and inclusion growth caused by annealing was observed using this method. Quantitative results seem to demand more careful measurements and analysis, however, the results of these preliminary measurements was of the expected order of magnitude.

# Acknowledgements

This work has been supervised by Jakob Bohr and Erik Johnson, and I wish to thank them for their inspiring and supportive guidance into the subjects of this thesis as well as in practical matters during my time as a Ph.D. student in the Department of Solid State Physics at Risø.

Pernille Harris, Erik Johnson, Jan Skov Pedersen, Jakob Bohr, and Allan Johansen are gratefully acknowledged for their careful reading of and comments to all or parts of this thesis. The memory of the late Bronislaw Buras, who took great interest in my work and with whom I profited from many discussions, will always be dear to me. Special thanks are due to David Pengra, Alec Sandy, and Pernille Harris for their help in computer matters whenever I needed it and for stimulating discussions. I would also like to thank Bente Lebech and Jens Lebech for helping me in setting up the Risø temperature controller to run the x-ray furnace. Furthermore, I am very grateful to Lajla Frederiksen and Ca Thi Studinski and the technicians at the Department of Solid State Physics, who have always been ready to solve a practical problem as fast as possible. Also, I wish to thank the staff, Post.Docs, and Ph.D. students at the Department of Solid State Physics.

The transmission electron microscopy, Rutherford backscattering and ion channeling experiments, and most of the sample preparations have been performed at the Orsted Laboratory of the University of Copenhagen. I am very grateful to Erik Johnson, Allan Johansen, Inger Jensen, Konstantin Bourdelle, and Hans Henrik Andersen for their invaluable support in these matters and enlightening discussions on these subjects.

During my Ph.D study I have spent three months at the Laboratory of Physical Metallurgy at the University of Poitiers, France. I would like to thank the staff, Master's students and Ph.D. students there for their great hospitality, and in particular I would like to thank Prof. André Naudon and Prof. Claude Templier for their collaboration and for making me feel at home in the Laboratory and in Poitiers. Furthermore, I would like to thank the organizers of the Hercules course in Grenoble, from which I have benefitted a lot.

My special thanks are due to Kristian Pedersen and Winnie Svendsen, who have spent many hours helping me with the preparation of this thesis — without them, I would still be working on the 30 transmission electron microscope photos included in Chapter 4.

Finally, I would like to thank my family and friends for bearing over with my lack of time for them, especially during the last months of this work.

# References


[1] J. Als-Nielsen. Resolution in diffraction. an outline of the method of conjugate diameters., (1984). Risø-M-2426.

[2] H. H. Andersen, J. Bohr, A. Johansen, E. Johnson, L. Sarholt-Kristensen, and V. Surganov. Melting and misalignment of solid crystalline krypton inclusions in aluminium. *Phys. Rev. Lett.*, **59**, 1589, (1987).

[3] H. H. Andersen, J. Bøttiger, and H. Wolder-Jørgensen. Ranges of ions with $Z_1 \geq 54$ in Al and $Al_2O_3$. *Appl. Phys. Lett.*, **26**, 678, (1975).

[4] Hans Henrik Andersen. *Overflade og tyndfilmsanalyse fortrinsvis ved hjælp af Rutherfordtilbagespredning.* Fysisk Laboratorium, H. C. Ørsted Institutet, (1992). Notes for the course Eksperimentelle metoder til faststoffysiske strukturstudier.

[5] J. H. Barrett. Monte Carlo channeling calculations. *Phys. Rev. B*, **3**, 1527, (1971).

[6] S. Bjørnholm. Clusters, condensed matter in embryonic form. *Contemp. Phys.*, **31**, 309, (1990).

[7] K. K. Bourdelle, A. Johansen, E. Johnson, and L. Sarholt-Kristensen. Melting and solidification of nanosized lead crystallites in aluminium studied by means of channeling. In *Proceedings from International Symposium on Metastable Mechanically Alloyed and Nanocrystalline Materials*, Grenoble, France, (1994).

[8] K. K. Bourdelle, V. A. Khodyrev, A. Johansen, E. Johnson, and L. Sarholt-Kristensen. Evolution of precipitates in lead-implanted aluminium: A backscattering and channeling study. *Phys. Rev. B*, **50**, 82, (1994).

[9] W. L. Bragg. *Proc. Camb. Phil. Soc.*, **17**, 43, (1913).

[10] E. A. Brandes, editor. *Smithells Metals Reference Book.* Butterworths, London, (1983).

[11] Ph. Buffat and J.-P. Borel. Size effect on the melting temperature of gold particles. *Phys. Rev. A*, **13**, 2287, (1976).

[12] B. Cantor. Embedded droplet measurements and an adsorption model of the heterogeneous nucleation of solidification. *Mat. Sc. Eng. A*, **178**, 225, (1994).

[13] W.-K. Chu, J. W. Mayer, and M.-A. Nicolet. *Backscattering Spectrometry.* Academic Press, Boston, (1978).

[14] C. J. Coombes. The melting of small particles of lead and indium. *J. Phys.*, **2**, 441, (1972).

[15] C. Ellegaard and N. O. Lassen. String effect with 5 Mev protons and 20 Mev alpha particles on bismuth. *Dan. Vidensk. Selsk. Mat.-Fys. Medd.*, **35**, No. 16, (1967).

[16] R. Feidenhans'l. Surface structure determination by x-ray diffraction. *Surf. Sci. Rep.*, **10**, 105, (1989).

[17] A. vom Felde, J. Fink, Th. Müller-Heinzerling, J. Pflüger, B. Scheerer, and G. Linker. Pressure of neon, argon, and xenon bubbles in aluminium. *Phys Rev. Lett.*, **53**, 922, (1984).

[18] J. W. M. Frenken and J. F. van der Veen. Observation of surface melting. *Phys. Rev. Lett.*, **54**, 134, (1985).

[19] W. Friedrich, P. Knipping, and M. Laue. Interferenz-Erscheinungen bei Röntgenstrahlen. *Sitz. math. phys. Klasse Bayer. Akad. Wiss.*, 303, (1912).

[20] Donald S. Gemmell. Channeling and related effects in the motion of charged particles through crystals. *Rev. Mod. Phys.*, **46**, 129, (1974).

[21] L. Gråbæk. *X-ray Diffraction Studies of Kr, Xe and Pb Inclusions in Aluminium*. PhD thesis, (1990). Risø-M-2868.

[22] L. Gråbæk, J. Bohr, H. H. Andersen, A. Johansen, E. Johnson, L. Sarholt-Kristensen, and I. K. Robinson. Melting, growth, and faceting of lead precipitates in aluminium. *Phys. Rev. B*, **45**, 2628, (1992).

[23] L. Gråbæk, J. Bohr, E. Johnson, L. Sarholt-Kristensen A. Johansen, and H. H. Andersen. Superheating and supercooling of lead precipitates in aluminium. *Phys. Rev. Lett.*, **64**, 934, (1990).

[24] L. Gråbæk, J. Bohr, E. Johnson, H. H. Andersen, A. Johansen, and L. Sarholt-Kristensen. X-ray studies of krypton, xenon and lead inclusions in aluminium single crystals. *Mat. Sci. Eng. A*, **115**, 97–101, (1989).

[25] A. Guinier. *X-Ray Diffraction In Crystals, Imperfect Crystals, and Amorphous Bodies*. Freeman, San Francisco, (1963).

[26] M. R. Harrison and P. P. Edwards. Electrons in small metallic particles. In P. P. Edwards and C. N. R. Rao, editors, *The metallic and nonmetallic states of matter*, 389. Taylor and Francis, London, (1985).

[27] N. F. M. Henry and K. Lonsdale, editors. *International Tables for X-ray Crystallography*. International Union of Crystallography, Birmingham, UK, (1965).

[28] P. B. Hirsch, A. Howie, R. B. Nicholson, D. W. Pashley, and M. J. Whelan. *Electron Microscopy of Thin Crystals*. Butterworths, London, (1965).

[29] Kirsten Hjemsted. Elektronmikroskopi af Al-In legeringer. Master's thesis, University of Copenhagen, (1991). Available from the Ørsted Laboratory.

[30] A. Horsewell. Solid sodium particles in aluminium. *Philos. Mag. B*, **62**, 647–658, (1990).

[31] A. Horsewell, E. Johnson, and K. K. Bourdelle. The sodium-aluminium interface. In *Proceedings from 6$^{th}$ International Conference on Intergranular and Interphase Boundaries in Materials*, Thessaloniki, Greece, June (1992). To be published in Materials Science Forum.

[32] E. Johnson, K. Hjemsted, B. Schmidt, K. K. Bourdelle, A. Johansen, H. H. Andersen, and L. Sarholt-Kristensen. Small lead and indium inclusions in aluminium. In G. S. Was, D. M. Fallstaedt, and L. E. Rehn, editors, *Phase Formation and Modification by Beam-Solid Interactions*, volume 235, 485. Materials Research Society Symposium Proceedings, (1992).

[33] E. Johnson, K. Hjemsted, B. Schmidt, K. K. Bourdelle, A. Johansen, H. H. Andersen, and L. Sarholt-Kristensen. Nanosize lead inclusions in aluminium. In *Electron Microscopy*, volume 2, Granada, Spain, (1992). EUREM 92.

[34] E. Johnson, A. Johansen, N. B. Thoft, H. H. Andersen, and L. Sarholt-Kristensen. Nanosized f.c.c. thallium inclusions in aluminium. *Philos. Mag. Lett.*, **68**, 131, (1993).

[35] G. W. C. Kaye and T. H. Laby. *Physical and Chemical Constants*. Longmans, London, (1959).

[36] R. Kofman, P. Cheyssac, and R. Garrigos. From the bulk to the clusters: solid-liquid phase transitions and precursor effects. *Phase Transitions*, **24-26**, 283, (1990).

[37] J. R. Levine, J. B. Cohen, Y. W. Chung, and P. Georgopoulos. Grazing-incidence small-angle x-ray scattering: New tool for studying thin film growth. *J. Appl. Cryst.*, **22**, 528, (1989).

[38] F. A. Lindemann. Über die Berechnung molekularer Eigenfrequenzen. *Phys. Zeitschr.*, **11**, 609, (1910).

[39] R. Lipowsky. Critical surface phenomena at first-order bulk transitions. *Phys. Rev. Lett.*, **49**, 1575, (1982).

[40] T. B. Massalski, J. L. Murray, L. H. Bennett, and H. Baker, editors. *Binary Alloy Phase Diagrams*, volume 1. American Society for Metals, Metals Park, Ohio, (1986).

[41] A. R. Miedema. The atom as a metallurgical building block. *Philips Techn. Rev.*, **38**, 257, (1978-79).

[42] K. I. Moore, K. Chattopadhyay, and B. Cantor. *In situ* transmission electron microscope measurements of solid Al-solid Pb and solid Al-liquid Pb surface-energy anisotropy in rapidly solidified Al-5% Pb (by mass). *Proc. Roy. soc. Lond. A*, **414**, 499, (1987).

[43] K. I. Moore, D. L. Zhang, and B. Cantor. Solidification of Pb particles embedded in Al. *Acta metall. mater.*, **38**, 1327, (1990).

[44] A. Naudon, T. Slimani, and P. Goudeau. Grazing small-angle scattering of x-rays for the study of thin surface layers. *J. Appl. Cryst.*, **24**, 501, (1991).

[45] J. Staun Olsen, L. Gerward, S. Steenstrup, and E. Johnson. A high-pressure study of thallium. *J. Appl. Cryst.*, **27**, 1002, (1994).

[46] P. Pawlow. Über die Abhängigkeit des Schmelzpunktes von der Oberflächenenergie eines festen Körpers. *Z. Phys. Chem.*, **65**, 545, (1909).

[47] S. J. Peppiatt and J. R. Samples. The melting of small particles. I. Lead. *Proc. R. Soc. Lond. A*, **345**, 387, (1975).

[48] D. A. Porter and K. E. Easterling. *Phase Transformations in Metals and Alloys*. Chapman & Hall, London, 2 edition, (1992).

[49] R. Pynn, Y. Fujii, and G. Shirane. The resolution function of a perfect-crystal three-axis x-ray spectrometer. *Acta Cryst. A*, **39**, 38, (1983).

[50] M. Roth, G. C. Weatherly, and W. A. Miller. On superheating and supercooling of lead and bismuth inclusions in aluminium. *Can. Metall. Quarterly*, **14**, 287, (1975).

[51] H. Saka, Y. Nishikawa, and T. Imura. Melting temperature of in particles embedded in an al matrix. *Philos. Mag. A*, **57**, 895, (1988).

[52] L. Sarholt-Kristensen, A. Johansen, E. Johnson, K. K. Bourdelle, M. Olsen, and H. H. Andersen. Nanosized cadmium crystallites in aluminium. In *Proceedings from International Symposium on Metastable Mechanically Alloyed and Nanocrystalline Materials*, Grenoble, France, (1994).

[53] K. Sasaki and H. Saka. *In situ* high-resolution electron microscopy observation of the melting process of In particles embedded in an Al matrix. *Philos. Mag. A*, **63**, 1207, (1991).

[54] B. Schmidt. Karakterisering af nm-store Pb krystaller i aluminium. Master's thesis, University of Copenhagen, (1992). Available from the Orsted Laboratory.

[55] F. G. Shi. Size dependent thermal vibrations and melting in nanocrystals. *J. Mater. Res.*, **9**, 1307, (1994).

[56] J. Skov Pedersen. Small-angle scattering from precipitates: Analysis by a polydisperse hard-sphere model. *Phys. Rev. B*, **47**, 657, (1993).

[57] T. Slimani, N. B. Thoft, and A. Naudon. Precipitation study in thin layers by grazing small-angle scattering of x-rays. *J. Phys. Colloq.*, **C8**, 303, (1993). Proccedings of the IX International Conference on Small-Angle Scattering.

[58] A. H. Sørensen. Elektronmikroskopiske undersøgelser af nanometer-store thallium inklusioner i aluminium. Master's thesis, University of Copenhagen, (1994). Available from the Orsted Laboratory.

[59] A. H. Sørensen, E. Johnson, K. K. Bourdelle, A. Johansen, H. H. Andersen, and L. Sarholt-Kristensen. Nanosized thallium inclusions in aluminium. In *Proceedings from 13th International Conference on Electron Microscopy*, Paris, France, July (1994).

[60] M. Takagi. Electron-diffraction study of liquid-solid transition of thin metal films. *J. Phys. Soc. Jap.*, **9**, 359, (1954).

[61] C. Templier, H. Garem, and J. P. Riviére. Transmission electron microscope study of xenon implanted into metals. *Philos. Mag. A*, **53**, 667, (1986).

[62] C. Templier, C. Jaouen, J. P. Riviére, J. Delafond, and J. Grilhé. Précipitation du xénon implanté dans des alliages d'aluminium. *C.R. Acad. Sc. Paris*, **299**, 613, (1984). Série II.

[63] J. Tersoff, A. W. Denier van der Gon, and R. M. Tromp. Shape oscillations in growth of small crystals. *Phys. Rev. Lett.*, **70**, 1143, (1993).

[64] N. B. Thoft, J. Bohr, B. Buras, E. Johnson, A. Johansen, H. H. Andersen, and L. Sarholt-Kristensen. Melting and solidification of bismuth inclusions in aluminium. To be published in J. Phys. D: Appl. Phys.

[65] E. Yu. Tonkov. *High Pressure Phase Transformations. A Handbook*, volume 2. Gordon and Breach, Philadelphia, Pennsylvania, (1992).

[66] D. Turnbull. Formation of crystal nuclei in liquid metals. *J. Appl. Phys.*, **21**, 1022, (1950).

[67] D. Turnbull and R. E. Cech. Microscopic observation of the solidification of small metal droplets. *J. Appl. Phys.*, **21**, 804, (1950).

[68] B. E. Warren. *X-Ray Diffraction*. Dover, New York, second edition, (1990). First edition 1969, Addison-Wesley, Reading, Massachussets.

[69] R. C. Weast, editor. *CRC Handbook of Chemistry and Physics*. CRC Press, (1979).

[70] C. R. M. Wronski. The size dependence of the melting point of small particles of tin. *Br. J. Appl. Phys.*, **18**, 1731, (1967).

[71] R. W. G. Wyckoff. *Crystal Structures*, volume 1. Wiley, New York, (1963).

[72] S. Q. Xiao, S. Hindenberger, U. Dahmen, E. Johnson, A. Johansen, and K. K. Bourdelle. High-resolution in-situ observations of nanometer-size Pb inclusions in Al near their melting point. In *Frontiers in Electron Microscopy*, Livermore, California, (1994).

[73] W. Yoon, J. S. Paik, D. LaCourt, and J. H. Perepezko. The effect of pressure on phase selection during nucleation in undercooled bismuth. *J. Appl. Phys.*, **60**, 3489, (1986).

[74] D. L. Zhang and B. Cantor. Heterogeneous nucleation of In particles embedded in an Al matrix. *Philos. Mag. A.* **62**, 557, (1990).

[75] D. L. Zhang and B. Cantor. Melting behaviour of In and Pb particles embedded in an Al matrix. *Acta metall. mater.*, **39**, 1595–1602, (1991).

[76] D. L. Zhang, K. Chattopadhyay, and B. Cantor. Heterogeneous nucleation of solidification of cadmium particles embedded in an aluminium matrix. *J. Mater. Sci.*, **26**, 1531–1544, (1991).

[77] J. F. Ziegler, J. P. Biersack, and U. Littmark. *The Stopping and Ranges of Ions in Solids*. Pergamon, New York, (1985).

# A TEM orientational relationship from Fig. 25

Assuming that the two Bi reflections marked in Fig. 25b stem from inclusions of the same orientation relatively to the aluminium lattice, this orientation can be determined. The plane of the paper is a $\{100\}_{Al}$ plane, *e.g.* the $(200)_{Al}$ plane. If it is as well a plane $(hkl)$ of the Bi lattice, $h$, $k$, and $l$ fulfill

$$q^{Bi}_{hkl} \perp q^{Bi}_{110} \quad \text{and} \quad q^{Bi}_{hkl} \perp q^{Bi}_{0\bar{1}1}. \tag{A.1}$$

The angle $\phi$ between planes $(hkl)$ and $(h'k'l')$ in a rhombohedral lattice is

$$\begin{aligned} \cos\phi &= \frac{(hh' + kk' + ll')\sin^2\alpha}{a^4 d_{hkl} d_{h'k'l'}/V^2} \\ &+ \frac{(hk' + kh' + kl' + lk' + lh' + hl')(\cos^2\alpha - \cos\alpha)}{a^4 d_{hkl} d_{h'k'l'}/V^2} \\ V &= a^3\sqrt{1 - 3\cos^2\alpha + 2\cos^3\alpha} \\ d_{hkl} &= \frac{\sqrt{((h^2 + k^2 + l^2)\sin^2\alpha + 2(hk + kl + lh)(\cos^2\alpha - \cos\alpha))}}{V/a^2} \end{aligned} \tag{A.2}$$

The requirement of orthogonality (Eq. A.1) and Eq. A.2 lead to

$$\begin{aligned} (h + k)\sin^2\alpha &= (\cos\alpha - \cos^2\alpha)(h + k + 2l) \quad \text{and} \\ -(k - l)\sin^2\alpha &= (\cos\alpha - \cos^2\alpha)(k - l) \end{aligned}$$

These two equations have the solutions

$$l = k \quad \text{and} \quad l = \frac{h}{2\cos\alpha - 1}. \tag{A.3}$$

Inserting the value $\alpha = 57.2369°$ of the bismuth rhombohedral lattice the latter equation reads $l \approx h \cdot 12.1457$. As $h$,$k$ and $l$ have to be integers, it is only possible to find approximate solutions, *e.g.*

$$h = 350 \quad \text{and} \quad k = l = 4251.$$

These values fulfills Eq. A.3 fairly accurately, but a (350,4251,4251) plane in the inclusions does not make any sense. Though still high, the indices (1,12,12) are easier to picture, and the angle between the latter and former planes is less than 1/10°; a difference of no importance considering the uncertainties involved. The aluminium (200) plane and bismuth (1,12,12) plane are thus approximately parallel.

It should be noted that the angle between the bismuth (011) and (1,12,12) (or (350,4251,4251)) planes is small, 3.45°(or 3.41 ,, suggesting the relationship $\{0,1,1\}_{Bi} \parallel \{2,0,0\}_{Al}$. However, this relationship has not been confirmed by the selected area diffraction images which include the {2,0,0} Al reflections.

In Fig. 25 the angle between the bismuth $\{0\bar{1}1\}$ and aluminium {022} reflection is approximately 10°. As $q^{Al}_{022} \parallel [022]_{Al}$ and, as an exception, $q^{Bi}_{0\bar{1}1} \parallel [0\bar{1}1]_{Bi}$

$$\angle([0,\bar{1},1]_{Bi}, [0,2,2]_{Al}) \approx 10.0°.$$

**Bibliographic Data Sheet** **Risø-R-783(EN)**

Title and author(s)

Annealing Studies of Bi and Kr Inclusions in Al

Nina Bjørn Thoft


| ISBN | ISSN |
|---|---|
| 87-550-2028-3 | 0106-2840 |

| Dept. or group | Date |
|---|---|
| FYS | April 1995 |

| Groups own reg. number(s) | Project/contract no. |
|---|---|
| | |

| Pages | Tables | Illustrations | References |
|---|---|---|---|
| 82 | 13 | 46 | 77 |



Abstract (Max. 2000 char.)

This report contains the results of experimental investigations of melting, solidification and growth of Bi and Kr inclusions made by ion implantation into aluminium.

The experimental techniques used for this study were x-ray diffraction, transmission electron microscopy, Rutherford backscattering, ion channeling, and grazing-incidence small-angle x-ray scattering.

The x-ray diffraction signal from crystalline Bi inclusions in Al has been recorded as a function of temperature during heating to temperatures above the bulk melting point and cooling to room temperature. Data from these measurements have been fitted using models (developed by Pawlow and Wronski) for the size-dependent melting temperature of small particles, and size distributions for the inclusions have been determined in this way.

Transmission electron microscopy has confirmed the melting and solidification of the Bi inclusions in the temperature ranges, in which these processes were observed by x-ray diffraction, establishing the facts that the inclusions melt below the bulk melting point and that a large supercooling is seen.

Information about the amount and depth distribution of the Bi confined in the Al matrix has been derived from Rutherford backscattering measurements. Melting and solidification of Bi inclusions have been observed by means of ion channeling. The results of the investigations of bismuth inclusions in aluminium are compared to previous, similar results for lead inclusions in aluminium.

Finally, preliminary experiments have confirmed that growth of Kr inclusions in Al can be observed using grazing-incidence small-angle scattering.



Descriptors INIS/EDB

ALUMINIUM; ANNEALING; BISMUTH; CRYSTAL GROWTH; INCLUSIONS; ION CHANNELING; ION IMPLANTATION; KRYPTON; MELTING; SMALL ANGLE SCATTERING; SOLIDIFICATION; TRANSMISSION ELECTRON MICROSCOPY; X-RAY DIFFRACTION



Available on exchange (R) or request (M) from:
Risø Library, Risø National Laboratory (Risø Bibliotek, Forskningscenter Risø)
P.O. Box 49, DK-4000 Roskilde, Denmark
Phone +45 42 37 12 12, ext. 2268/2269 · Telex 43 116 · Telefax +45 46 75 56 27

RISØ

## Objective

The objective of Risø's research is to provide industry and society with new potential in three main areas:

- *Energy technology and energy planning*
- *Environmental aspects of energy, industrial and plant production*
- *Materials and measuring techniques for industry*

As a special obligation Risø maintains and extends the knowledge required to advise the authorities on nuclear matters.

## Research Profile

Risø's research is long-term and knowledge-oriented and directed toward areas where there are recognised needs for new solutions in Danish society. The programme areas are:

- *Combustion and gasification*
- *Wind energy*
- *Energy technologies for the future*
- *Energy planning*
- *Environmental aspects of energy and industrial production*
- *Environmental aspects of plant production*
- *Nuclear safety and radiation protection*
- *Materials with new physical and chemical properties*
- *Structural materials*
- *Optical measurement techniques and information processing*

## Transfer of Knowledge

The results of Risø's research are transferred to industry and authorities through:

- *Research co-operation*
- *Co-operation in R&D consortia*
- *R&D clubs and exchange of researchers*
- *Centre for Advanced Technology*
- *Patenting and licencing activities*

To the scientific world through:

- *Publication activities*
- *Co-operation in national and international networks*
- *PhD- and Post Doc. education*

**Risø-R-783(EN)**
**ISBN 87-550-2028-3**
**ISSN 0106-2840**

Available on request from:
**Information Service Department**
**Risø National Laboratory**
P.O. Box 49, DK-4000 Roskilde, Denmark
Phone +45 46 77 46 77, ext. 4004/4005
Telex 43116, Fax +45 46 75 56 27

## Key Figures

Risø has a staff of just over 900, of which more than 300 are scientists and 80 are PhD and Post Doc. students. Risø's 1995 budget totals DKK 476m, of which 45% come from research programmes and commercial contracts, while the remainder is covered by government appropriations.